Doctoral Dissertation

Tip-enhanced nano-Raman analysis of deformation in single wall carbon nanotubes

Yoshito Okuno

December 2013

Graduate School of Engineering,

Osaka University

Lists of contents

Introduction

Physics is a foundation of matter and energy. Ancestors invented a laser and a transistor by grace of physics. We created a first computer and a first airplane with the aid of physics, in other words almost everything you see in your living room and on a street can be traced back to physics. Utilizing physics, we have done and created many things for our better prosperity and have foretold future. Now we are going to have a car driving itself, which we couldn't imagine 20 years ago, and strive to seek the unified field theory which is believed to have one-inch long equation to explain everything. I was attracted such a potential of physics and I wished to be the one who apply physics to make new revolutionary products and a better future.

Now, while Moore's law, which is the observation that the number of transistors and integrated circuits doubles approximately every 18 months, is about to saturate, fundamental methods for breaking this stagnation is needed for us to prosper more forward to better life in the future. This year, a research group in Harvard University demonstrated carbon nanotubes (CNTs) circuits as a first report [1]. The accomplishment gave a great impact on all researchers in the field of nanotechnology because if we can apply CNTs to build circuits, performance of semiconducting products could be dramatically improved due to their wealth of electronic property and a size of their diameters with overwhelmingly small enough to reach to 1nm [2-5]. Therefore, it is no exaggeration to say that this event was the dawn of nano-electronic device utilizing CNTs.

My research purpose is to see nano-materials with light. Especially, the nano-materials I investigated were single-walled carbon nanotubes (SWCNTs). SWCNTs are molecules described as rolled up graphene sheet, which has a variety of band gap and play a role as metal and semiconductor depending on the combination of rolling angle and radius. Products made of SWCNTs such as nano-transistor [2], high integrated circuits [6] and field emitters in flat panel displays [23] are expected to have a great role as nano-electronic devices with a variety of electronic characteristic. A surge of the interests has given rise to many methods for tailoring electronic properties of SWCNTs such as chemical functionalization [7-8], encapsulation of organic and non-organic materials inside SWCNTs and structural deformation [9]. In particular, interesting configurations to study are arbitrary deformations and the deformations caused through the process of SWCNTs bridging over other SWCNTs. These deformations widen their

application possibilities because they are flexible techniques for making defects and modifying electronic band structure by strong pressurization on SWCNTs or interconnects which induce tunnel barriers. Interestingly, arbitrary deformations has been pointed out as a cause of strains, which is very significant for tuning electronic property of SWCNTs, and a pressurization on semiconducting SWCNTs was predicted to have a bearing on metallization of semiconducting SWCNTs attributable to $\pi^* - \sigma^*$ hybridization effect [10]. The metallization is expected to occur also by crossing them each other. However, what types of strains is applied on deformed SWCNTs and what is the detailed cause of this metallization have not been supported well by other researches. Therefore, there remains considerable debates and stimulate extensive research enthusiasm on these types and main causes because they are localized property's change and it needs analysis in nanoscale region.

Raman spectroscopic measurement is a suitable tool for paving the way to understand the physical properties of SWCNTs depending on their positions because of their ability to detect directly vibrational features of molecule and topographical information simultaneously. Raman spectroscopic measurement enables us to easily see what is happening on SWCNTs as a 2D imaging. From the first experimental report about Raman scattering of SWCNTs by Rao et. al. in 1997 [11], Raman spectroscopy has became a standard technique for understanding how physical properties change by a certain perturbation such as chemical functionalization, electronic field, strains and defects. In 2000, Alf Mews et. al. reported the imaging of CNTs by use of scanning confocal Raman microscopy for locating individual SWCNTs for the first time [12]. Since then, spectroscopic analysis of SWCNTs turned to microscopic one, which push researchers to perceive physical properties of them as 2D image.

Let me refer to prime researches on Raman investigations on SWCNTs for giving a detailed account. Mildred S. Dresselhaus et al. evaluated the defects induced on SWCNTs by Ar plasma through the detection of D-band signature [13]. New physical property achieved by functionalizing carbon nanotube with a dope of various types of foreign atoms [24-26] or with absorption of atoms or molecules [27, 28] has been evaluated by Raman measurements. For example, Richard E. Smalley [29] et al. succeeded to elucidate the charge transfer degree difference depending on types of doped atoms by monitoring the frequency shift of longitudinal optical mode in G-band [14]. Now since the report from M. S. Dresselhaus et al., an observation of strains applied nanotubes with Raman spectroscopy become more and more significant

because of an easy and a quick way to observe the tailored properties [15].

One of challenges in a Raman observation of SWCNTs is high spatial resolution. This is because SWCNTs have nano-structure and their entire property can be affected completely by localized nano-change in their physical property. Kawata et al. suggested tip-enhanced Raman scattering (TERS) microscopy for reaching 10-30 nm spatial resolution [16-22]. Tip-enhanced coherent Raman scattering microscopy was developed by the combination of TERS with nonlinear optical response, which suggested a road for a better signal sensitivity and a better spatial resolution [19]. Such that, researches on physical properties of SWCNTs become more and more hot by the support of new optical microscope and techniques. However, you might think that Raman scattering of SWCNTs come into being as normal vibrations of whole crystal and we can't regard vibrational modes as information of localized properties. It is not true. Each Raman mode has a line width. This implies that each vibrational motion is not complete coherent phenomena and it brings the information of localized properties. Therefore, the new optical microscopes suggested today will make a significant contribution to observe nano-localized properties in SWCNTs.

In first chapter, I introduce the principle of Raman scattering in SWCNTs. In second chapter, I explain the principle of tip-enhanced techniques for improving spatial resolution and efficiency of signal generation. In third chapter, I show the results of Raman scattering investigations on deformed SWCNTs. In forth chapter, I indicate that local pressure cause metal transition from semiconducting feature of SWCNTs, which was revealed through tip-enhanced Raman investigations on crossed SWCNTs. Finally, I conclude the dissertation by orderly explanations read off from the whole text in my dissertation.

References:

[1] Max M. Shulaker et al., NATURE, VOL **501**, 526, (SEPTEMBER 2013).

[2] A. D. Franklin, et al., Nano Lett. **12**, 758–762 (2012).

[3] L. Wei, D. Frank, L. Chang, & Wong, H.-S. P. in Proc. 2009 IEEE Intl Electron Devices Meeting 917–920 (IEEE, 2009).

[4] R. A. Martel et. al., Appl. Phys. Lett., **73**, 2447 (1998).

[5] S. J. Tans, A. R. Verschueren, & C. Dekker, Nature, **393**, 49–52 (1998).

[6] Z. Chen, et al., Science, **311**, 1735 (2006).

[7] Z. Liu *et al.,* PNAS, **105**, 1410 (2008).

[8] M. S. Strano *et al.,* Science, **301**, 1519 (2003).

[9] T. W. Tombler *et al.,* Nature (London) **405**, 769 (2000).

[10] X. Blase *et al.,* Phys. Rev. Lett.., **72**, 1878 (1994).

[11] A.M.Rao et.al., NATURE, VOL **388**, 257-259, (1997).

[12] Alf Mews et. al., Adv. Mater., **12**, No. 16, (2000) .

[13] M. Kalbac et. al., Nano Lett, **10***,* 4619–4626, (2010).

[14] A. M. Rao *et al.,* Nature **388**, 257 (1997).

[15] A. G. Souza Filho et al., Phys. Rev. Lett, **95,** 217403 (2005).

[16] N. Hayazawa et. al., J. Microsc., **194**, 472-476, (1999).

[17] N. Hayazawa, Y. Inouye, Z. Sekkat, & S. Kawata, *Optics Communications,* Vol. **183**, No. 1-4, pp. 333-336, (2000).

[18] N. Hayazawa, Y. Saito, & S. Kawata, Appl. Phys. Lett., **85**, 6239-6241, (2004).

[19] T. Ichimura et. al., Phys. Rev. Lett, VOLUME **92**, NUMBER 22, (2004).

[20] T. Yano et. al., Appl. Phys. Lett., **88**, 93125 (2006).

[21] Y. Saito et. al., J. Raman. Spectrosc., **39**, 1643-1648, (2008).

[22] T.Yano et. al., Nature Photon., **3**, 437–441 (2009).

[23] Q. H. Wang, A. A. Setlur, J. M. Lauerhaas, J. Y. Dai, E. W. Seelig, and R. P. H. Chang,

Appl. Phys. Lett., **72**, 2912 (1998).

[24] D. Golberg, Y. Bando, W. Han, K. Kurashima, and T. Sato, Chem. Phys. Lett., **308**, 337 (1999).

[25] F. Villalpando-Paez et al., Chem.Phys. Lett., **424**, 345 (2006).

[26] S. S. Yu, Q. B. Wen, W. T. Zheng, and Q. Jiang, Nanotechnology., **18**, 165702 (2007).

[27] L. Qiao, W. T. Zheng, Q. B. Wen, and Q. Jiang, Nanotechnology., **18**,155707 (2007).

[28] S. F. Xu, G. Yuan, C. Li, W. H. Liu, and H. Mimura, J. Phys. Chem. C, **115**, 8928 (2011).

[29] W. Wade Adams and Ray H. Baughman*, "*Richard E. Smalley (1943-2005)*",* Science*,* **310**, 1916 (2005).

Chapter 1. Raman scattering at single walled carbon nanotubes (SWCNTs)

A new type of secondary radiation found in 1928 became a ground-breaking discovery, which is now called Raman scattering [1, 2]. The discovery has stimulated researches in the fields of biological science, medical science, material science and so on. Time has passed and then since Iijima's discovery of SWCNTs, which is fascinating materials for nano-electronic devices, in 1991 [3], many analytical methods have been applied to observe the hidden nature in SWCNTs. However, most of the methods just revealed one or two particular properties of SWCNTs because of a lack of information in signal for analysis. Raman scattering totally resolve such problems. What does Raman scattering tell us? Before proceeding to following chapters, I decide myself to explain what Raman scattering tells us and how about the case in SWCNTs for your better understanding on how beneficial Raman scattering of SWCNTs is. In first section, I explain a principle of Raman scattering. In second section, I will introduce basics of Raman scattering of SWCNTs and how it relates to their own physical properties.

1-1. Raman scattering

Raman scattering is the light interacted with a material and emerges in accordance with selection rule derived from a symmetric property of a material. At the beginning of this section, I would like to mention the overview of Raman scattering and pursue the subject toward Kramers-Heisenberg-Dirac (K-H-D) dispersion formula used for estimating the intensity of Raman scattering. Finally, I will develop the selection rule using K-H-D dispersion formula.

Overview of Raman scattering

The scattering process of light can be considered as a collision process between photon and material. In this process, Rayleigh scattering takes place by an elastic collision without energy conversion and Raman scattering takes place by an inelastic collision with energy conversion [4]. The exchanged energy through the Raman scattering process corresponds to the energy required for a transition from an initial state to a final state of material as shown in Fig. 1. This energy is detectable as a spectrum.

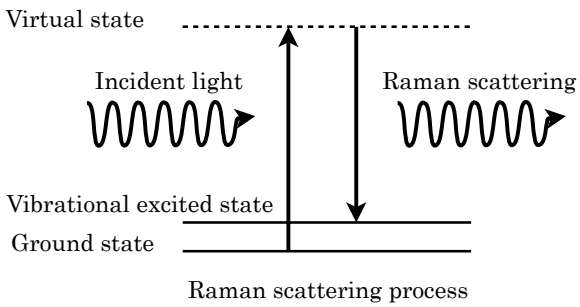

Fig.1 | Scheme of Raman scattering process is shown above. When incident light comes into a certain system, an electron in ground state goes up to virtual state by absorbing one photon. After a vibrational lifetime, an electron goes down to a vibrational excited state of ground electronic state, then the system generate a scattered photon.

Fig. 2 shows a schematic image of a typical Raman spectrum from material. The frequency of the spectrum is equals to difference between that of incident light and that of Raman scattering. The Raman scatterings are classified as Stokes and Anti-Stokes scattering, respectively.

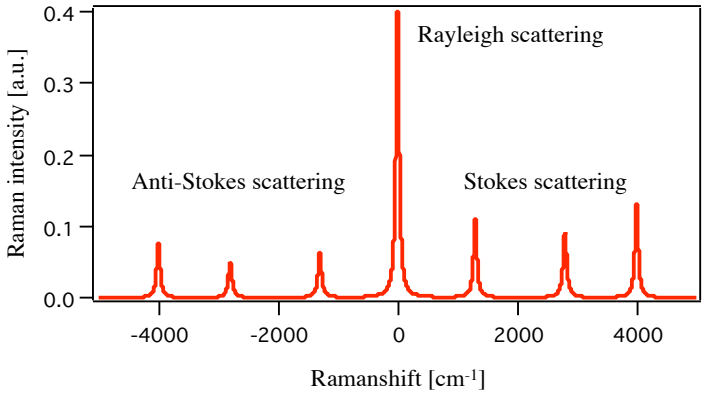

Fig.2 | Schematic image of a typical Raman spectrum from materials.

The strongest peak positioned center is Rayleigh scattering. Three peaks positioned to the left side of the center are attributed to Anti-Stokes scattering and other peaks positioned to the right are attributed to Stokes scattering. This spectrum displays the intensity at its vertical axis and wavenumber at its horizontal one. Unit used either for intensity or Raman shift is arbitral unit or cm^{-1}. This spectrum tells detailed molecular information with the intensity and the position of peaks. In usual, the intensity indicates the volume of molecule and the peak position tells chemical composition.

Raman spectra can be classified by the state of motion of material. Raman scattering has been classified as following types: 1) Rotational Raman scattering caused by the intra transition between different rotational states in same vibrational and electronic states 2) Rotational Raman scattering caused by the intra transition between different rotational states in different vibrational and same electronic states. These modes appear in air condition, which does not regulate rotational motions. In contrast to that, in liquid and in solid condition, quantized energy levels of rotational motions disappear because of strict regulation imposed against rotational movements. Then vibrational Raman scattering, which derives from inter transition between different vibrational states in same electronic state, has a dominant role. The number of normal vibrational modes equals $3N - 6$. The number derives from the number of degrees of freedom subtracted by 3 rotational motions and 3 translational motions. Since the Raman scattering by vibrational transition reflects the feature of their composition and configuration of atoms, it is called a fingerprint of molecules that is an identifier for the individuality of molecules. Therefore, it is used in the field of analytical science. In the case of crystals, vibration modes derive from translational motion of atoms and molecules. This is the quantized quasi-particle called “Phonon”. In the process of collision between photon and phonon, a part of light is scattered in sensitive with the structure of crystal. In this time, since the object of observation is a carbon nanotube composed of carbon atoms aligned in regulated manner, the concept of “Phonon” is quite important.

K-H-D dispersion equation from a mutual effect between electron and radiant field

A theory of Raman scattering has been explained by two points of views. One is classical theory that Raman tensor is related to the intensity of the scattering but usually indicate just intuitive and qualitative comprehension of Raman scattering. Second is quantum theory that the intensity of Raman scattering is proportional to Kramers-Heisenberg-Dirac (K-H-D) dispersion equation [5, 6]. And whether the scattering is Raman active or not can be simply judged by K-H-D dispersion equation.

To begin with, I am going to develop K-H-D dispersion equation by quantization of a radiant field relevant to a thought that Raman scattering happens through a process of annihilation and generation of photons. A mutual effect between a molecule and a radiant field can be restated in an interaction between electrons in molecules and a radiant field. Therefore, classical Hamiltonian function of electrons is useful for mathematically expressing the interaction energy

between electrons and radiant field. Classical Hamiltonian function of an electron in electromagnetic field is given by [7],

$$H = \frac{1}{2m}\left(\vec{P} - \frac{e}{c}\vec{A}\right)^2 + e\phi \tag{1.1}$$

In this equation, m is mass of electron and e is charge and $\vec{P}$ is kinetic momentum and $\vec{A}$ is a vector potential and ϕ is scalar potential. If we neglect the effect of fields induced by electrons on themselves, it is quite sure that a vector potential $\vec{A}$ and scalar potential ϕ is purely caused by the radiant field so that ϕ=0 is assumed. Hamiltonian of an interaction between electrons and radiant field corresponds to remaining terms of Hamiltonian H after a deduction of kinetic energy of electrons $\vec{P}^2/2m$, which is described as,

$$H_Q = \frac{e}{mc}\vec{P}\vec{A} + \frac{e^2}{2mc^2}\overrightarrow{A^2} \tag{1.2}$$

where c is a speed of light. Quantized radiant field is given by.

$$4\pi^2 \sum_k \sum_l k^2 A_{kl}\overline{A_{kl}}\sigma_k^{-1} = \sum_k \sum_l h\nu_k \eta_{kl}\overline{\eta_{kl}} \tag{1.3}$$

where η_{kl} is a creation operator and $\overline{\eta_{kl}}$ is an annihilation operator for one photon with k propagating direction and l direction of electronic field. $h\nu_k$ is energy of photon with the propagating direction along k. A_{kl} is Fourier amplitude of a vector potential of light. The value denoted as σ_k^{-1} is a volume assigned to one lattice point in reciprocal space (k-space). The summation denoted as Σ_k and Σ_l is for summing up all Fourier amplitudes of vector potentials, creation operators and annihilation operators for photon in all kl modes. The equation in Eq. (1.3) implies η_{kl}, which physically represents a creation operator for "Photon", corresponds to A_{kl}, which is Fourier amplitude of a vector potential of "Light wave" used a lot in classical electrodynamics, namely we transcribe the equation used in classical physics to the one in quantum physics.

Quantization of the Hamiltonian representing an interaction between electrons and radiant field can be introduced by substituting Eq. (1.3) of quantized radiant field into Eq. (1.2),

$$H_Q = \frac{eh^{\frac{1}{2}}}{4\pi^2 m}\sum_k \sum_l P_l \nu_k^{\frac{-1}{2}}(\eta_{kl} + \overline{\eta_{kl}})\sigma_k^{\frac{-1}{2}} + \frac{e^2 h}{32\pi^4 m}\sum_k \sum_{k'} \sum_l \sum_{l'} \nu_k^{\frac{-1}{2}} \nu_{k'}^{\frac{-1}{2}}$$

$$\times(\eta_{kl}+\overline{\eta_{kl}})\times(\eta_{k'l'}+\overline{\eta_{k'l'}})\times\vec{l}\vec{l'}\sigma_k^{\frac{-1}{2}}\sigma_{k'}^{\frac{-1}{2}} \quad (1.4)$$

This is the Hamiltonian of quantized interaction between electrons and radiant field. The value denoted as k and l are discrete values of direction of propagation and field. The denotations indicate the modes of photon. The frequency of the photon in k mode is represented as ν_k. The value of $\sigma_k^{-1/2}$ is derived from the confinement effect of radiant field. The equation of $P_l(\eta_{kl}+\overline{\eta_{kl}})$, which constitute the first term in Eq. (1.4), physically indicate that a state change of molecule is caused by perturbation of P_l at the same time as a photon is generated and annihilated by η_{kl} and $\overline{\eta_{kl}}$. However, second term of Eq. (1.4) doesn't have any operators denoted as P promoting the state change, which physically means that there is no perturbation acting on a molecule. So the second term has nothing to do with scattering. Besides, Raman scattering is generated through the two-photon process with one photon generation and annihilation. Therefore, an equation corresponding to Raman scattering must be derived from second-order perturbation of the term of scattering. K-H-D dispersion equation is derived from second-order perturbation of the first term in Eq. (1.4). Here, the process through which initial state $|q\rangle$ at $t=0$ transits to final state $|s\rangle$ at $t=t$ of a certain system by the perturbation H_Q yields the following probability amplitude using state vectors.

$$b_s^{(2)}(t)=\sum_r\frac{\langle s|H_Q|r\rangle\langle r|H_Q|q\rangle}{h(\nu_r-\nu_q)}\cdot\frac{e^{2\pi i(\nu_s-\nu_q)t}-1}{h(\nu_s-\nu_q)} \quad (1.5)$$

where $h\nu_q$, $h\nu_r$ and $h\nu_s$ express energy of $|q\rangle$, $|r\rangle$ and $|s\rangle$ state, respectively. $|r\rangle$ is a state vector of an intermediate state. The probability amplitude described in Eq. (1. 5) is finally rewritten as following equations with the use of momentum operator P,

$$b_s^{(2)}(t,r_1)=\frac{\langle s|H_Q|r_1\rangle\langle r_1|H_Q|q\rangle}{h(\nu_{r_1}-\nu_q)}=\frac{e^2h}{16\pi^4m^2}\frac{\langle n|P_{l''}|e\rangle\langle e|P_{l'}|m\rangle}{h(\nu_e-\nu_m-\nu_{l'})}\times(\nu_{k'l'})^{\frac{1}{2}}(\nu_{k'}\nu_{k''}\sigma_{k'}\sigma_{k''})^{\frac{-1}{2}} \quad (1.14)$$

where $|e\rangle$, $|m\rangle$ and $|n\rangle$ are state vectors of an intermediate state, an initial state and an final state, respectively. The above equation indicates the process that one-photon in the mode $k'l'$ is absorbed and the one in the mode $k''l''$ is emitted by the Hamiltonian of quantized interaction denoted as H_Q. And the probability amplitude for another scattering process is given by,

$$b_s^{(2)}(t,r_2)=\frac{\langle s|H_Q|r_2\rangle\langle r_2|H_Q|q\rangle}{h(\nu_{r_2}-\nu_q)}=\frac{e^2h}{16\pi^4m^2}\frac{\langle n|P_{l\prime}|e\rangle\langle e|P_{l\prime\prime}|m\rangle}{h(\nu_e-\nu_m+\nu_{l\prime\prime})}\times(\nu_{k\prime l\prime})^{\frac{1}{2}}(\nu_{k\prime}\nu_{k\prime\prime}\sigma_{k\prime}\sigma_{k\prime\prime})^{\frac{-1}{2}} \quad (1.15)$$

This equation indicates the process that one-photon in the mode $k''l''$ is absorbed and that in the mode $k'l'$ is emitted by the Hamiltonian of quantized interaction denoted as H_Q. Let me spare the details for deriving Eq. (1.14-15) to avoid jumping out the rails. If you want to pursue the description for the probability amplitude written by the momentum operator of electron, please read through the details shown in *Appendix (For pp.101-102)*. By substituting Eq. (1.14-15) into Eq. (1.5) and squaring the absolute value, one can have following equation as a transition probability of Raman scattering.

$$\left|b_s^{(2)}(t)\right|^2=\frac{e^4}{128\pi^8m^4}\left|\sum_e\left\{\frac{\langle n|P_{l\prime\prime}|e\rangle\langle e|P_{l\prime}|m\rangle}{h(\nu_e-\nu_m-\nu_{l\prime})}+\frac{\langle n|P_{l\prime}|e\rangle\langle e|P_{l\prime\prime}|m\rangle}{h(\nu_e-\nu_m+\nu_{l\prime\prime})}\right\}\right|^2\times(\nu_{k\prime l\prime})(\nu_{k\prime}\nu_{k\prime\prime}\sigma_{k\prime}\sigma_{k\prime\prime})^{-1}\cdot$$

$$\frac{1-\cos 2\pi(\nu_n-\nu_m+\nu_{k\prime\prime}-\nu_{k\prime})t}{(\nu_n-\nu_m+\nu_{k\prime\prime}-\nu_{k\prime})^2} \quad (1.16)$$

Taking the summation of the equation with k' and k'' for an integration of whole incident and scattering components, one has following equation,

$$P=\iint\left|b_s^{(2)}(t)\right|^2d^3\overrightarrow{k'}\,d^3\overrightarrow{k''} \quad (1.17)$$

This is the total probability of Raman transition from $|m\rangle$ to $|n\rangle$ occurring on molecules under radiant field during t=0 to t=t. Expressing the equation with the use of Fourier components of vector potential leads to the following equation,

$$P=\iiint|A_{l''l'}|^2\,\nu_{k'l'}\nu_{k'}(\nu_{k'}+\nu_m-\nu_n)d\nu_{k'}d\omega_{k'}d\omega_{k''} \quad (1.18)$$

$$A_{l''l'}=\frac{e^2}{m^2}\sum_e\left\{\frac{\langle n|P_{l\prime\prime}|e\rangle\langle e|P_{l\prime}|m\rangle}{h(\nu_e-\nu_m-\nu_{k\prime})}+\frac{\langle n|P_{l\prime}|e\rangle\langle e|P_{l\prime\prime}|m\rangle}{h(\nu_e-\nu_n+\nu_{k\prime})}\right\} \quad (1.19)$$

The frequency of a scattering is derived by using that of incident light and Raman shift as follows $(\nu_{k'}+\nu_m-\nu_n)=\nu_{k''}$. Although the Fourier component of vector potential A is written by the momentum of electron in a molecule P, the above equation in Eq. (1.18) and Eq. (1.19) are needed for being rewritten as a formula with electric dipole moment R for easier comprehension of the electronic interaction,

$$\langle n|P_l|m\rangle = -\frac{2\pi i m}{e\hbar}(\nu_m - \nu_n)\langle n|R_l|m\rangle \tag{1.20}$$

This equation is obtained with the Heisenberg equation of motion expressed by P and R,

$$\frac{dR_l}{dt} = \frac{1}{ih}(R_l H_e - H_e R_l) \tag{1.21}$$

where H_e is the Hamiltonian for electronic state of a molecule. By substituting the equation Eq. (1.20) into Eq. (1.19), the expression for the Fourier component A is rewritten with the use of the electric dipole moment R.

$$A_{l''l'} = \frac{4\pi^2}{h^2}\sum_e'(\nu_e - \nu_m)(\nu_e - \nu_n)\times\left\{\frac{\langle n|R_{l''}|e\rangle\langle e|R_{l'}|m\rangle}{h(\nu_e - \nu_m - \nu_{k'})} + \frac{\langle n|R_{l'}|e\rangle\langle e|R_{l''}|m\rangle}{h(\nu_e - \nu_n + \nu_{k'})}\right\} \tag{1.22}$$

Furthermore, Eq. (1.22) is simplified as a following formula,

$$A_{l''l'} = \frac{4\pi^2}{h^2}\nu_{k'}(\nu_{k'} + \nu_m - \nu_n)\sum_e'\left\{\frac{\langle n|R_{l''}|e\rangle\langle e|R_{l'}|m\rangle}{h(\nu_e - \nu_m - \nu_{k'})} + \frac{\langle n|R_{l'}|e\rangle\langle e|R_{l''}|m\rangle}{h(\nu_e - \nu_n + \nu_{k'})}\right\} \tag{1.23}$$

Let's think about a possibility to obtain a scattering with propagation vector k_s and electric field direction l_s from an incident light with propagation vector k_i and electric field direction l_i. $\nu_{k'l'}$ in Eq. (1. 18) has constant value only within $\Delta\nu_i$, $\Delta\omega_i$ and $\Delta\omega_s$ otherwise it is zero value. Therefore, the integral interval in Eq. (1.18) is simply converged in the range of $\Delta\nu_i\Delta\omega_i\Delta\omega_s$ and the following equation can be derived with the integration operator $\iiint$ excluded,

$$P = \frac{t}{c^6}|A_{l''l'}|^2\nu_{k_i l_i}\nu_{k_i}(\nu_{k_i} + \nu_m - \nu_n)\Delta\nu_i\Delta\omega_i\Delta\omega_s \tag{1.24}$$

Energy of photon scattered into solid angle of $\Delta\omega_s$ per unit time is given by multiplying $h\nu_{k_s} = h\nu_{k_i}(\nu_{k_i} + \nu_m - \nu_n)$ to Eq. (1.24) and dividing it by time t, then we have the following equation,

$$W_{k_s l_s}\Delta\omega_s = \frac{1}{c^6}|A_{l''l'}|^2\nu_{k_i l_i}\nu_{k_i}(\nu_{k_i} + \nu_m - \nu_n)^2\Delta\nu_i\Delta\omega_i\Delta\omega_s \tag{1.25}$$

A total radiant energy from an incident photon in $\Delta\nu_i$ and $\Delta\omega_i$ is equal to the equation $(L^3 h{\nu_{k_i}}^3\nu_{k_i l_i}/c^3)\cdot\Delta\nu_i\Delta\omega_i$. A density of energy in a unit of time is derived from dividing the total radiant energy by L^3/c, then we have,

$$I_{k_i l_i} = \frac{h\nu_{k_i}{}^3 \nu_{k_i l_i}}{c^3} \Delta\nu_i \Delta\omega_i \cdot c \tag{1.26}$$

This value is intensity of light in spectroscopy. With Eq. (1.26) and Eq. (1.23), Eq. (1.25) indicates the relation between vector potential and electric dipole moment, which is expressed as follows,

$$E_{k_s \rho} = \frac{16\pi^4 (\nu_0 + \nu_m - \nu_n)^4}{c^4} \left| a_{\rho\sigma} \right|^2 I_{k_i \sigma} \tag{1.27}$$

$$a_{\rho\sigma} = \sum_e' \left\{ \frac{\langle n|R_\sigma|e\rangle\langle e|R_\rho|m\rangle}{h(\nu_e - \nu_m - \nu_0)} + \frac{\langle n|R_\rho|e\rangle\langle e|R_\sigma|m\rangle}{h(\nu_e - \nu_n + \nu_0)} \right\} \tag{1.28}$$

where l_i and l_s indicate the polarization directions of electronic field for incident light and scattering light each in space-fixed system of coordinates correspond with σ and ρ ($\sigma, \rho = x, y, z$) in molecule-fixed system of coordinates. The propagating directions of incident light and that of scattered light are denoted as k_i and k_s. Here, we have Kramers-Heisenberg-Dirac (K-H-D) dispersion formula written as Eq. (1.28). The equation is the expression for the cross section of one photon scattering by an atomic electron. $\langle e|R_\rho|m\rangle$ in the first term represents that an incident light polarized in ρ direction disappear and $\langle n|R_\sigma|e\rangle$ represents that a scattering light polarized in σ direction appears. Eq. (1.27) indicates the intensity of incident light $I_{k_i \sigma}$ generates the intensity of Raman scattering $E_{k_s \rho}$. Eq. (1.28) determines whether it is Raman active or not. Adding more, Eq. (1.27) is often used for polarized Raman scattering measurements. For example, if you illuminate the light from X direction in space fixed system of coordinates and detects scattering from Y direction in space fixed system of coordinates, all you need to observe is $X(e_\rho, e_\sigma)Y$, which is a general writing style known as Porto notation used for finding the value of $a_{\rho\sigma}$ from the given experimental configuration. The vector value e_ρ and e_σ are the polarization directions of electronic field for incident light and scattering light, respectively. By the combination of electric field direction ρ with σ, $\rho\sigma$ component in Raman tensor $a_{\rho\sigma}$ can be calculated. More general expression of Eq. (1.27) is written as $I \propto \left| e_i \cdot a_{\rho\sigma} \cdot e_s \right|^2$, which is for the case that l_i and l_s electronic field directions for incident light and scattering light doesn't correspond with σ and ρ components for Raman tensor $a_{\rho\sigma}$.

Selection rule of Raman scattering and symmetric property of states of molecule

Relation between irreducible representations of states of molecule and Raman scattering tensor operator gives selection rule for Raman scattering, which simply expressed as $\Gamma_m \times \Gamma_n \subset \sum \Gamma_{\rho\sigma}$. Γ_m, Γ_n and $\sum \Gamma_{\rho\sigma}$ denote irreducible representations of initial state, final state and Raman scattering tensor operator. Here, I try to derive the selection rule from K-H-D dispersion formula. K-H-D dispersion formula expressed in (1.28) is transcribed as the following equations,

$$a_{\rho\sigma} = \langle m | \widehat{a_{\rho\sigma}} | n \rangle \tag{1.29}$$

$$\widehat{a_{\rho\sigma}} = \sum_{e \neq m,n} \left\{ \frac{R_\sigma |e\rangle\langle e| R_\rho}{h(\nu_e - \nu_m - \nu_i) - i\Gamma_e} + \frac{R_\rho |e\rangle\langle e| R_\sigma}{h(\nu_e - \nu_n + \nu_i) - i\Gamma_e} \right\} \tag{1.30}$$

where $\widehat{a_{\rho\sigma}}$ is $\rho\sigma$ component in the Raman scattering tensor operator and Γ_e is a damping constant for avoiding the situation that the denominator of $h(\nu_e - \nu_m - \nu_i)$ is close to infinite and R is an electric dipole moment of molecule. Raman scattering tensor operator $\widehat{a_{\rho\sigma}}$ physically means the capability of responding to electric field, which is a corresponding value to polarizability tensor in classical theory. Initial state $|m\rangle$ is in ground vibrational state |0) on ground electronic state [g] and final state $|n\rangle$ is in first excited vibrational state |1) on ground electronic state [g]. Adding more, if intermediate states $|e\rangle$ were expressed as a following general state, we can make Eq. (1.29) more clear form.

$$|e\rangle = \sum_{e \neq g} |e] \sum |v) = |e]|v) \tag{1.31}$$

where |] or |) is state vector representing electronic or vibrational state, respectively. $\sum_{e \neq g} |e]$ and $\sum |v)$ are represented as $|e]$ and $|v)$ for convenience. Removed summations expressed as Σ|v)(v|=1 in Poncelet's closure theorem, we can ignore contributions from all vibrational state during intermediate state, then we have the following equations.

$$a(1 \leftarrow 0) = (0|\alpha|1) \tag{1.32}$$

$$\alpha_{\rho\sigma} = \sum_e \left\{ \frac{[g|R_\sigma|e][e|R_\rho|g]}{h(\nu_e - \nu_m - \nu_0)} + \frac{[g|R_\sigma|e][e|R_\rho|g]}{h(\nu_e - \nu_n + \nu_0)} \right\} \tag{1.33}$$

where $|0)$ is a ground vibrational state and $|1)$ is an excited vibrational state. The Poncelet's closure theorem approximate Raman tensor a with vibrational matrix element $|0)$ and $|1)$ of polarizability α. Polarizability tensor α is an operator depending on a core point of molecule. This polarizability tensor can be expanded into power series of Q_a around an equilibrium position because a molecule vibration is small oscillation along base coordinates around an equilibrium position, which is described as,

$$\alpha_{\rho\sigma} = {\alpha_{\rho\sigma}}^0 + \sum_a \left(\frac{\partial \alpha_{\rho\sigma}}{\partial Q_a}\right)_0 Q_a + \cdots \tag{1.34}$$

By substituting Eq. (1.34) into Eq. (1.33),

$$a(1 \leftarrow 0) = \frac{1}{\sqrt{2}} \varepsilon_a \left(\frac{\partial \alpha_{\rho\sigma}}{\partial Q_a}\right)_0 \tag{1.35}$$

is given. This equation indicates that Raman tensor of fundamental tone on mode a near an equilibrium position is proportional to an amplitude of normal vibration and derivative of polarizability tensor $\alpha_{\rho\sigma}$ at Q_a. Eq. (1.35) is a basic formula of Placzek polarizability theory for the theoretical treatment of bond polarizability [8]. Symmetric property of polarizability tensor has to be same with that of base coordinates Q_a for obtaining a finite value of Raman scattering. In terms of group theory, Raman is active only if linear combination of irreducible representations of a polarizability tensor $\alpha_{\rho\sigma}$, which is expressed as $\sum \Gamma_{\rho\sigma}$, belongs to that of base coordinates on a molecule Q_a expressed as Γ_a.

$$\Gamma_a \subset \sum \Gamma_{\rho\sigma} \tag{1.36}$$

This is the selection rule for vibrational Raman scattering with Placzek polarizability theory. To derive the general selection rule, we can take a different path.

For detecting Raman scattering, $a(n \leftarrow m) = (m|\alpha|n)$ must have non-zero value. In terms of group theory, a direct product of $(m|\alpha|n)$ must belong to totally symmetric representation, which is denoted as A, because the value is integrated over a whole space and must be invariant against all operations of symmetry group to which the molecule belongs. To obtain a totally symmetric representation from the direct product of $\Gamma_m \times \Gamma_n \times \sum \Gamma_{\rho\sigma}$, the obtained irreducible representation is required to equal A, where Γ_m, Γ_n and $\sum \Gamma_{\rho\sigma}$ are irreducible representations

of an initial state $|m\rangle$, a final state $|n\rangle$ and linear combination of irreducible representations of $\rho\sigma$ component of an operator of Raman tensor. This is also written as,

$$\Gamma_m \times \Gamma_n \subset \sum \Gamma_{\rho\sigma} \tag{1.37}$$

Eq. (1.37) is completely same as Eq. (1.36) in principle because $\Gamma_m \times \Gamma_n$ is always equals to Γ_a due to symmetric property of vibrational motion.

In either a resonance or pre-resonance condition that the energy of photon goes up to or close to excited electronic state, we can't use Placzek polarizability theory. The value of $\alpha_{\rho\sigma}$ is practically determined by $\sum_i \delta_{ie}|e]\sum|v) = |e]\sum|v)$ or by $\sum_i \delta_{ie}|e]\sum_i \delta_{iv}|v) = |e]|v)$, which indicate a pre-resonance and a rigorous resonance Raman scattering, respectively [see Fig. 3].

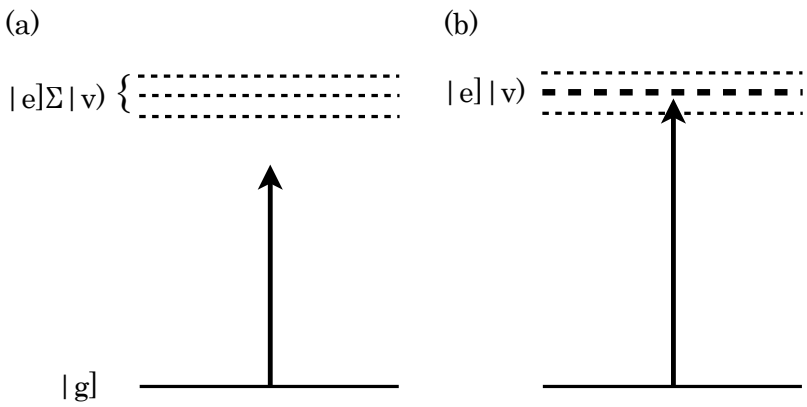

Fig. 3 | Jablonski-diagram illustrates (a) pre-resonance Raman scattering and (b) a rigorous resonance Raman scattering.

In the case of Fig. 3 (a), only one electronic state contributes to an operator of Raman tensor but all vibrational state in the electronic state have on an operator of Raman tensor, which can be seen as $\sum_i \delta_{ie}|e]\sum|v) = |e]\sum|v)$ in K-H-D equation. Fig. 3 (b) shows only one vibrational state contributes to an operator of Raman tensor, which is described as $\sum_i \delta_{ie}|e]\sum_i \delta_{iv}|v) = |e]|v)$.

In these cases, the irreducible representation of intermediate state has significant role for selection rules, which leads to a more strict condition expressed as,

$$\Gamma_a \subset \Gamma_{\rho\sigma} \tag{1.38}$$

Selection rules of Raman scattering of crystal

Since a single walled carbon nanotube (SWCNT) has crystal structure composed of well-ordered six-membered carbon rings, selection rules derived from translation symmetries has to be considered. In the case that each element in crystal moves periodically, it is natural that polarizability of each element changes periodically, which is expressed as follows [9, 10].

$$\overrightarrow{a_n} = \overrightarrow{a_0} + \overrightarrow{a_1}\cos(2\pi\nu_R t - \overrightarrow{k_R}\cdot\overrightarrow{r_n}) \tag{1.39}$$

where $\overrightarrow{k_R}$ is phase vector of periodic motion of each element and $\overrightarrow{r_n}$ is position in n element. a_0 is time-independent polarizability and a_1 is time-dependent polarizability. ν_R is the frequency of periodic motion of molecules. The second term of Eq. (1.39) is a relevant term with Raman scattering. The selection rule for Raman scattering from crystal is determined by translation symmetry of element and symmetry of Bravais lattice. Translation symmetry of crystal is reflected in the cosine function of the second term. Symmetry of Bravais lattice defines the symmetry of a_1 in the second term.

The equation of electric field component of second radiant wave from crystal, which is described as $E_s \propto \sum_n \cos\{2\pi\nu_s t - \overrightarrow{k_s}\cdot\vec{R} - (\overrightarrow{k_i} - \overrightarrow{k_s} - \overrightarrow{k_R})\}$, gives the requirement to obtain Raman scattering from crystal given by,

$$\overrightarrow{k_R} = \pm(\overrightarrow{k_i} - \overrightarrow{k_s}) \tag{1.40}$$

where k_i and k_s are allowed wave vector of incident light and scattering light. $\vec{R}$ is position vector of observation point. The phase vector k_R of Eq. (1.40) is within the following closed interval,

$$k_i - k_s \le k_R \le k_i + k_s \tag{1.41}$$

The phase vector is physically useless except for its being within Brillouin Zone. The range of Brillouin Zone is expressed as follows,

$$-\frac{\pi}{a} \le k_R \le \frac{\pi}{a} = \pi\times10^7\ cm^{-1} \tag{1.42}$$

where a is lattice constant for space between neighboring lattices. With visible light, the phase vector ineluctably satisfy $k_i + k_s \ll \frac{\pi}{a}$ because Brillouin Zone is far bigger than the allowed

region described as $k_R \leq k_i + k_s \approx 10^5\ cm^{-1} \ll \frac{\pi}{a} = \pi \times 10^7\ cm^{-1}$. That means Raman scattering occurs only in very limited region around $k_R = 0$

$$k_R = 0 \tag{1.41}$$

Eq. (1.41) restricts the phase of the cyclic motion of the crystal. That means Raman scattering only occurs in the vicinity of Γ point. Fig. 4 shows dispersion curve of phonons of graphite. In graphite, there are six *Γ* phonons, i.e., the out-of-plane transverse acoustic (oTA), longitudinal acoustic (LA), in-plane transverse acoustic (iTA), out-of-plane transverse optical (oTO), in-plane TO (iTO), and longitudinal optical (LO) modes listed in order of increasing phonon frequency. At Γ point, we have phonons near 1600 cm^{-1}, 800 cm^{-1} and 100 cm^{-1}. That's why we have Raman spectra whose frequency located on these Raman shifts.

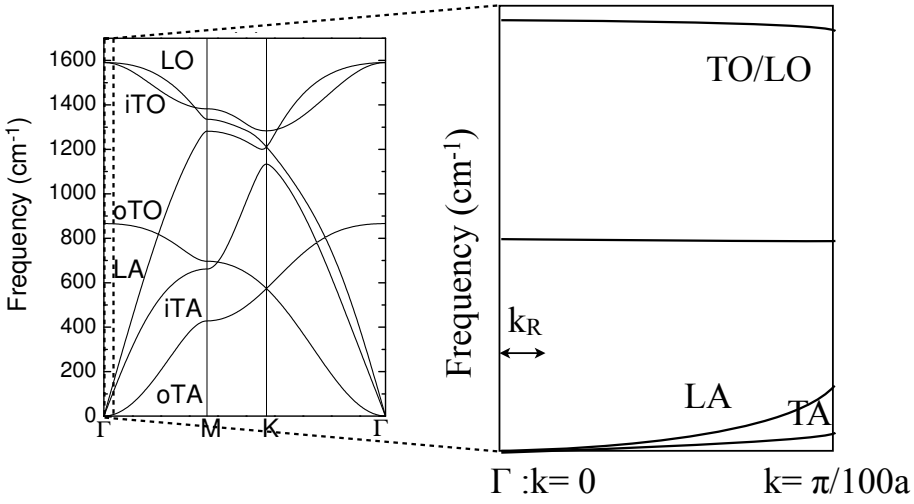

Fig. 4 | Dispersion curve of phonon of graphene and dispersion curve near k=0, calculated in following report [11].

Provided that $k_R = 0$, Raman scattering from crystals is treated equally with that from molecule. This is because the equation of polarizability of molecule is described as $\overrightarrow{a_n} = \overrightarrow{a_0} + \overrightarrow{a_1}\cos(2\pi\nu_R t)$, which is same as $\overrightarrow{a_n} = \overrightarrow{a_0} + \overrightarrow{a_1}\cos(2\pi\nu_R t - \overrightarrow{k_R}\cdot\overrightarrow{r_n})$ derived from that of crystal. In the above condition, Raman scattering of crystals depends on symmetric property of Bravais lattice, which is reflected in time-dependent polarizability $\overrightarrow{a_1}$.

1-2. Introduction of SWCNTs and its Raman scattering

Single walled carbon nanotubes (SWCNTs) have become a standard material in nanotechnology and a wide variety of applications using nanotubes have been proposed and investigated intensively due to its having 1D nano-structure which provides a wealth of electronic and mechanical property. However, there are unknown properties concealed in SWCNTs, which inhibited their practical applications. One of the most attractive subjects is to reveal intrinsic properties of them in a simple and quick way. To apply SWCNTs into nanotechnology, we need the information of following points: 1) the purity of SWCNTs 2) diameter and chirality 3) whether it is metallic or semiconducting 4) whether a perfect or defective crystal 5) strains applied to SWCNTs. Raman spectroscopy is a non-destructive measurement which is powerful tool for investigating the intrinsic properties in a simple and quick way. Rao et al. showed the Raman signal from the carbon nanotube not only consists of the graphite-oriented A1, E1 and E2 (for armchair, A1g, E1g and E2g) modes but also contains a strong low frequency A_g-active mode in its spectrum, known as radial breathing mode (RBM), which is special to the diameter of SWCNT [22]. The result was in good agreement with lattice dynamics calculations and precisely characterized their physical properties, which fuel researcher's motivation to apply Raman scattering for their evaluation. In this session, firstly, I explain fundamental physics of SWCNTs about geometry and electronic properties. Then I introduce the Raman scattering of SWCNTs and how to utilize it for the characterization of SWCNTs.

Physical property of SWCNT

A SWCNT is depicted as a single layer of a graphite crystal that is rolled up into a seamless cylinder. Each SWCNT is specified by the chiral vector $C_h = na_1 + ma_2$, where n and m are integers and where a_1 and a_2 are unit vectors of graphene layer, as shown on Fig. 5.

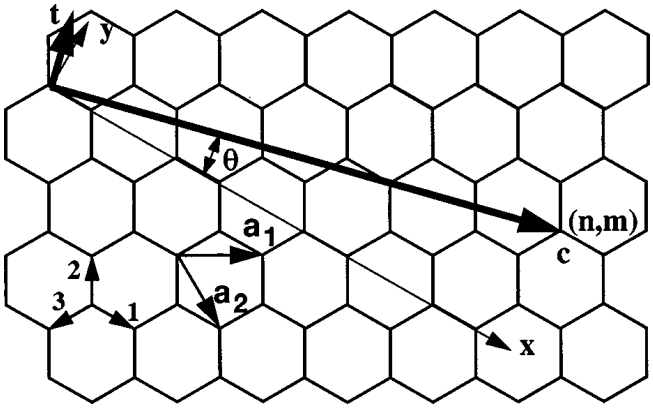

Fig. 5 | The fixed (x,y) and chirality dependent (n, m) coordinates. r_1 , r_2, and r_3 correspond to bonds 1, 2, and 3, respectively. a_1 and a_2 are the lattice vectors of the two dimensional sheet [23].

Using above integers, types of SWCNTs are simply expressed by the pair of indices (n, m), which is called chirality. The chirality provides information about electronic and mechanical property. The diameter d of the SWCNTs is calculated by using chirality. It is expressed with (n, m) as $d = |C_h/\pi| = a\sqrt{(n^2 + m^2 + nm/\pi)}$, where a=$|a_1|$=$|a_2|$=2.46Å is three times as long as the nearest C-C distance.

The electronic σ bands binding each neighboring C atoms build the strong planar covalent bonds over the 2D graphene sheets, while the π bands gives weak van der Waals interactions between graphene sheets in graphite. The π bands are closer to the Fermi level than the σ bands, so that electrons can be excited from the valence (π) to the conduction (π∗) band optically. The electronic structure of a SWCNT can be obtained from 2D graphite as shown in Fig. 6(a), but in the case of SWCNTs, the quantum confinement of the 1D electronic states must be taken into account because SWCNTs has a rolled up structure of 2D graphite, which gives Periodic Boundary Condition in C_h vector. That's why the cutting lines of allowed wave vectors can be represented in the 2D graphene sheet Brillouin zone [see Fig. 7].

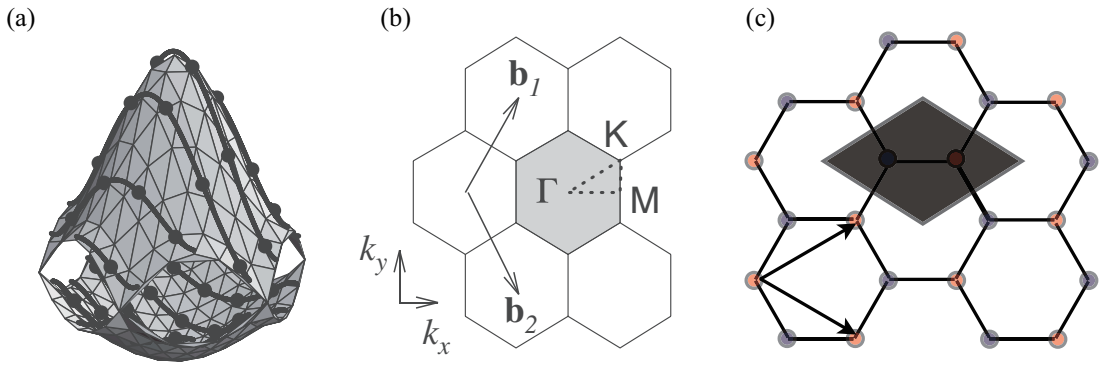

Fig. 6 | (a) shows the electronic dispersion for the π and π∗ bands of 2D graphite in the first Brillouin zone, obtained with the tight binding (TB) method. The optical transitions occur close to the corners of the Brillouin zone, called the *K* points, where the valence and conduction bands touch each other and near Fermi energy [M. S. Dresselhaus et. al., "Raman spectroscopy of carbon nanotubes" Physics Report, (2005)]. (b) shows Brillouin zone of grapheme sheet. k_x and k_y are reciprocal space axes. *Γ* and *K* point are the position where the wavenumber equals to 0 and $(2n + m)|K_1|/3$ respectively. *M* point is a fractional coordinate, which gives the edge of unit cell in reciprocal lattice space. (c) Unit cell of grahene sheet described as a shallow black area, which includes 2 carbon atoms.

The optical absorption or emission of SWCNTs is related primarily to the electronic states at the van Hove singularities (vHSs) closer to the Fermi level. The vHSs related to optical absorption/emission originate from the cutting lines closer to the *K* point in the 2D Brillouin zone as shown in Fig. 6(b). 2D Brillouin zone of graphene is calculated by taking inverse of the unit cells shown in Fig. 6(b). Each unit cell has two carbon atoms colored as red and blue as shown in Fig. 6(c). By using the 2D Brillouin zone, SWCNTs can be classified into three different classes, according to whether MOD (2n + m, 3) = 0, 1 or 2, where the integers 0, 1, 2 denote the remainders when (2n + m) is divided by 3 as shown right panels in Fig. 7. This classification is based on the fact that the distance from *Γ* to *K* point equals to $(2n + m)|K_1|/3$ where K_1 is a unit reciprocal vector that is in inverse proportion to diameter of nanotube.

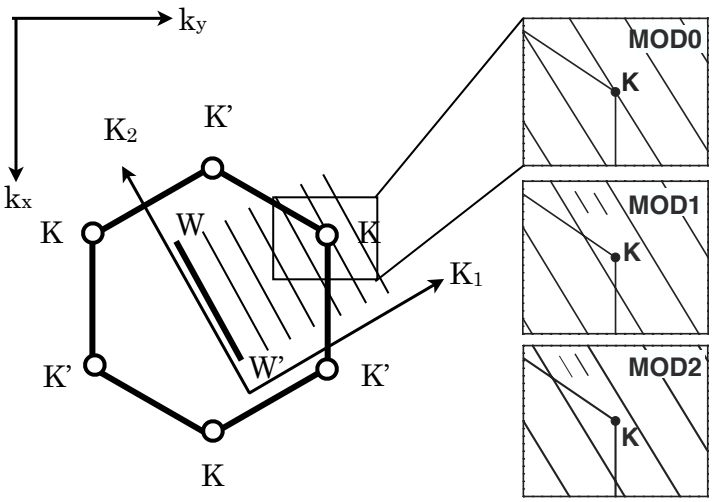

Fig. 7 | Cutting line in Brillouin zone of graphene is shown in left scheme. This cutting line is defined by chirality of carbon nanotube. K1 and K2 are decided by inverse components of a chiral vector and translation vector. And right panel shows how the feature of electronic property of nanotube is decided. Only MOD 0 has a cutting line at K-point, which means this chiral nanotube is metal.

Here, MOD1 and MOD2 SWCNTs are two types of semiconducting nanotubes, since allowed *k* vectors (cutting lines) don't cross the *K* point. Regarding MOD0 SWCNTs, a cutting line crosses the *K* point. The cutting line classifies SWCNTs as metal.

I show here the typical electronic dispersion relation and the typical vHSs of semiconducting carbon nanotubes, whose chirality is (10, 0) in Fig. 8 (a) and (b), respectively.

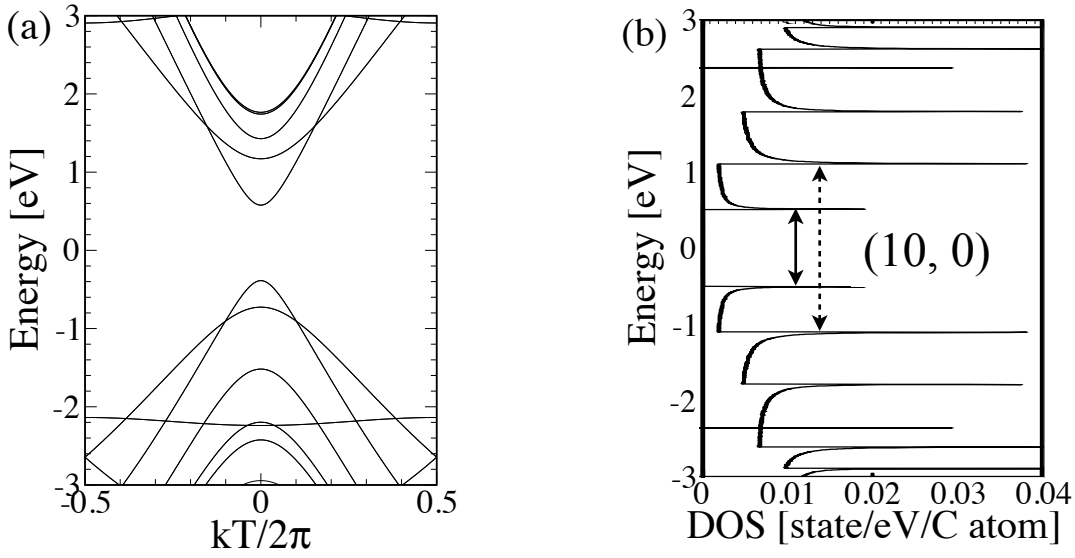

Fig. 8 | (a) shows 1D electronic dispersion relation of carbon nanotubes (10, 0) near E_F. (10, 0) nanotube has a band gap at the point where the wavenumber equals to 0, which is very feature of semiconducting material. (b) shows vHSs of (10, 0) nanotube. E_{11} is denoted as a solid arrow and E_{22} is denoted as a dotted arrow.

Fig. 8(a) shows conduction band and valence band near E_F do not cross together. In this case, the nanotube has a semiconducting feature. The energy of absorbed light is determined by the band gap corresponding to energy difference between first or second vHSs in valence band and in conduction band, each of which is called E_{11} or E_{22}. In general, light is absorbed when the energy of light corresponds to E_{22} denoted as a dotted arrow in Fig. 8(b). After that, SWCNT emit the light whose energy corresponds to E_{11} denoted as a solid arrow in Fig. 8(b).

I show next the typical electronic dispersion relation and the typical vHSs of metal carbon nanotubes, whose chirality is (10, 10) in Fig. 9(a) and (b), respectively.

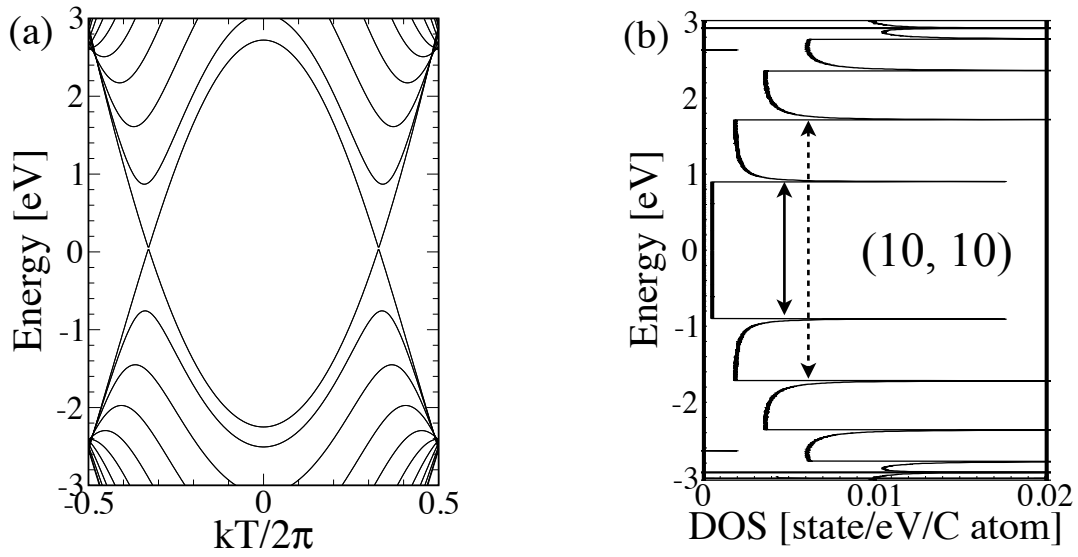

Fig. 9 | (a) shows 1D electronic dispersion relation of carbon nanotubes (10, 10) near E_F. (10, 10) nanotube has no band gap because a cutting line pass through K-point, which indicates this nanotube is metallic material. (b) shows vHSs of (10, 10) nanotube. E_{11} is denoted as a solid arrow and E_{22} is denoted as a dotted arrow.

Fig. 9(a) shows conduction band and valence band near E_F cross together. In this case, the nanotube have metal feature. It provides optical absorption when inter peak between vHSs correspond to the energy of light but no fluorescence can be obtained. Electrons in the nanotube always move freely owing to no band gap near E_F.

The 2D graphene sheet has two atoms per unit cell, thus having 6 phonon branches as shown in Fig. 4. Since the SWCNT is based on a 2D graphene sheet that has been rolled up seamlessly, a similar folding procedure is applied to obtain the phonon dispersion relations and phonon density of states for SWCNTs. The phonon dispersion for a (10,10) SWCNT is obtained by this folding procedure. The phonon dispersion is illustrated in Fig. 10 (a), and the relevant phonon density of states (DOS) is shown in Fig. 10 (b). The large amount of sharp structure in the phonon DOS reflects the many phonon branches derived from the quantum confinement of the phonon states.

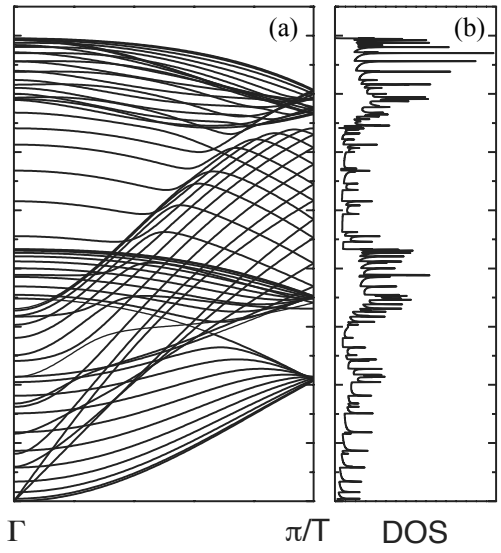

Fig. 10 | (a) The calculated phonon dispersion relations of an armchair carbon nanotube with (n, m) = (10, 10), for which there are 120 degrees of freedom and 66 distinct phonon branches [12], calculated from by using the zone folding procedure. (b) The corresponding phonon density of states (DOS) for a (10,10) nanotube.

Carbon nanotubes also exhibit other unusual aspects regarding their phonon dispersion relations, such as four acoustic branches. In addition to LA and TA modes, there are two acoustic twist modes for rigid rotation around the tube axis, which are important for heat transport and charge carrier scattering. Also important for coupling electrons to the lattice are the low-lying optical modes at the center of the Brillouin zone q = 0. These modes include one with E_2 symmetry expected at ~ 17 cm^{-1}, one with E_1 symmetry, expected at ~ 118cm^{-1}, and one with *A* symmetry expected at ~ 165 cm^{-1} for a (10,10) SWCNT [11]. Among these three low-energy phonon modes, it is only the radial breathing mode (RBM) that is attributable to *A* symmetry. And a vibrational motion in plane directions of nanotubes is reflected at ~ 1590 cm^{-1}. And quantum confinement appears as splits in the modes near ~ 1590 cm^{-1}. The most interesting details about the rich phonon structure of carbon nanotubes will be discussed in the next sections.

Raman scattering of SWCNT

The number of emitted phonons before relaxation of the lattice can be one, two, and so on, which we call, respectively, one-phonon, two-phonon and multi-phonon Raman processes. The order of a scattering event is defined as its number in the sequence of the total scattering events, including elastic scattering by an imperfection (such as a defect or edge) of the crystal, which occurs through the higher order process (two-phonon or multi-phonon). Second-order Raman scattering is the process with two scattering events. The lowest order process is first-order Raman scattering process with one scattering event which gives Raman spectra involving one-phonon emission. A scattering event with only elastic scattering, i.e., change of photon direction but no frequency shift, corresponds to Rayleigh scattering of light [M. S. Dresselhaus et. al., "Raman spectroscopy of carbon nanotubes" Physics Report, (2005)].

Raman active modes in carbon nanotube are shown in below with irreducible representations.

$$Raman\ active:$$

$$\Gamma = 2A_1 + 3E_{1g} + 3E_{2g} \text{ (For zig-zag)}$$
$$\Gamma = 2A_1 + 2E_{1g} + 4E_{2g} \text{ (For armchair)}$$

The two A_1 phonons are the RBM and high energy longitudinal mode (G+ mode) for zig-zag nanotube and transverse (G- mode) for armchair nanotube. E_{1g} and E_{2g} modes usually belongs to G-band. From now, I explain the first-order Raman peak known as G-band and RBM and second order Raman peak known as D-band.

G-band

A Raman-active mode of G-band appearing at 1585cm^{-1} originate from LO (Longitudinal Optic) mode and TO (Traverse Optic) mode of graphite degenerated near Γ point of Brillouin zone (q=0), both of which are Raman active as A_1, E_1 and E_2 symmetry. A phonon dispersive relation of graphite is shown on Fig. 4. In the case of carbon nanotubes, LO mode and TO mode are separated at zone center (q=0) owing to resolving a degeneracy caused by cylinder geometry, which I mentioned above as a quantum confinement, and they appear as G+ mode and G- mode. Fig. 11 (a) and (b) show the vibration direction of G+ and of G- mode occurring at Γ point.

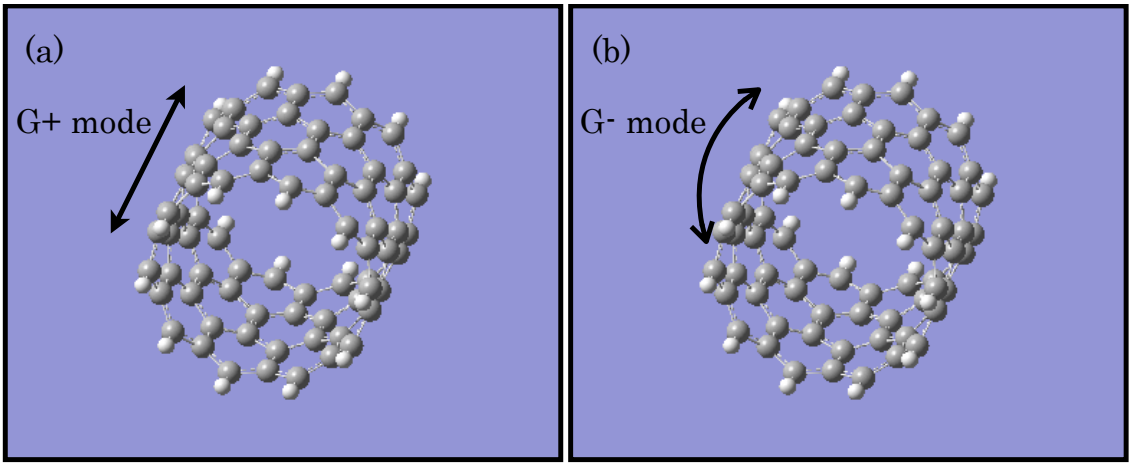

Fig. 11 | (a) shows G+ mode, which is a normal vibrational motion in nanotube axis, which is LO mode. (b) shows G- mode, which is a normal vibrational motion in circumferential direction of the nanotube, which is iTO mode.

For more detailed explanation of G+ and G- modes, I show the projection of Raman active displacement patterns of G-band in armchair nanotube in Fig. 12.

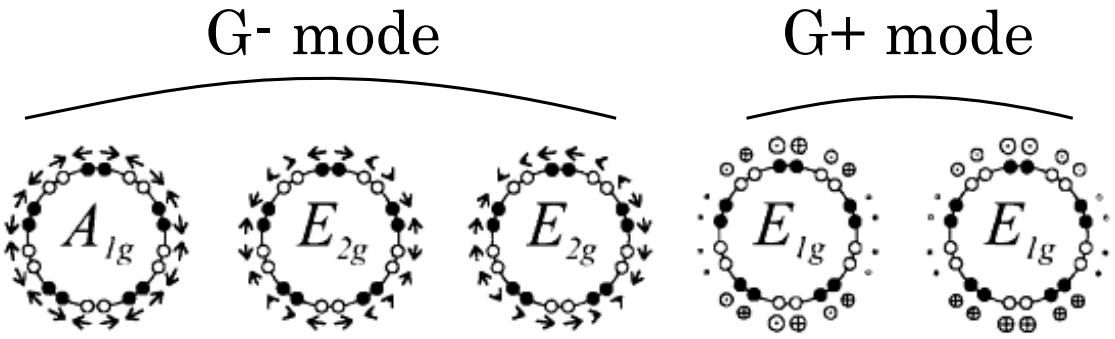

Fig. 12 | Projection of Raman-active displacement of G-band in an armchair nanotube.

As you can see from Fig. 12, E_{1g} modes of armchair nanotube are singled out as LO mode where carbon atoms vibrate in axial, which comes to be in G+ mode. E_{2g} and A_{1g} modes constitute iTO mode, which belongs to G- mode. However, E_{1g} mode has vibrations in axial direction in armchair but circumferential direction in zig-zag, which means we can't single out E_{1g} as LO mode. And A_{1g} mode constitute LO mode in zig-zag. So unless we can separate chiral nanotube perfectly, we can not distinguish the origin of each eigenvector in G-band. In usual, polarized Raman scattering measurement is used for identification of the eigenvector.

D-band

D-band has been considered as one-phonon double resonant Raman scattering mode through a second order Raman process, which is given by one-phonon inelastic scattering and elastic scattering. D-band is observed at around 1350 cm^{-1}, which is not a group theory predicted but be said to be caused by defects on SWCNTs [10]. Second-order Raman scattering usually consists of (1) two-phonon scattering events, or (2) one-phonon and one-elastic scattering event. In electronic band structure of carbon materials, such as graphite and carbon nanotubes, excited electrons appear only nearby K points located on the corner of Brillouin zone because graphite and carbon nanotube both have Fermi energy at K points. If the summation of q vector, which is wave vector of phonon, is equals to 0 value, Raman scattering happens and can become detectable even in K point but weak compared to G-band signal. Double resonance (DR) Raman theory [18] works well for explaining a non-zone-center (except for Γ point) phonon mode and a second-order Raman process [16,17,19,20].

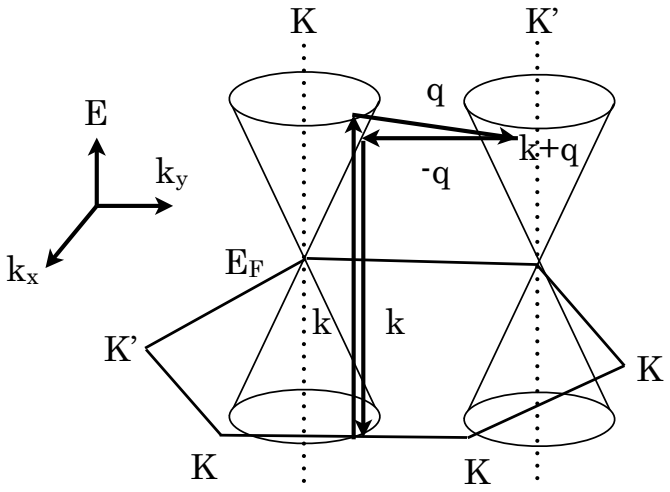

Fig. 13 | One-phonon second-order Resonance Raman spectral processes. For one-phonon, second-order transitions, one of the two scattering events is an elastic scattering event. Resonance points are shown as solid circles. See text for details.

Fig. 13 depicts the scheme of the second-order DR Raman processes near K points. In the process, the electron (1) absorbs a photon at a **k** state, (2) scatters to **k** + **q** states by elastic or inelastic scattering, (3) scatters back to a **k** state by inelastic or elastic scattering, and (4) emits a

photon by recombining with a hole at a **k** state. The scattering processes of either elastic scattering or inelastic scattering are caused by defects of the crystal or by emitting a phonon.

In a DR Raman process, there are the electrons excited around K point (near the Fermi surface) scattered to K' point by phonon modes near the K point. This phenomenon is called "intervalley scattering", which is shown on Fig. 13 and on upper part of Fig. 14. On the other hands, the process caused by the electrons excited near the K point scattered to the same K point by the phonon modes around the **Γ** point is called "intravalley scattering". D band belongs to intervalley scattering. The initial (or final) *k* and the intermediate k + q state exist on the equi-energy contour of the electronic structure. An equi-energy contour of graphite is a circle as you see around the *K* and *K*' points in the 2D Brillouin zone shown in Fig. 14. As a result, the possible *q* states are on many circles made by rotating them around *K''* point. In this case, the density of states for possible *q* states becomes singular for q = 0 and 2k, both of which we have near **K** point and far from **K** point, respectively [20]. Thus there are two double resonance peaks corresponding to the q = 0 and 2k conditions. For the peak at q = 0, the corresponding phonon frequency does not depend on laser energy, while for the peak at q = 2k the corresponding phonon frequency change dependent on laser energy. Therefore, D-band has a dispersive behavior with energy of laser light.

This dispersive behavior is explained using the schematic image in Fig. 13. The electronic structure of 2D graphite near the Fermi energy is linear in wave vector *k,* which is expressed by the crossed solid lines in Fig. 13. The crossing point corresponds to the Fermi energy located at the *K* point. When the laser energy increases or decreases, the resonance *k* vector for the electron moves away from or close to the *K* point. In the DR process, the corresponding *q* vector for the phonon increases with increasing *k* vector. Thus by changing the laser energy, we can observe the electronic structure along the phonon dispersion relations. This effect is observed experimentally as a dispersion of the phonon energy as a function of excitation laser energy [19], which is dispersive behavior. A tunable laser system can directly show this dispersive behavior in the Raman spectrum. In carbon materials, we have D-band whose phonon frequencies change with changing laser excitation energy [13–17]. We see dispersive feature in the D-band as frequency changes by 53 cm^{-1} per 1 eV in laser energy.

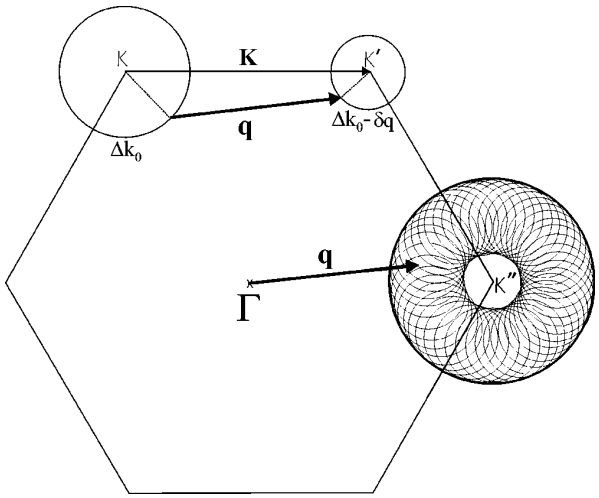

Fig. 14 | One of the possible double-resonance (DR) Stokes Raman processes involving the emission of a phonon with wave vector **q.** The set of all phonon wave vectors **q** which are related to tran- sitions from points on the two circles around *K* and *K'* gives rise to the collection of small circles around the *K''* point. Note that this collection of circles is confined to a region between the two circles with radii Δ q and 2 Δ k0- Δ q. The differences of the radii of the circles around *K* and *K'* and thus the radius of the inner circle around *K''* were artificially enlarged for clarity [21].

In 1970, Tuinstra et. al. found that the intensity of D-band can be described as the following equation.

$$\frac{I_D}{I_G} = \frac{44(\text{Å})}{L_a}$$

where L_a is the size of cluster and I_D is the intensity of D-band and I_G is the intensity of G-band. By heat treatment with high temperature, the size of cluster increases, which is caused by decline of defects. In 2005, L. G. Cancado found the relation between laser energy and L_a as follows.

$$\frac{I_D}{I_G} \propto \frac{1}{E_{laser}^4 L_a}$$

That means the intensity of D-band changes by a change of laser energy E_{laser} and amount of defects. By scrutiny of D-band, we can investigate the amount of defects and electronic band structure.

RBM

The atomic vibration of the C atoms in the radial direction is called Radial Breathing Mode (RBM). RBM is used for characterizing nanotube diameters d_t through the relation $\omega_{RBM} = A/d_t + B$, where the A and B parameters are determined experimentally [24]. For typical SWNT bundles in the diameter range $d_t = 1.5 \pm 0.2\, nm$, $A = 234\, cm^{-1} \cdot nm$ and $B = 10\, cm^{-1}$ has been found for SWCNT bundles [25]. For isolated SWCNTs on an oxidized Si substrate, $A = 248 cm^{-1} \cdot nm$ and $B = 0$ have been found [26]. Recently, it was found that $A = 227 cm^{-1} \cdot nm$ gave a reliable d_t for a given ω_{RBM} [27]. However, for $d_t < 1\, nm$, the simple $\omega_{RBM} = A/d_t + B$ relation is not expected to be applied, what with nanotube lattice distortions, which leads to a chirality dependence of ω_{RBM}. For large diameter tubes ($d_t > 2\, nm$) the intensity of the RBM feature is weak and is hardly observable.

In 1998, Kataura plotted transition energy E_{ii} as a function of d_t, which is now called Kataura plot (see Fig. 15) and which is widely used for characterization of nanotube. From the Kataura plot, which shows the relation between resonance energy of nanotube and a diameter of nanotube, the chirality of nanotube under resonance condition with incident can be estimated [28-29]. In accordance with Kataura plot, metallic nanotube with 1.4 nm diameter resonate with 1.95 eV (633 nm) light, while semiconducting one with 1.4 nm diameter resonates with 2.54 eV (488 nm) light.

We have two types of resonant scatterings. One is the resonant scattering occurring when the energy of incident light has same energy to inter band transition between E_{11} or E_{22} of matter. Another is the resonant scattering when the energy of scattered light $E_{laser} - E_{phonon}$ equals the inter band transition of matter, which differs by the energy of phonons. That implies that $E_{laser} - E_{phonon1}$ is different from $E_{laser} - E_{phonon2}$, where $E_{phonon1}$ or $E_{phonon2}$ is energy of phonon1 and phonon2. Therefore, one can have only one phonon resonant with incident light in spectrum. Actually, energy difference of phonons between RBM (120-250 cm^{-1}) and G-band (1590 cm^{-1}) is 150 meV, while an energy window for resonant Raman scattering is only 10 meV. Therefore, if you have either a RBM or a G-band in spectrum, it is

highly likely that a resonantly scattered light described by $E_{laser} - E_{phonon} = E_{11}\ or\ E_{22}$ takes place.

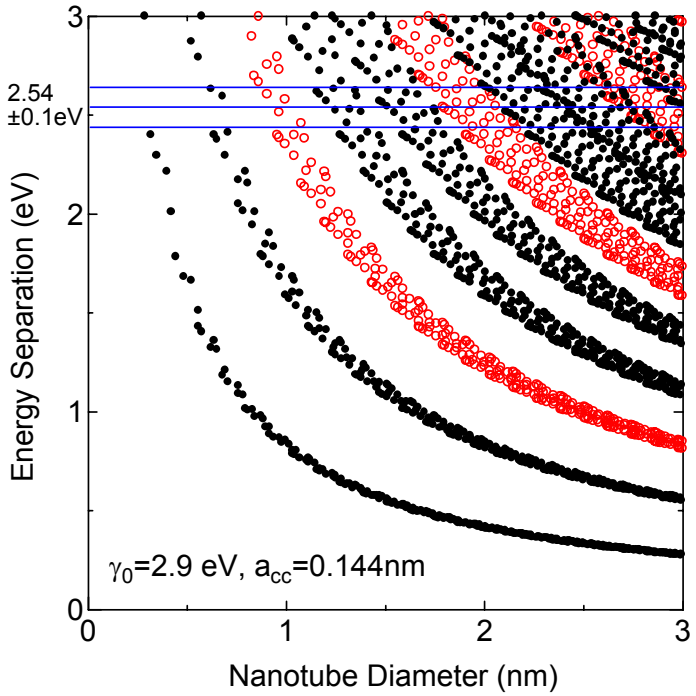

Fig. 15 | Relation between excitation energy and diameter of nanotube under resonance (Kataura plot). Black circles denote semiconducting nanotube and red circles denote metallic nanotube. Blue line shows an energy of 488 nm light [28].

Finally, I show the projection of Raman active displacement patterns of RBM in armchair and zig-zag nanotube. Lowest frequency modes of A_{1g} of armchair and zig-zag are out of plane modes in radiation direction of nanotube, which is the totally symmetric vibration as shown in Fig. 16.

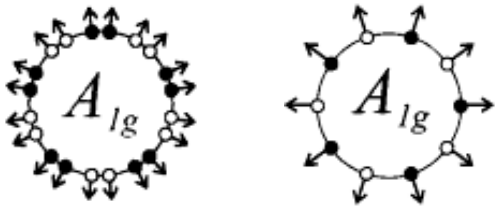

Fig. 16 | Projection of Raman-active displacement of RBM in an armchair nanotube (Left) and an zig-zag nanotubes (Right).

In my research, I used Raman modes of SWCNTs such as G-band, D-band and RBM for characterizing physical properties in SWCNTs. In following sections and chapters, I often refer to the above information for an evaluation of SWCNTs.

Summary

I have introduced the principle of Raman scattering through first section for comprehension of it in a quantitative way. In order to explain the principle, I developed the K-H-D dispersion equation from quantization of radiant field for a thought that Raman scattering happens through a process of annihilation and generation of photons in materials. K-H-D dispersion equation is derived from the simple concept that molecule interacts with photons via electrons. The selection rule of Raman scattering is used for deciding whether Raman scattering takes place or not by irreducible representations of initial, final states of material and an operator of Raman tensor. Then I mentioned about the case of crystal material because I investigated SWCNTs, which is one of crystal, for my research. Finally, I have introduced characteristics of SWCNTs and shown the examples of Raman scattering of SWCNTs, which can be used for characterization of SWCNTs.

References:

[1] C. V. Raman and K. S. Krishnan, Nature **121**, 501-502 (1928).

[2] “Sir C. V. Raman, F.R.S”, Nature **163**, 54-54 (08 January 1949).

[3] S. Iijima, Nature **354**, 56–68 (1991).

[4] 浜口宏夫, 平川暁子, ラマン分光; 日本分光学会 (1988).

[5] H. A. Kramers, W. Heisenberg, Z. Phys, **31**, 681, (1925).

[6] P. A. M. Dirac, Proc. Roy. Soc. (London), **A 114**, 710, (1927).

[7] 浜口宏夫, 田隅三生, ラマン分光の基礎; 南江堂 (1983).

[8] G. Placzek,: “Handbuch der Radiologie” Akademische Verlagsgeselshaft, Leipzig, Vol. **6**, Part. 2, (1934).

[9] 中川一郎: 分光研究 **30**, 223, (1981).

[10] H. Hamaguchi: 文献 B8, Vol. **12**, Chap. 6.

[11] O. Dubay and G. Kresse, Phys. Rev. B., **67**, 035401 (2003).

[12] R. Saito, G. Dresselhaus, M. S. Dresselhaus, Imperial College Press, London, (1998).

[13] M. S. Dresselhaus, G. Dresselhaus, A. Jorio, A. G. Souza Filho, R. Saito, Carbon, **40**, 2043–2061, (2002).

[14] F. Tuinstra, J. L. Koenig, J. Phys. Chem., **53**, 1126, (1970).

[15] M. S. Dresselhaus, P. C. Eklund, Adv. Phys., **49**, 705–814, (2000).

[16] C. Thomsen, S. Reich, Phys. Rev. Lett., **85**, 5214., (2000).

[17] J. Kürti, V. Zólyomi, A. Grüneis, H. Kuzmany, Phys. Rev. B., **65**, 165433(1–9), (2002).

[18] M. Cardona, Topicsin, Applied Physics, vol. **50**, pp.19–176, (Chapter2).

[19] R. Saito, A. Grüneis, Ge. G. Samsonidze, V. W. Brar, G. Dresselhaus, M. S. Dresselhaus, A. Jorio, L. G. Cançado, C.Fantini, M. A. Pimenta, A. G. Souza Filho, New J. Phys., **5**, 157.1–157.15. (2003).

[20] R. Saito, A. Jorio, A. G. Souza Filho, G. Dresselhaus, M. S. Dresselhaus, M. A. Pimenta, Phys. Rev. Lett., **88**, 027401, (2002).

[21] L. G. Cançado, M. A. Pimenta, R. Saito, A. Jorio, L. O. Ladeira, A. Gruneis, A. G. Souza Filho, G. Dresselhaus, and M. S. Dresselhaus, Phys. Rev. B., **66**, 035415 (2002)

[22] A. M. Rao et. al., Science, **275**, 187-191 (1997).

[23] Liu Yang, Phys. Rev. B., **60**, 13874 (1999).

[24] A. Jorio, M. A. Pimenta, A. G. Souza Filho, R. Saito, G. Dresselhaus and M. S. Dresselhaus, New J. Phys., **5**, 157.1–157.15. (2003).

[25] M. Milnera, J. Kurti, M Hulman and H. Kuzmany, Phys. Rev. Lett., **84** 1324, (2000).

[26] A. Jorio et. al., Phys. Rev. Lett., **86** 1118, (2001).

[27] R. Saito, M. Hofmann, G. Dresselhaus, A. Jorio, M.S. Dresselhaus, *Advances in Physics* **60**, 413 (2011).

[28] R. Saito, G. Dresselhaus, M. S. Dresselhaus, Phys. Rev. B., **61**, 2981(2000).

[29] A. Jorio, R. Saito, J. H. Hafner, C. M. Lieber, M. Hunter, T. McClure, G. Dresselhaus and M. S. Dresselhaus, Phys. Rev. Lett., **86**, 1118 (2001).

Chapter 2. Plasmonic enhancement and nano-imaging technique

Low efficiency of Raman scattering has been a problem for all in the field of analytical science. To detect enough signals, a method for enhancing signal has been required. There is one method enhancing Raman signal dramatically, which use metal nano-particles for intensifying signal in the vicinity of them. This is called surface enhanced Raman scattering (SERS) effect [1]. In 1974, Fleischmann, Hendra and McQuillan reported about enhanced Raman scattering from pyridine molecules absorbed on Ag electrode for the first time [2]. The initial paper has been cited more than 3300 times, and the early papers triggered a sustained output of SERS publications, currently numbering more than 8000. However, SERS has drawbacks of spectrum fluctuations and low reproducibility of quantitative measurements. To resolve the problems, SERS is optimized as the technique capable of scanning the nano-metal particle. This is known as tip enhanced scanning technique for imaging nanomaterials. In the first section, I will explain behavior of electromagnetic field near a metal nano-structure under light illumination. Then, in next section, I talk about tip enhanced scanning technique.

2-1. Principle of surface enhanced Raman scattering (SERS)

Surface enhanced Raman scattering from a material can be recognized on the condition that the material is irradiated with light near metal nano-structure through the coupling of electrons in metal with photon. This SERS effect is caused by “Plasmon”. Plasmon is regarded physically as a quantized collective oscillation of electron. This is a physical particle to enhance optical signals, which is a beneficial phenomenon for analytical science because it leads us to nano-world.

In a bulk metal, plasmon doesn’t couple with photon because plasmon is based on longitudinal wave that never couple to transversal wave of photon. However, a situation of surface of metal is different. Plasmon on an interface between a metal and a dielectric medium can couple with photon under a satisfied boundary condition [see Fig. 1].

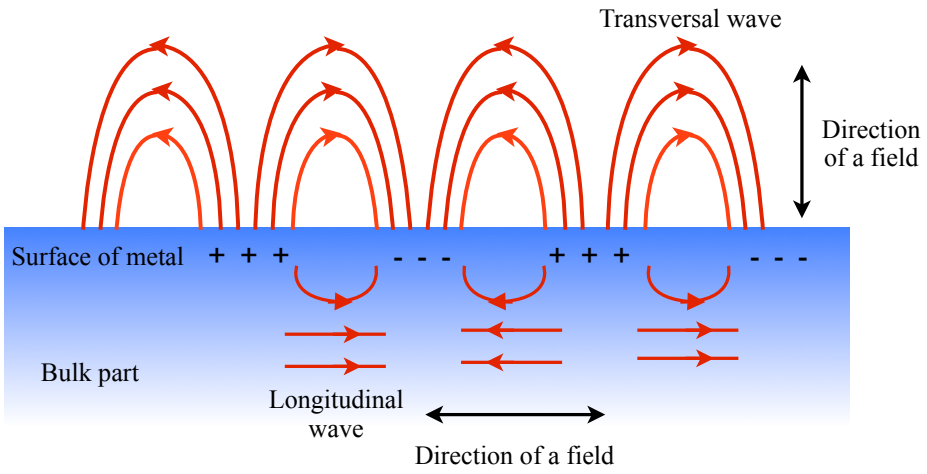

Fig. 1 | Propagating surface plasmon: On the surface of a metal material, we have transversal components which can couple with a wave of light.

Such plasmons coupling with photon on metal surfaces are called surface plasmon polaritons (SPPs), and resonant excitation of SPPs induces field enhancement of light on the metal surface. The SPPs is excited through an effective matching of spatial wavenumbers of surface plasmon (SP) expressed mathematically as follows [3].

$$k_{sp} = \frac{\omega}{c}\left(\frac{\epsilon_1 \epsilon_2}{\epsilon_1 + \epsilon_2}\right)^{\frac{1}{2}} \tag{2.1}$$

where ω is the angular frequency of the SP, ϵ_1 is the complex dielectric constant of the metal, and ϵ_2 is that of the surrounding medium. The absolute value of k_{sp} is greater than that of the propagating light ($k_p = \frac{\omega}{c}$) at any given frequency, as schematically shown in Fig. 2.

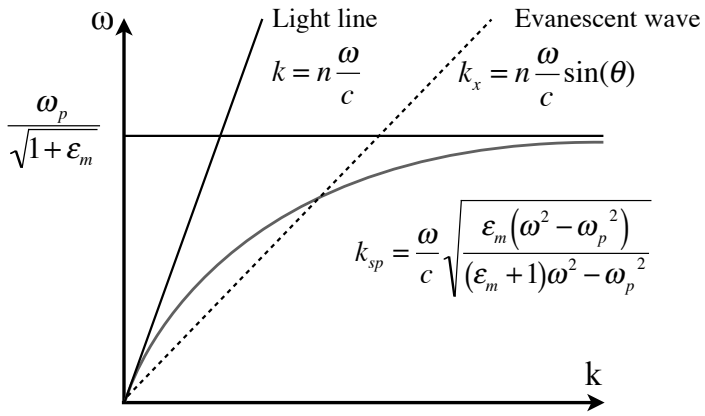

Fig. 2 | The dispersion relation of light in vacuum (Light line) and evanescent light (Evanescent wave) at surface of prism have linear functions. Surface plasmon at boundary of metal/air has non-linear function in Dispersion relation.

Surface plasmon can be induced only by matching wavenumber and frequency of propagating light to those of surface plasmon. For the matching, the wavenumber of propagating light have to increase greater than that of propagating light, which is called evanescent light. Then the energy of evanescent light is converted to the energy of surface plasmon, which is expressed as coupling. Dispersion relationship of light, surface plasmon and evanescent light give a simpler understanding about what is the coupling. The group velocity of SPPs is always slow compared with that of propagating light as shown on Fig. 2, so SPPs are often called “slow light”. Physically speaking, the electromagnetic energy is condensed in the propagating direction. From quantum point of view, slow light can be understood as an increase of the number of photon in a unit value. For the conversion of energy, dispersion curve of propagating light and surface plasmon have to cross together because of matching of wavenumber and frequency of light and surface plasmon. In addition, SPs can be excited using a metal nanoparticle smaller than the wavelength of light. SPP generated by a metallic nanoparticle is called localized surface plasmon (LSP). When light pass easily through a nano-metal structure, an oscillation of electron is formed in a metal nano-particle. That oscillation gives a localized field behaving as a near field light. Unlike propagating SPs on a metal surface, which appear along Eq. (2.1), LSPs on a metallic nano-structure can always couple with an electromagnetic field of propagating light.

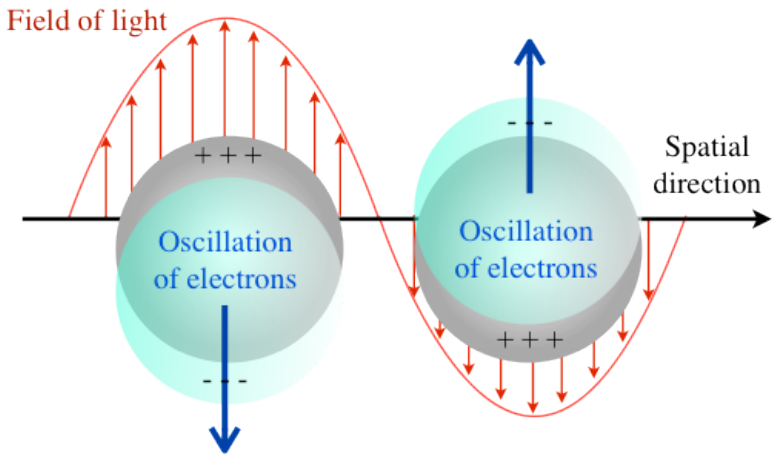

Fig. 3 | The localized plasmon near surface of metal nanoparticle oscillating along a field of light.

Resonance condition of LSPs is derived from resolving Lsplace equation of Mie scattering equation. From the equation of scattered field derived from the Mie scattering equation with quasi-static approximation, which is used only in the case that phase retardation can be neglected, a metal nanoparticle in static field can be regarded as one dipole in the center of the metal nanoparticle under the static field.

$$\vec{p} = \epsilon_2 \alpha \vec{E}$$

$$\alpha = 4\pi a^3 \frac{\varepsilon_1 - \varepsilon_2}{\varepsilon_1 + 2\varepsilon_2}$$

where a denotes the diameter of the nano-particle. From the polarizability denoted as α, the amplitude of the dipole, which is polarizability, drastically increase when the real part of $\varepsilon_1 + 2\varepsilon_2$ equals to 0, which means $\varepsilon_1 = -2\varepsilon_2$. This is localized surface plasmon resonance. In the above condition, the frequency of electronic oscillation is sometimes called Fröhlich frequency. Satisfying the condition, metals such as silver and gold show strong electric-field enhancement in the visible region, because in this region they have small imaginary part of dielectric constant, then absorption by metals becomes low. Silver has plasmon resonance frequency in 340 nm and gold has the one in 490 nm.

An enhancement ratio of the enhanced field to the incident field under the resonance condition can be estimated by the following equation,

$$\eta = \left| \frac{E_{scattered\ field} + E_0}{E_0} \right|^2$$

The maximum value of an enhanced field on the surface of a metallic nano-particle, which is denoted as $E_{scattered\ field}$, is developed by solving scattered field equation under time variable condition.

$$E_{scattered\ field} = 2\frac{\varepsilon_1 - \varepsilon_2}{\varepsilon_1 + 2\varepsilon_2} E_0$$

In that case, the enhancement ratio is expressed as follows,

$$\eta = \left| \frac{2\frac{\varepsilon_1 - \varepsilon_2}{\varepsilon_1 + 2\varepsilon_2} E_0 + E_0}{E_0} \right|^2 = \left| \frac{3\varepsilon_1}{\varepsilon_1 + 2\varepsilon_2} \right|^2$$

In a resonant condition, assuming $\varepsilon_1 = \varepsilon_1' + \varepsilon_1''$,

$$\eta_{max} = 9\left[\left(\frac{\varepsilon_1'}{\varepsilon_1''} \right)^2 + 1 \right]$$

So far, Raman scattering was enhanced typically by a factor of 10^2-10^6. The enhancement factor for the observed Raman signals is resulted from both the enhancement factors for the excitation field and the scattered Raman field, because the field enhancement of a metallic nano-particle act on both fields, which is described as,

$$\eta_{Raman} = \eta_{incident} \cdot \eta_{scattered}$$

The field enhancement effect I mentioned above is used as an intensifier for a weak optical signal such as Raman scattering. One of the methods using this enhancement is SERS technique. However, in SERS technique, Raman signal from a material is enhanced by metalic nano-particles dispersed randomly on substrate. Therefore, it can not be used for quantitative analysis and imaging. For quantitative analysis and imaging, scanning probe technique to

manipulate a nano-particle is needed. Now, tip enhanced Raman scattering (TERS) microscopy takes much attention as a quantitative nano-imaging technique.

2-2. Principle of tip enhanced Raman scattering (TERS) spectroscopy and microscopy

The electronic field enhancement derived from the above sequence of the equations can be used for nanoscopic technique because of the localized feature of LSPs. From 1998, scanning probe microscopic technique using LSPs has been reported frequently as a tip enhancing technique [4-5]. Concept of enhancing optical signal was proposed by Weels in 1985, but couldn't stimulated relevant researches much [6]. Nanosocopy, which enable us to observe and analyze nano-material, can be achieved by replacing a metal nanoparticle with a nano-metal probe, which is called TERS microscopy or apertureless plasmonic near field scanning optical microscopy (p-NSOM). TERS can be categorized as one of SERS technique which controls the position of metallic nano-particle for scanning it over a sample and detecting SERS from the sample. Using this technique, the spatial resolution of the optical image improved much beyond the diffraction limit. The resolution is determined by the radius of a nano-metal probe.

TERS has been utilized for the researches from 2000 by the reports claiming its great capability of imaging nanomaterial [7-8]. Now, TERS spectroscopy and microscopy have became a great tools for sensitive nano-analysis and nano-imaging.

Here I explain about how can we achieve nano-resolution and sensitive analysis by using TERS.

Optical setup and basic performance of TERS microscopy

Our optical setup of TERS microscopy is based on an inverted optical microscope combined with a contact-mode AFM. In Fig. 4, I show the optical configuration of TERS microscopy.

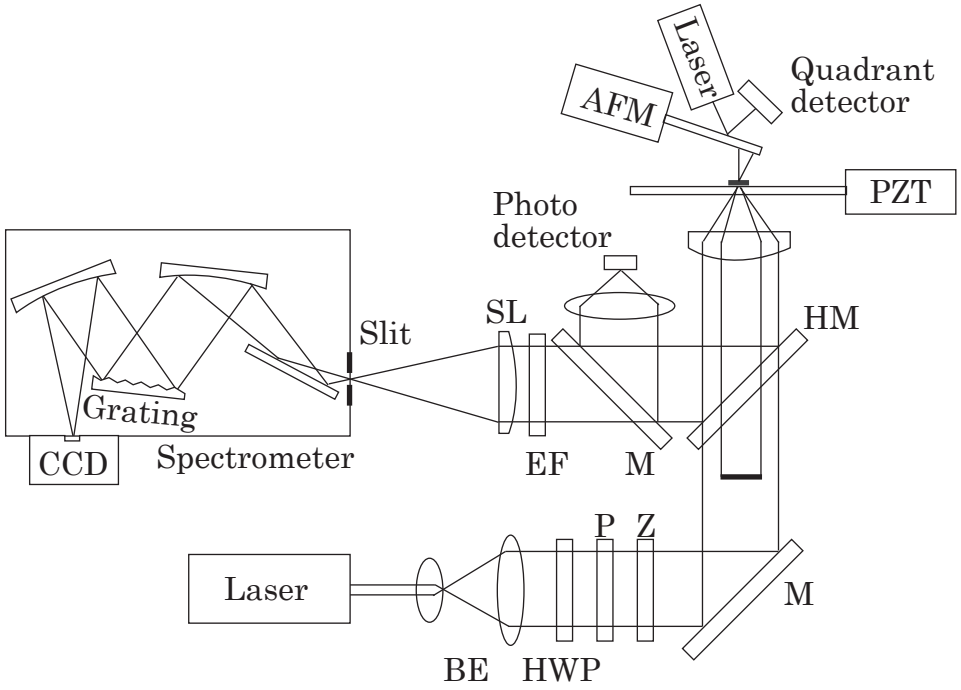

Fig. 4 | The optical setup for tip-enhanced Raman scattering microscope. (BE) Beam expander, which can expand wave surface of light. (HWP) Half wave plate. (P) Polarizer (Z) Z-polarizer. (M) Mirror. (HM) Half mirror without polarization dependence. (EF) Edge filter. (SL) Single lens. (PZT) Piezoelectric element.

Before a light comes into microscope (NIKON: Eclipse TE2000-U), solid state laser (λ: 488 nm) is collimated with a beam expander and is radially polarized with the use of eight divided half wave plates so as to efficiently excite localized surface plasmon polariton along tip apex [9-11]. The laser light pass through a mask for rejecting the low N.A. components, which is less than N.A.=1.0, and is introduced into inverted objective lens (Nikon, Plan Apo.) [12]. By focusing only high N.A. components onto the surface of substrate, the evanescent light occurs. A sillicon cantilever tips used in this measurements were water-oxidized in order to make plasmon resonance shift to shorter wavelength before the cantilever was silver-coated up [13] until the end of a diameter reach 15 nm by the vacuum evaporation method. This tip approaches into the evanescent light and is always adjusted onto the focus spot of evanescent light by controlling precisely the tip position on plane direction of sample stage by feedback system using a quadrant detector. For adjustment of the tip into focus spot, scattering image of tip apex is taken and tip is moved to center of focus spot. The tip with evanescent light works as

plasmon enhanced near field light and display the sample and the enhanced Raman scattering from sample is collected by the same objective lens, then is navigated into spectrometer (Princeton instruments, Inc., SpectraPro -300i). Finally, the enhanced Raman scattering is detected by a liquid nitrogen cooled CCD camera (Rope, 1340×400 channel, -100) incorporated in a spectrometer. Through the navigation process, the Raman scattering is dispersed by a grating, which has blaze wavelength of 1200 lines/mm. The spectrometer gives 1.2 cm^{-1} spectral resolution. This resolution is calculated by following equations.

$$S = d_v S_m$$

where d_v cm^{-1} mm^{-1} is linear dispersion of spectroscope and S_m mm is mechanical slit width. And linear dispersion of spectroscope is determined by v wavenumber in center of spectra and by d_λ wavelength dispersion.

$$d_v = v d_\lambda \cdot 10^{-7}$$

In the case of *Czerny-Turner spectrometer, focal length of spectrometer* f mm and the blaze wavelength of grating N mm^{-1} and an order of diffracted light m need to be considered.

$$d_\lambda = \frac{10^6}{fNm}$$

Our *spectrometer* has $f = 300\,mm$, $N = 1200$ mm^{-1} and $m = 1$. So if 488 nm laser light (20419.8 cm^{-1}) is used, the resolution of spectroscope is,

$$d_v = (20419.8)^2 \cdot \frac{10^6}{300 \cdot 1200 \cdot 1} \cdot 10^{-7} = 115.82$$

Then I always set the slit width as $10\mu m$, which leads to following spectral resolution.

$$S = 115.82 \cdot 0.01 = 1.1582\ cm^{-1}$$

Raman scattering is detected point by point with raster scanning of sample stage.

Tip condition is important for an enhancement of LSPs. Nano particle on tip apex work as intensifier of LSPs so that Raman scattering from sample can be detected by CCDs and the

spatial resolution is determined by size of nanoparticle. Here, I show SEM image of metallic Ag coated AFM tip used for TERS system.

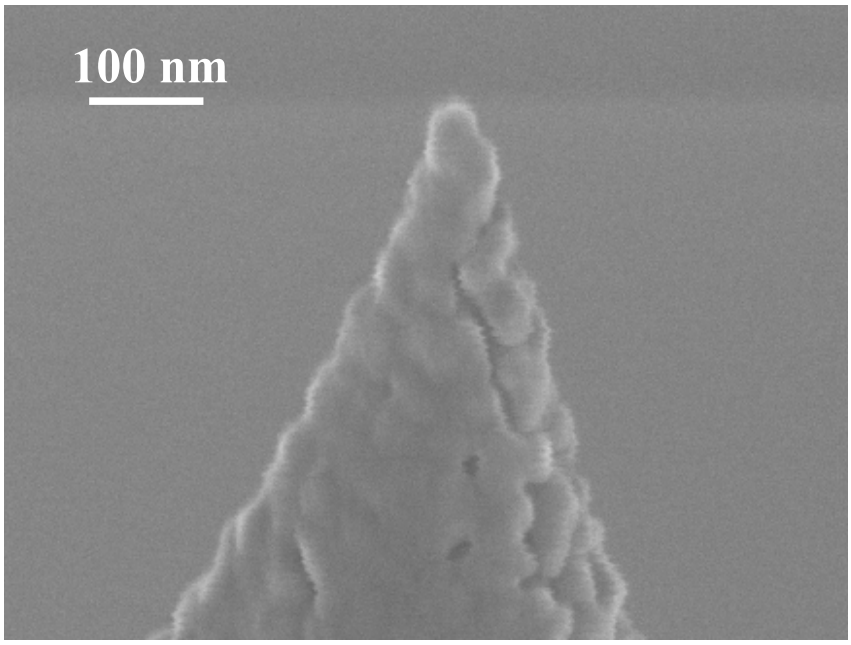

Fig. 5 | SEM image of an apex of a silver coated oxidized Si tip. At very apex, we have silver nano-particle which gives effective enhancement for scattering of material at just below tip.

The curvature of silver nano particles attached on tip apex or apex of metallic tip itself determine the resolution of TERS microscopy [30]. As decrease more the curvature, we have a higher spatial resolution. The size of nanoparticle at tip apex shown in Fig. 5 is around 50 nm. Therefore, less than 50 nm spatial resolution far beyond the diffraction limit of visible light is to be expected. For reference, I show an equation for spatial resolution achieved by using a conventional microscope as follows.

$$x = 0.61 \cdot \frac{\lambda}{NA}$$

where λ is wavelength of incident light and NA is numerical aperture of objective lens used for focusing light. When one use $NA = 1.4$ and $\lambda = 488$ nm, light is confined within around 200 nm.

Sometimes tip can be degenerated by the strong force applied to the tip apex. To avoid this kind of degeneration, tip applied force should be set to 0.1nN and low intensity of incident laser, which is less than $500\mu W$/diffraction limit, is needed [see Fig.6].

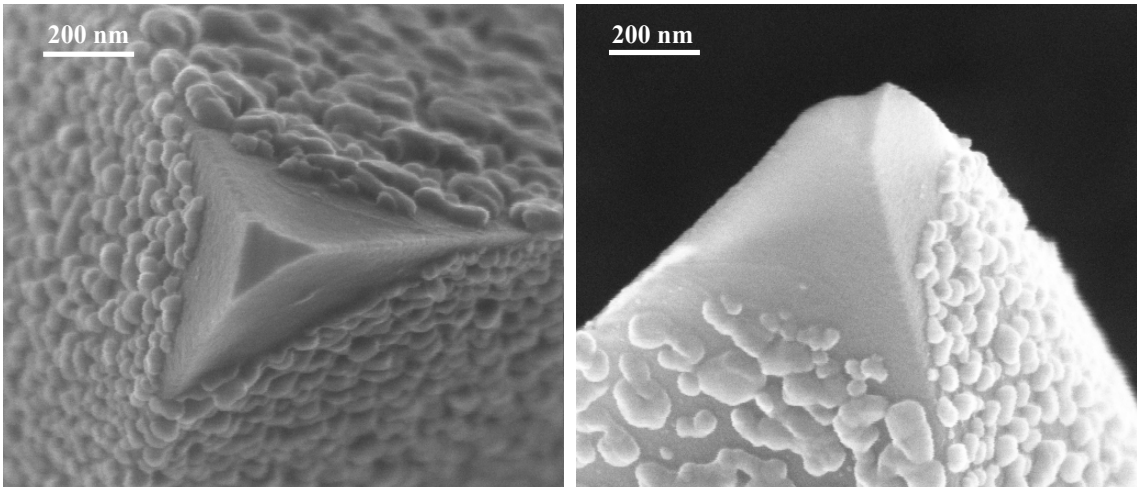

Fig. 6 | SEM image of an apex of a damaged silver coated oxidized Si tip (Left). At very apex, we see silver nano-particle being peeled off from apex of tip (Right).

Tip position adjustment

For an effective coupling of localized surface plasmon with light, tip position relative to focus spot is significant. An objective lens with high N.A. is useful to induce the strong z-polarized fields and tip apex has to be on the position where there are the strong z-polarized fields. I show the optical system used for tip positioning in Fig. 7 (a). For a rough positioning of the tip relative to focus spot, an image of tip shone by white light is taken by CCD camera as shown on Fig. 7 (b). Then the tip is moved to the position of focus spot. For a more precise adjustment, tip scans over a focus spot and scattered signals from tip apex, which are detected by a photo detector, are used for constructing the scattering image as shown on Fig. 7 (c). Yellow spot in Fig. 7 (c) indicates the position showing strong interaction between the focus spot and metallic tip, where we have a strong sufficient excitation of localized surface plasmon. Relative position of tip to focus spot can be monitored by CCD image incorporated in microscope. Fig. 8 (a) and (b) show the image of focus spot and tip apex both taken by the same CCD camera. The place of focus spot and the tip position are confirmed by the images. By monitoring these CCD images and scattering image taken by photo detector, which is shown in Fig. 7 (c), I easily bring the tip apex to the focus spot to induce localized surface plasmon at tip apex.

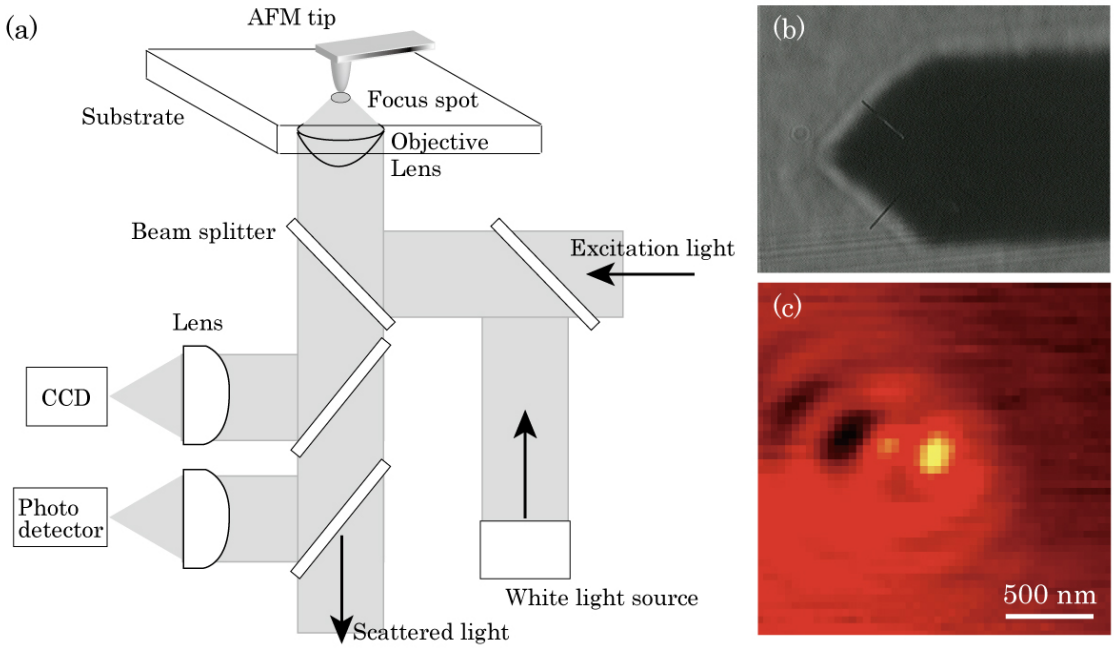

Fig. 7 | (a) Schematic image for tip positioning (b) CCD image of tip (c) Field distribution of focus spot constructed by scattering light interacted with metallic tip.

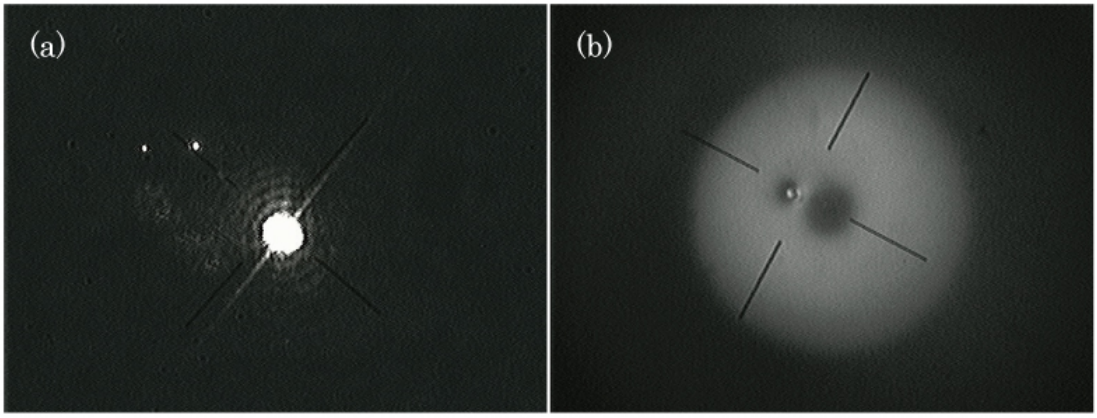

Fig. 8 | CCD images of (a) focus spot and of (b) a tip apex shone by white light from bottom side.

Polarization tendency for enhancement

Electrons at metallic tip apex resonantly oscillate when they perceive electric field oscillating parallel to the tip axis due to lightning rod effect [14, 29]. Therefore, polarization property of an incident light is important and the polarization should be set to have as much z-vertical components as possible onto a surface of substrate because tip has a sharp structure in z-coordinate [see Fig. 9].

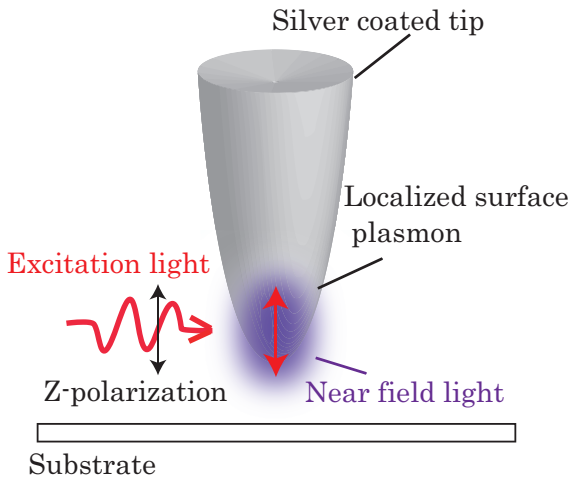

Fig. 9 | Plasmonic enhanced near-field induced at silver tip apex by z-polarized light. Polarized light whose polarization lie in axis of tip comes into tip apex, which results in exciting strong z-polarized near field at the apex.

In conventional microscopic technique, a focusing of ordinary laser beam such as linear polarized laser beam doesn't provide a polarization component along tip axis at the center of focus spot because polarized light coming with angle to substrate are cancelled out at the center. Then we have two strong z-components at the position deviated from the center as shown on Fig. 10 (a). Therefore, tip has to be placed on one of spots induced near off from the center position of focus spot where strong z-components appear, which gives low z-components even on effectively interacted positions. To resolve these problems, radial polarizer can be employed for making radial polarization of light having z-components at the center when it is focused on sample plane with the use of objective lens. Inserting π phase plate to one half of beam resolve the problem that z-components are canceled out and z-polarized light constructively interfere at the center of the focus spot, which provide one strong z-components at the center as shown on Fig. 10 (b).

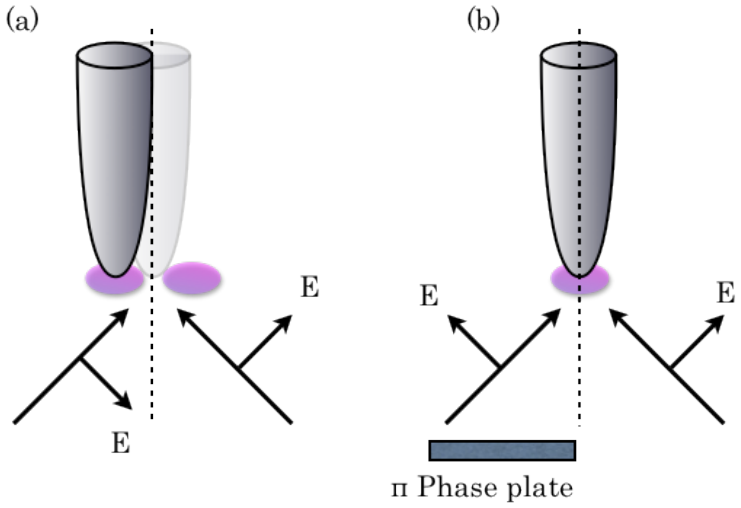

Fig. 10 | Two types of configuration of laser focusing (a) linear polarized laser light, which results to have two strong z-components off-center (b) z-polarized laser light, which results to have one strong z-components at center.

I show a scattering image of focus spot in Fig. 11 when z-polarized light is focused onto the substrate with high N.A. objective lens after passing through mask to remove low N.A. components. Fig. 11 implies that the focus spot has strong z-components at the center, which means that a metallic tip can interact effectively with light at center.

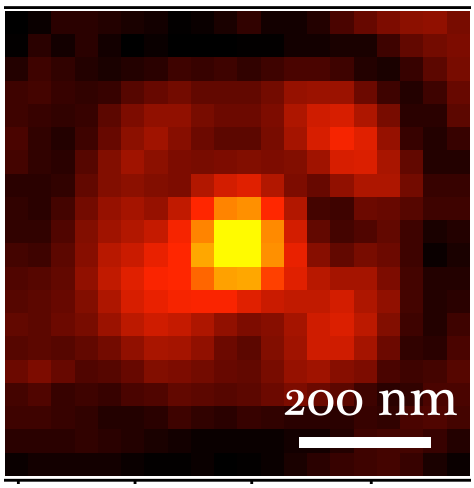

Fig. 11 | Field distribution of focus spot with the use of z-polarized laser light, which results to have one strong z-components at center.

Optimization of geometry and material of metallic tip

Geometry and material of metallic tip are quite important to induce strong enhancement of electronic field of plasmon on tip apex. Au or Ag has been utilized for TERS tips because of plasmonic resonance located in visible region. And metallic smooth surface or rough surface of tip apex are tried to be evaluated for inducing strong electronic field of plasmon and base materials such as SiO_2, AlF_3, SiOx, Si_3N_4 and W have been selected for changing resonance wavelength of plasmon by changing refractive index near plasmonic tip. This is because TERS performance has been theoretically predicted to improve by using an AFM tip with a low permittivity [13, 15-18]. The plasmonic resonance wavelength is greatly altered according to a refractive index of materials. For example, since a refractive index of Si and SiO2 is ～4.3 and ～1.5 at the wavelength of 488 nm, the plasmon resonance wavelength of a Ag-coated silicon tip is dramatically blue shifted with a replacement from Si to SiO_2. Numerical analysis is conducted to estimate the plasmon resonance shift, magnitude and field distribution for TERS by altering base materials of nano-shell structure or sample thickness [19-21]. In addition, coating treatment on a metallic tip surface has came under the spotlight for improving a stability of plasmonic metal tip. One report claimed that metallic tip gives constant enhancement for over 40 days by pre-coated with ultra thin aluminum oxide [22]. And Zenobi et. al. have demonstrated theoretically that a SiOx layer can protect metallized tips for TERS too [23].

These kinds of works provide a new method to prevent metallic tips from undesired physical and chemical damages without losing their original performance for TERS.

Reports on a size effect of nanoparticle and an aspect ratio of ellipsoid structure on the frequency of plasmon are important for TERS. The report by Luis M. Liz-Marza´n showed that an increase in diameter from 10 up to 100 nm leads to red-shift of 47 nm for spherical particles, whereas a change in aspect ratio from 2.5 up to 3.5 for prolate ellipsoids promotes red-shift of the longitudinal plasmon band of 92 nm, which is almost double the size effect [24]. Therefore, it can be said that the change of an aspect ratio of tip is more crucial for resonance shift of localized surface plasmon. This implies that cone angle of metallic tip have to be taken account of for deciding wavelength of laser light. And also a finite tip gives higher enhancement for apertureless NSOM probe and the length of finite tip is important factor for an optimum enhancement, which revealed that partial peeling off technique could have effect on TERS optimization [25].

The tip geometry for enhancement is still under discussion because of difficulty in elucidating the relation between tip apex structure and how the signals are enhanced [26-27].

Summary

I have introduced the principle of SERS, which gives us comprehension of plasmonic field enhancement in the close vicinity of metal nanostructures and behavior of electromagnetic field near a metal nano-structure under light illumination. Then I have explained about how SERS got involved in nano-analysis and nano-imaging, one of which has been now utilized as TERS technique. Then I explained about the principle of TERS. Through this TERS section, I described the property of localized suface plasmon and effective enhancement of local field of plasmon at the tip apex. Optical setup of TERS spectroscopy/microscopy was described with simple scheme and I mentioned what keys are in this technique. Finally, I showed effective inducing and collection of Raman signal. And I push the importance of polarizability on metal tip and the tip geometry.

References:

[1] R. P. Van Duyne, Chem. Biochem. Appl. Lasers., **4**, 101–185 (1979).

[2] M. Fleischmann, P. J. Hendra and A. J. McQuillan, Chem. Phys. Lett., **26**, 163–166 (1974).

[3] 岡本隆之, 梶川浩太郎, プラズモニクス; 基礎と応用, 講談社

[4] L. Novotny, E. J. S´anchez, & X. S. Xie, Ultramicroscopy, **71**, 21–29, (1998).

[5] E. J. S´anchez, L. Novotny, & X. S. Xie, Phys. Rev. Lett., **82**, 4014–4017, (1999).

[6] J. Wessel, J. Opt. Soc. Am., **B 2**, 1538–1540, (1985).

[7] S. M. Stockle, Y. D. Suh, V. Deckert, & R. Zenobi, Chem. Phys. Lett., **318**, 131–136, (2000).

[8] N. Hayazawa, Y. Inouye, Z. Sekkat, & S. Kawata, *Optics Communications,* Vol. **183**, No. 1-4, pp. 333-336, (2000).

[9] Y. Saito et. al., J. Raman. Spectrosc., **39**, 1643-1648, (2008).

[10] N. Hayazawa, Y. Saito, & S. Kawata, Appl. Phys. Lett., **85**, 6239-6241, (2004).

[11] N. Anderson, A. Bouhelier, & L. Novotony, J. Opt. A: Pure Appl. Opt., **8**, S227-S233, (2006).

[12] N. Hayazawa et. al., J. Microsc., **194**, 472-476, (1999).

[13] A. Taguchi et. al., Opt. Express., **17**, 6509-6518, (2009).

[14] L. Novotony, R. X. Bian, & X. S. Xie, Phys. Rev. Lett., **79**, 645-648, (1997).

[15] C. C. Neacsu, G. A. Steudle, & M. B. Raschke, Appl. Phys. B., **80**, 295-300, (2005).

[16] D. Mehtani et al., J. Opt. A., **8**, S183-S190, (2006).

[17] B. Yeo et. al., Anal. Bioanal. Chem., **387**, 2655-2662, (2007).

[18] X. Cui et. al., Opt. Express, **15**, 8309-8316, (2007)

[19] I. Notinger, & A. Eflick, J. Phys. Chem. B., **109**, 15699-15706, (2005).

[20] F. Fresty et. al., Ultramicroscopy, **100**, 437-441, (2004).

[21] C. Graf and A. v. Blaaderen (2002). *Langmuir* **18,** 524–534.

[22] C. A. Barrios et. al., J. Phys. Chem. C., **113**, 8158-8161, (2009).

[23] X. Cui, D. Erni, W. R. Zhang, R. Zenobi, Chem. Phys. Lett**., 453***,* 262, (2008)

[24] Luis M. Liz-Marza´n, Langmuir*,* **22***,* 32-41, (2006)

[25] J. T. Krug II et. al., J. Chem. Phys., **116**, 10895-10901, (2002)

[26] Y. Saito et. al., Chem. Lett., **34**, 920-921, (2005).

[27] Y. Zou et. al., Appl. Phys. Lett., **94**, 171107, (2009).

[28] M. Fleischer et. al., Nano. Lett., **5**, 2570-2579, (2011).

[29] A. V. Ermushev , B. V. Mchedlishvili, V. A. OleTnikov, and A. V. Petukhov, Quantum Electron. 23 (5), 435, (1993)

[30] F. Fresty et. al., Ultramicroscopy, **100**, 437-441, (2004).

Chapter 3. Manipulation of SWCNTs

This chapter represents effects of manipulations on properties of SWCNTs. I present the strains and defects distribution induced by atomic force microscope (AFM) tip manipulation and how it affects on the properties of SWCNTs by conventional Raman spectroscopic/microscopic investigation as well as tip-enhanced Raman investigation for nano analysis and nano-imaging. This chapter is divided into 4 sections. Each section is about strain generation on a SWCNT caused by manipulation, quantum chemical calculation of strain effects on Raman spectra, Raman investigation of manipulated SWCNTs and tip enhanced Raman investigation of manipulated SWCNTs.

3-1. Manipulation of SWCNTs and strain generation in SWCNTs

SWCNTs are promising candidates for novel nano-electronic devices because of their unique mechanical and electronic property [1-6]. Making well organized nano-electronic devices requires precise and desired positioning of SWCNTs using precisely controlled AFM tip, which is often called a manipulation. Any manipulation of SWCNTs may induce highly localized variation in their physical properties, such as electronic property, mechanical property and heat conductivity caused by localized defects or strains along their lengths. However, still how the localized defects and strains affect on their electronic property and other physical properties has been unclear, which has made many researchers be interested in properties changing depending on strains and defects induced by deformations [7-14]. Raman spectroscopic and microscopic investigations are used for this property change by analyzing Raman signature precisely.

In order to explain my AFM-based manipulation technique utilized for manipulating SWCNTs, Fig. 1 (a) illustrates manipulation steps where a nanotube is being dragged through a series of lateral pushes by the AFM tip apex, and Fig. 1 (b) shows the scanning scheme of an AFM tip during topographic imaging of manipulated SWCNT. After several precisely controlled manipulation steps, which are shown in Fig. 2 (a) and (b), the isolated SWCNTs could be manipulated to any desired shape as shown on the AFM image of manipulated SWCNTs in Fig. 3. Through the sequence of manipulations, the AFM tip operating under the contact mode configuration was positioned near a specific site of the nanotube and was scanned towards the nanotube along a straight line by maintaining the tip-applied vertical force constant at 20 nN,

which dragged the nanotube locally in the direction of tip scanning and was deformed into the "C" shape as shown on Figure.2 (b).

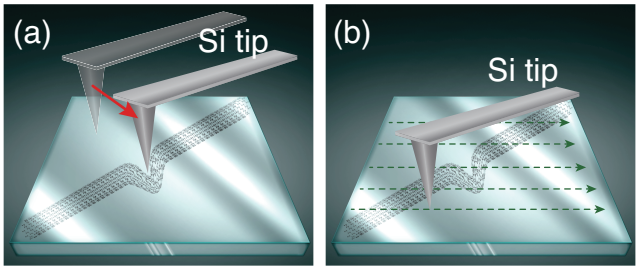

Fig. 1 | Manipulation of CNTs by an AFM tip. (a) An illustration showing the manipulation scheme where a straight isolated CNT lying on a glass substrate is locally dragged by the sharp apex of an AFM tip, as the tip scans along a straight line in a contact- mode operation with a constant tip-applied force of 20 nN. (b) An illustration showing AFM imaging of a manipulated CNT. The imaging is performed in tapping-mode operation, where there is no more manipulation of the CNT during the imaging process.

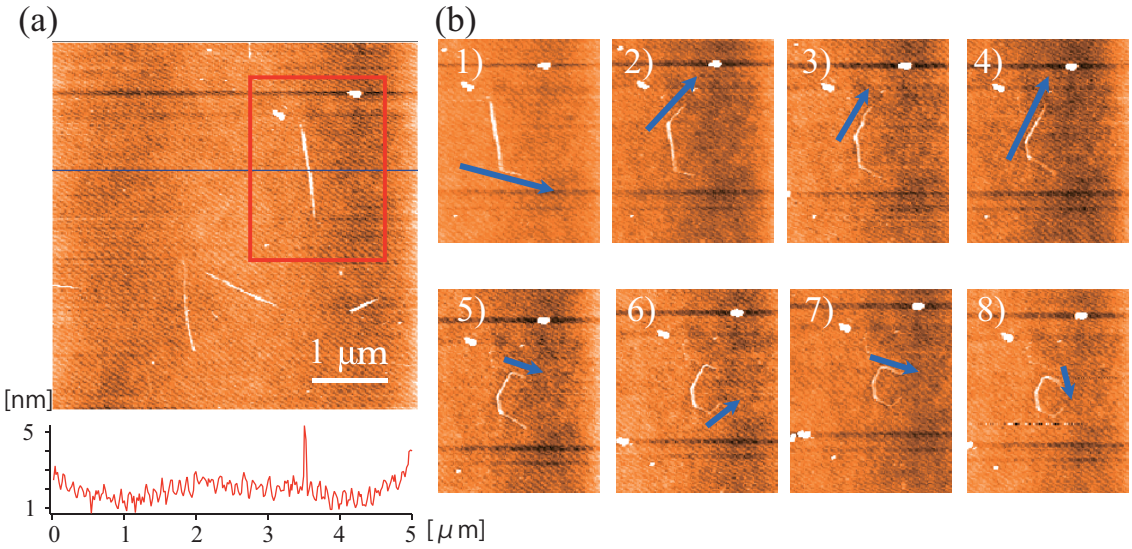

Fig. 2 | Manipulation process of CNTs by an AFM tip (a) AFM image of target area and target sample colored by red square. And line profile along blue line on (a) is shown on bottom of this image (b) Manipulation process for making "C" alphabet is shown in order of steps from 1 to 8 steps.

The examples in Fig. 3, which are AFM images of manipulated nanotube deformed to “A”, “B”, “C”, “P”, “Q” and “R” alphabets, show that my AFM-based dragging technique works well for manipulating SWCNTs to any desired shape and dragging them to any required location.

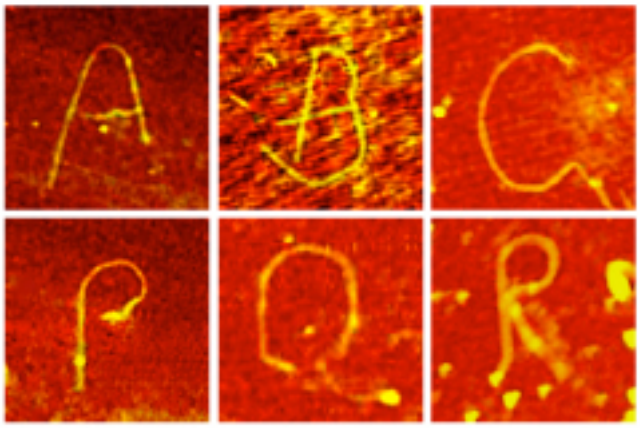

Fig. 3 | Some examples of manipulated CNTs, where the CNTs take the shapes of alphabets.

Raman measurement is still strong to study many physical phenomena occurring in a SWCNT, although there are even only limited parameters in a Raman spectrum, namely, the intensity, the frequency positions and the peak broadening. Variations in these parameters can be related to different kind of physical phenomena. Through the manipulation process, rolling, moving and stretching are developed up on SWCNTs as strains, which could be thought to be a direct factor on the change of electronic property of SWCNTs. What we need to disclose from this manipulated SWCNTs is what types of strains could be applied to SWCNTs through manipulation. The shift, intensity and splitting of particular modes in Raman spectra can help to evaluate this strains.

From now, I present what G-band shift in Raman spectra stands for and how it relates to types of strains, which can be achieved by just dragging with the AFM based manipulation system.

The strains in SWCNTs are developed by displacements of carbon atoms, which are caused by the friction between the substrate and the SWCNTs. By manipulating straight shape SWCNTs into a desired shape, the nanotubes locally roll on the substrate, inducing a local torsional strain, and a part of it is elongated on the substrate to induce local tensile strain. These local strains remain in the SWCNT permanently if it stably sticks onto substrate after the manipulation. Fig.

4 can explain the physical condition of SWCNT during local rolling and elongation, which induce torsional and tensile strains, respectively.

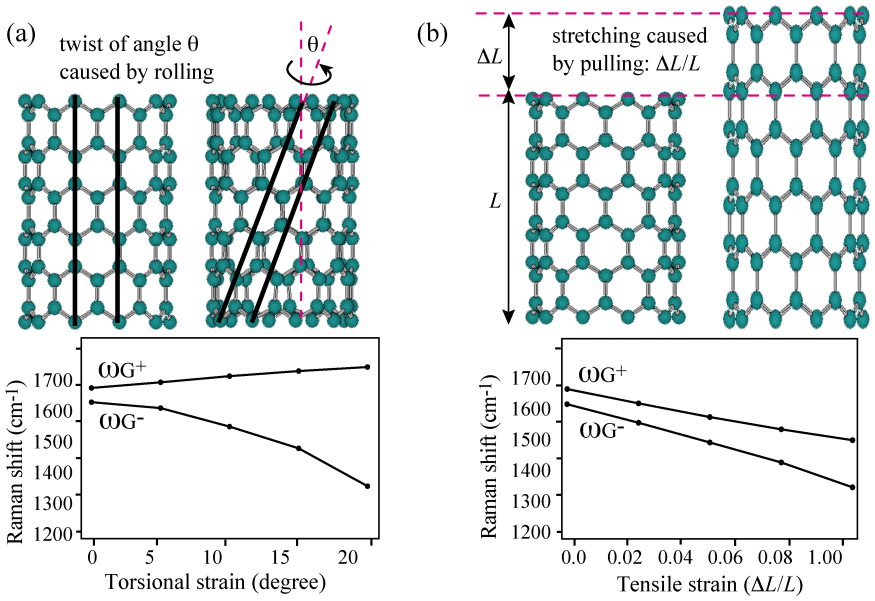

Fig. 4 | Illustration of strain in SWCNT developed by (a) twist and (b) stretching. The lower curves show calculated shifts in G-mode (both G+ and G- modes). The G+ mode shifts in higher-frequency direction for torsional strain, while it shifts in the lower frequency direction for tensile strain.

As illustrated in Fig. 4(a), the SWCNT is locally twisted with some angle of twist, θ, which can be used to quantify the amount of torsional strain on the SWCNT. The lower curves in Fig. 4(a) show the calculated shifts in G-modes as a function of θ. Similarly, Fig. 4(b) shows an illustration of tensile strain in SWCNT, developed by stretching of SWCNT in tangential direction by a length ΔL. Here, the relative increase in length, ΔL/L, can be used to quantify the amount of tensile strain. The lower curves in Fig. 4(b) show the calculated shifts in G-modes as a function of ΔL/L. The calculations are performed for a SWCNT possessing (10, 0) chirality. A similar result is expected for other chirality, as well.

For the calculation, I used Density Functional Theory (DFT) method by using Gaussian software, which is a computer program for quantum chemical calculation built by John Pople [27-28]. The concept of this calculation is that the Hamiltonian operator and the energy of a certain system is derived only from the value of electron density $\rho(r)$. In DFT method, electronic energy is calculated by solving Kohn Sham equation.

$$\left(-\frac{1}{2}\nabla^2 - \sum_{A=1}^{M}\frac{Z_A}{r_A} + \int\frac{\rho(r')}{|r-r'|}dr + V_{XC}(r)\right)\psi_i(r) = E_i\psi_i(r)$$

where first term is an operator for a motion energy and second term is an operator for a motion for inter electron-core attracting force and third term is an operator for Coulomb repulsive force and forth term is a exchange correlation functional operator. $\psi_i(r)$ is i-state Kohn–Sham wavefunction in multielectron system. And from Kohn-Sham orbit, electron density $\rho(r)$ is calculated as shown in following equation.

$$\rho(r) = \sum_{i}^{n}\psi_i(r) * \psi_i(r)$$

Electronic energy E_i can be simply described as following equation.

$$E_i = E^T + E^V + E^J + E^{XC}$$

where E^T is a term for a motion energy and E^V is a term for potential energy of internuclear repulsive force and inter electron-core attracting force and E^J is a term for repulsive force between electrons and E^{XC} is a term for exchange correlation and electron correlation. Proper solution for the exchange and correlation energy expressed as E^{XC} is still under controversial. Following exchange and correlation energy is often used, which is known as B3LYP type functional.

$$E_{B3LYP}^{XC} = E_{LDA}^{X} + c_0(E_{HF}^{X} - E_{LDA}^{X}) + c_X E_{B88}^{X} + E_{VWN3}^{C} + c_C\left(E_{LYP}^{C} - E_{VWN3}^{C}\right)$$

where each parameters are $c_0 = 0.20$, $c_X = 0.72$ and $c_C = 0.81$. Explanation of LDA, B88, VWN3 and LYP is beyond the scope of this chapter. To calculate Raman scattering intensity, following equation is used.

$$I_{Raman} = \left(\frac{\partial \alpha_{\rho\sigma}}{\partial Q_a}\right)_0 \int \Psi_{i+1} Q_a \Psi_i dx$$

where is $\left(\frac{\partial \alpha_{\rho\sigma}}{\partial Q_a}\right)_0$ derivative of polarizability tensor $\alpha_{\rho\sigma}$ at Q_a, which is base coordinates, and Ψ_{i+1} and Ψ_i are final-state and initial-state wave function in multielectron system composed of linear combination of Kohn Sham orbits.

For a calculation of normal vibrational modes, a hybrid functional of $B3LYP$ and a base function of $6-31G(d)$ are used. First step for the calculation, a structure of the nanotube is optimized by $B3LYP/6-31G(d)$ and normal vibrational frequency is calculated in the calculation level of $B3LYP/6-31G(d)$ with the use of the optimized structure. When a potential energy of whole system you modeled takes minimum value through the calculation, DFT calculation converges. For modeling a structure of carbon nanotube, I used WINMOSTAR and GAUSSVIEW, both which are computer software works on Windows and Linux.

One can notice that the direction of shift for the G+ mode in Figs. 4(a) and (b) are opposite, which can be utilized to understand whether the developed strain is torsional or tensile. One has qualitatively estimated the amount as well as the nature of strain within the CNT by measuring the value as well as the direction of shift in the frequency position of the G+ mode [8]. That means the shift in G+ mode can be in both positive and negative directions, depending upon whether the tensile or the torsional strain is dominant. Thus, we can also estimate the nature of dominant strain from the shift in G-mode.

3-2. Raman spectra analysis of G+ mode of manipulated SWCNTs

I present here a Raman investigation of strain distribution on manipulated SWCNTs and process of growing strains up by manipulation. Finally, I show a mixing of a tensile and a torsional strain made up by simple dragging.

In my experiment, semiconducting SWCNTs used for Raman microscopic measurements were produced by Meijo carbon Inc., with a purity of ~99%. Individual bundle of this semiconducting SWCNTs with the diameter equal to 1.4 nm were ultrasonically dispersed with 1-2 dichrolethane, then the droplets of this solution were spin-casted onto the glass coverslip. The probable rolling indexes, which are often called chirality, of SWCNTs used for my study

are (12, 11), (15, 7) (16, 5) base2d on Kataura plot and the peak value of Raman frequency in radial breathing mode [15]. My experimental setup, based on an inverted optical microscope combined with a tapping-mode AFM capable of manipulating sample on the substrate, was especially established for Raman microscopy to analyze strained SWCNTs. Raman scattering from the sample were excited by solid state laser (λ: 488 nm, Nippon roper, Inc., Sapphire LP). The Raman scattering was detected by CCD (Princeton instruments, Inc., LNCCD, 1340/400. *EB/1*) incorporated into a Raman spectrometer (Acton, Inc., Spectrapro 300-i, focal length is 300 mm), which provide 1.2 cm^{-1} spectral resolution with 10 μm slit with in front of spectrometer.

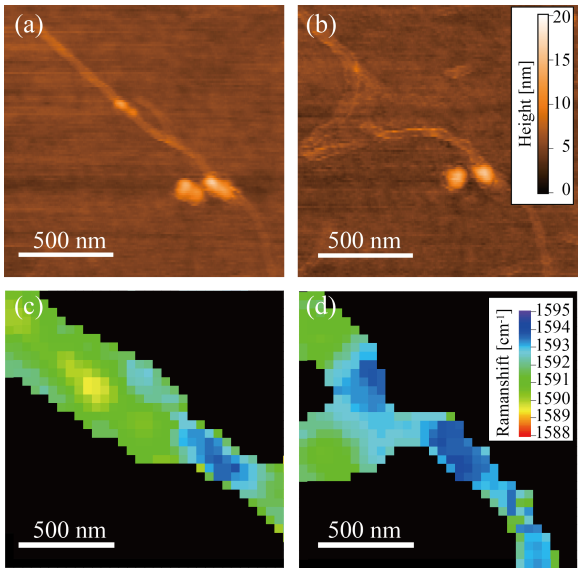

Fig. 5 | AFM images of SWCNTs sample (a) before and (b) after manipulation. Raman images of the sample (c) before and (d) after manipulation, which are constructed from the peak shift of G+-mode.

SWCNTs lied on substrate, whose shape is straight, were used as a target sample for Raman microscopic measurements, which is shown in Fig.5 (a) as an AFM image. The diameter of the bundle of SWCNTs was estimated around 2.5 nm by the line profile of the AFM image in Fig.5 (a), which is the evidence that this sample consists of 2-3 SWCNTs. AFM based manipulation system was utilized to form arbitrarily a shape on SWCNTs, in this time I made “V” shape, as shown in Fig.5 (b) as topographic image of the manipulated SWCNTs, by dragging them from its side. The shape in Fig. 5(b) was so stable that SWCNTs could keep deformed shapes under the strains developed by dragging (manipulation) owing to strong adhesion on the glass substrate. For evaluating types of strains developed through forming “V” shape, a comparison

of Raman image of the SWCNTs before and after dragging, which were constructed from the peak shift of Raman G+ mode, was shown on Fig.5 (c) and (d), respectively. In this time, a polarization of the light was a circular polarization.

In general, Raman imaging, which includes Raman spectroscopy, is the best way to visualize and analyze these strains [12] and Raman scattering can even distinguish between torsional and tensile strains in SWCNTs, because the high-frequency G-band vibrational mode (G+-mode) shifts towards higher frequency under a torsional strain, while it shifts towards lower frequency under a tensile strain as I said previous section [9]. In Fig. 5 (c) and (d), stretching and torsional strain each denoted as red color and blue color, which was induced by manipulation from the side at the center of SWCNTs with the AFM tip.

From the existence of higher frequency shift of G+ mode, colored by blue in Fig. 5 (d), torsional effect took over at two points of supports where smooth curves emerge after manipulation. Interestingly, a strong curved part, which is colored by green and is most dragged to form kink shape, didn't show any Raman shift. This result could be the evidence of a mixing effect of stretching and torsional strain. From these results, manipulating nanotube from an inner location could provide a possibility of SWCNTs being got a torsional train except for kink part (pushed region).

As a next step, for observing how strains are developed during a dragging (manipulation) process, a spectra evolution analysis as a function of step numbers of manipulation was conducted. During manipulating SWCNTs, laser focus was fixed onto the position of tip apex and tip moved with focus spot. Steps of dragging are 50 steps. At each steps, Raman scattering spectra from focus spot on the tip apex were detected, as shown in Fig. 6(c). And SWCNTs are dragged from inner part by tip. From the previous results shown in Fig. 5, one can expect that G+ mode cold be getting higher shift as manipulation proceeds. However, as a result shown in Fig. 6 (a), which shows spectra change in G-band region through the sequence of step numbers, I noticed the discreet change in G+ mode as a jump to lower frequency just when the tip started to touch SWCNTs, which implies the evidence of being incurred by stretching effect as easily seen in Fig. 6 (b). However, more manipulation steps proceeds, G+ mode gradually recovered back to the original position around 1590 cm^{-1}. This result indicates that the more deformation proceeds, the more complicated strains applied to SWCNTs become enough to cancel stretching

effect by torsional or just by symmetry breaking. For the easier look, the comparison of spectra of SWCNTs before manipulation and the end of manipulation are shown on Fig.6 (d).

At the beginning of manipulation, stretching strain, which was confirmed as a lower frequency shift of G+-mode as you can confirm by red spectra shifting to blue spectra in Fig.6 (d), was found to be dominant in strains applied to SWCNTs. However, as taking more steps, the dominance of stretching strain became weaker, confirmed by G+ mode recovering back to the original position, as shown on green colored spectra in Fig.6 (d), from which I concluded that there was relaxation of strains or mixing effect of torsional with stretching strain on SWCNTs.

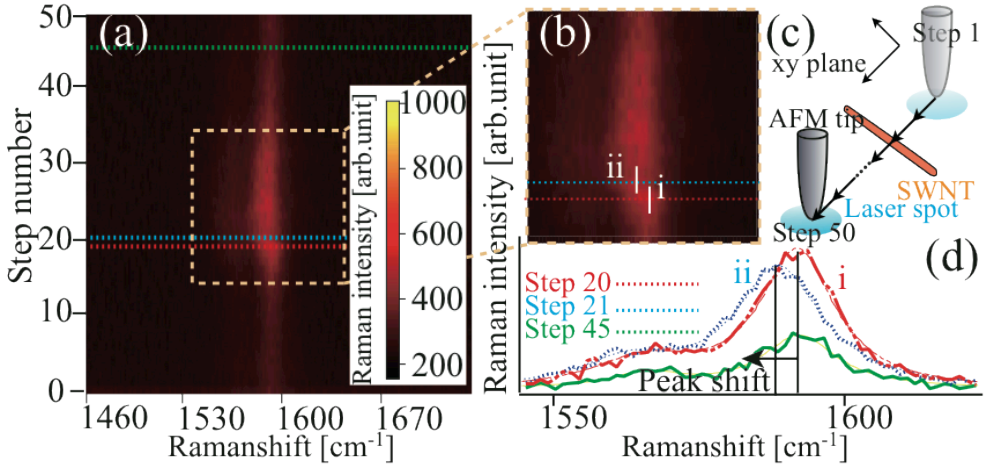

Fig. 6 | (a) Raman evolution image during manipulation. Raman intensity is denoted as black-yellow color. (b) A magnified image in yellow dotted region in (a) and white lines denoted as (i) and (ii) show the peak positions of G+ mode. (c) The schematic image of spectra evolution analysis. Tip moves from top right to bottom left along arrow through manipulation process over nanotubes colored by yellow. (d) The Raman spectra taken from red, blue and yellow dotted lines in Fig.2 (a).

Let me start my discussion by taking the results obtained through far field Raman studies into consideration for explaining what came to happen on the SWCNTs after the manipulation. Manipulating SWCNTs gave rise to complicated strains on their structure, which was confirmed by the Raman peak shift in G+ mode. Then from a time-lapse measurement of Raman evolution during manipulating, I concluded that tensile strain was dominantly applied to SWCNTs at the beginning of manipulating while torsional strain sets off the effect of the tensile in the end.

More simply speaking, from results shown in Fig. 5 and Fig. 6, it seems that a degree of manipulation decides the main strains applied to SWCNTs and a slight manipulation from inner position of SWCNTs gives a stretching effect, whereas an excessive manipulation gives a torsional effect.

3-3. Defect evaluation in manipulated SWCNTs by D/G ratio analysis

I present here a Raman investigation of defects distribution on manipulated SWCNTs, process of growing defects developed by manipulating and finally we show a tangible interplay between torsional strain and defect.

Change of lattice distance between C-C atoms is possibly considered to be a main factor for an increment of D-band intensity. For an investigation of how the pure defects are induced upon SWCNTs, I imaged manipulated SWCNTs, which was in the white dotted rectangular region in AFM image shown in Fig. 7 (a), with the ratio of D-band intensity divided by G-band intensity as shown in Fig. 7 (b). From the image of Fig. 7 (b), I noticed that defects were mainly induced at highly bended part in SWCNTs, which can be seen as a bright white color in this image. This result seems to be conceivable and reasonable because lattice distance change at bend region should be larger than that at straight part.

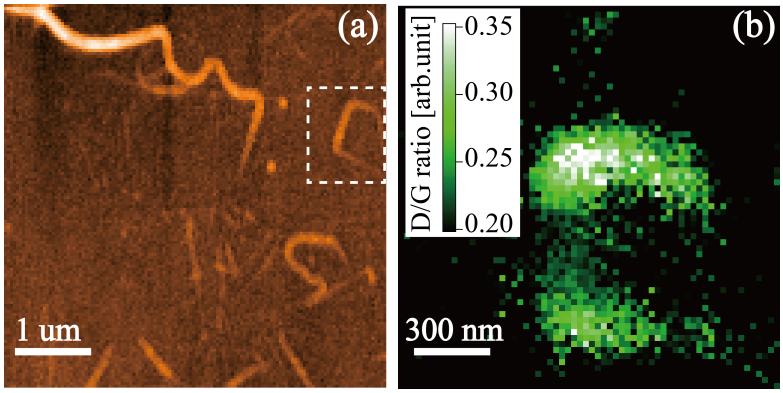

Fig. 7 | (a) AFM image of manipulated SWCNTs to shape “C” character and (b) Raman image with the ratio of D-band intensity divided by G-band intensity in the white dotted region in (a).

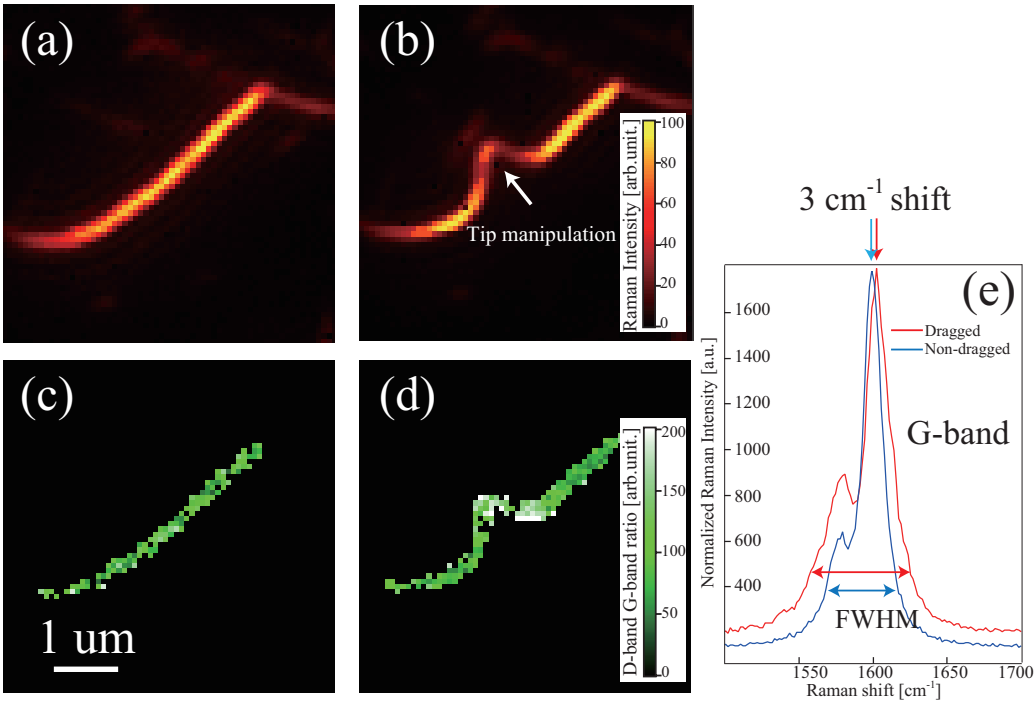

Fig. 8 | Raman image of SWCNTs with the peak intensity in G-band (a) before and (b) after manipulation. D/G ratio image (c) before and (d) after manipulation. (e) A comparison of G-band at dragged area and non-dragged area.

For an evaluation of how defects are induced on SWCNTs through manipulation and what types of strains are related to an inducer of defects, a comparison of D/G-ratio images of SWCNTs between before and after manipulating and Raman shift investigation were conducted, which are shown on Fig.8 (c), (d) and (e). The process of the manipulation are shown as Raman images of SWCNTs before and after manipulation as shown in Fig.8 (a) and (b). White arrow on Fig.8 (a) shows the part where SWCNTs was dragged. From Fig.8 (d), lattice defects were found at manipulated area. Compared the G-band in manipulated area to that in non-manipulated area, full width of half maximum (FWHM) of G-band in manipulated area is tangibly larger than that of G-band in non-manipulated area, as seen from Fig.8 (e). This broadening implies that internal strains were applied to SWCNTs, which means that we disclosed the relation between a deterioration of lattice arrangements and strains. More looking inside, types of strains were verified by frequency shift of peak position of G-band. Higher frequency shift indicates torsional strain on SWCNTs, which occurred at defect area. The fact that defects seemed to be related not only with bend as you could see in Fig.7 but also with torsional strain was revealed.

Let me summarize this section, I noticed that it was quite possible that the manipulation caused defects to SWCNTs. Then next, I found a main cause of defects could be torsional effect rather than tensile strain as well as bending. Note that it is interesting to find that deformations are likely to induce defects in SWCNTs because this is the fist time experiment to succeed to compare the defects before and after being induced on SWCNTs by Raman imaging. Finally, I conclude that the broadening feature of SWCNTs is the evidence of the fact that manipulation always cause internal strains on SWCNTs, and in addition defects were built up on SWCNTs through manipulation. Looking inside more, I also revealed a torsional strain was main cause of defects emerging.

In summary of section 3-2 and 3-3, strains distribution over manipulated SWCNTs was revealed by Raman microscopic measurement, making clear the relation of types of strains with the defects on SWCNTs. These studies indicate a potential ability of AFM dragging precise to control the properties of SWCNTs, which is basic necessity for producing nano-electronic devices. Even though Raman spectroscopic and microscopic techniques are good for making clear the relation, there are no established methods to optically visualize the variation of physical and intrinsic properties at nano-scale resolution, which are enough to evaluate material properties as point-by-point information corresponding to their topographical distribution. So nano-scale resolved optical investigation has been desired for nano-structured material such as SWCNTs. In next section, I show the tip enhanced Raman investigation for getting over the problems.

3-4. 2D color nano-imaging of manipulated SWCNTs

High-resolution characterizations of SWCNTs to understand local variations of deformations and how it affects on their own physical properties have always been challenging. It can be speculated that Raman spectroscopic/microscopic measurements would give direct information related to the intrinsic properties of SWCNTs. However, the diffraction limit of light is always a problem for resolving materials with the size of less than half of the wavelength, which would be about 250~300 nm for visible light. There have been some advances in Raman imaging techniques to overcome the diffraction limit, and researchers have shown impressively high spatial resolutions, which is tip-enhanced technique as I mentioned in chapter 2 [16-23]. In this section, I demonstrate color-coded 2D Raman image of locally strained SWCNTs where the colors represent strain distribution within the SWCNTs at high spatial resolution far beyond the diffraction limit of light. Tip enhanced Raman investigation represented deformation of

molecular alignment of SWCNTs due to the existence of local strain. This investigation revealed extremely localized variations of strains developed on SWCNTs as a convenient form of color images.

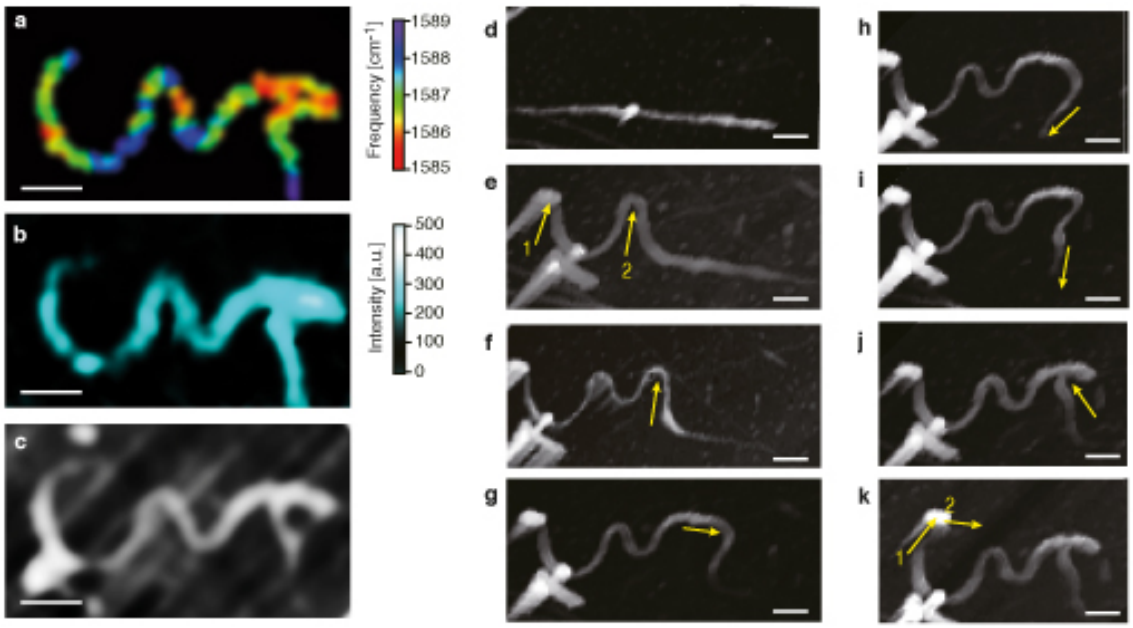

Fig. 9 | Strain distribution along a nanotube at high spatial resolution. a, 2D Colour image of a nanotube manipulated into the shape of the word “CNT”. This image was constructed by colour-coding the frequency position of G+-mode in TERS spectra. The colour variation shows strain distribution along the nanotube at high spatial resolution. b-c, For comparison, TERS image of the same sample constructed from the intensity of G+- mode is shown in b, and simultaneously obtained AFM image is shown in c. d-k, AFM images showing intermediate steps during the fabrication of the “CNT” shaped sample. Yellow arrows indicate the dragging directions in each step.

Firstly, I tried to make a shape of the word “CNT” with SWCNTs by a series of AFM manipulation. With the same manner with manipulation technique mentioned in section 3-1, tip dragged the SWCNTs locally in the direction of tip scanning and SWCNTs was deformed into the “CNT” shape (Fig 9a). A TERS image of the sample is shown in Fig. 9a and a spatial resolution of that image was better than 20 nm far beyond the diffraction limit of light. TERS imaging was performed under contact mode operation of the tip by raster-scanning the sample under a constant tip-applied force of about 0.1nN. This force was small enough to prevent any dragging, scratching or physical damage of the sample. This TERS image was constructed from

the shift of the G+-mode in G-band, which depends sensitively on the local strain and which can distinguish between torsional and tensile strains in SWCNTs by higher frequency shift for a torsional strain and by lower frequency shift for a tensile strain [24-26]. In a simple term, various colors along the length of the SWCNTs in Fig. 9a represent the variation of local strain in the sample. I show a TERS image constructed from the peak intensity of G+ mode in Fig. 9b, and Fig. 9c shows an AFM image simultaneously taken with the TERS image. Both of the images are taken and compared for confirming the physical existence of nanotube manipulated in the shape of the word "CNT". The other AFM images in Figs. 9d-9k were measured with a silicon tip during the process of manipulation, which show a sequence of several intermediate manipulation steps where the arrows indicate the direction of dragging in each step.

For avoiding confusions, let me emphasize that a complicated structure seen near the lower left end in the AFM images was a dust particle attributed to the fact that there were no Raman signal within the signature frequency range of a SWCNT. Therefore, this structure is visible in the AFM images, but not seen in the TERS images.

I explain what the colors in TERS image tells physically with the step-by-step development of strain in the manipulation process as follows. It can be understood that the SWCNTs pushed from an inner location could have a possibility of providing an elongation on SWCNTs if a degree of manipulation is slight, whereas SWCNTs pushed from its end could have more possibility of shifting and rolling rather than getting elongated. Such manners and tendencies can be seen in our sample as the two ends of the SWCNT. The upper part of the letter "C" and the lower part of the letter "T", which is made by tip push from the two end of SWCNT, show blue and green colors in Fig. 9a, indicating the dominance of torsional strain. The dominance of rolling continues further near the free ends of the nanotube to provide green color to the left lower part of "C" and to the mid-lower part of "T". The left part of the letter "N" was created from the second push in Fig. 9e, which being located far from the end of the SWCNT is expected to dominantly stretch the nanotube if the manipulation is slight. Some orange and yellow colors can be seen near the upper left part of "N", however the top area briefly shows blue color, indicating that rolling took over the stretching at that point. It seems that this part of the nanotube has rolled due to the excessive pushes from inner part and resulted in blue-green colors for the lower part of the letter "N". The upper part of the letter "T" was created by the pushes in Figs. 9f, 9g and 9j, all of which correspond to locations away from the ends of the

nanotube, and manners of manipulation is totally different from pushes shown in Fig. 9e, which finally gave red-orange-yellow colors indicating the dominance of stretching on the upper part for “T”. In Figs. 9i, SWCNTs incurred a slight push from side, which is understandable for us to expect an elongation induced on SWCNTs.

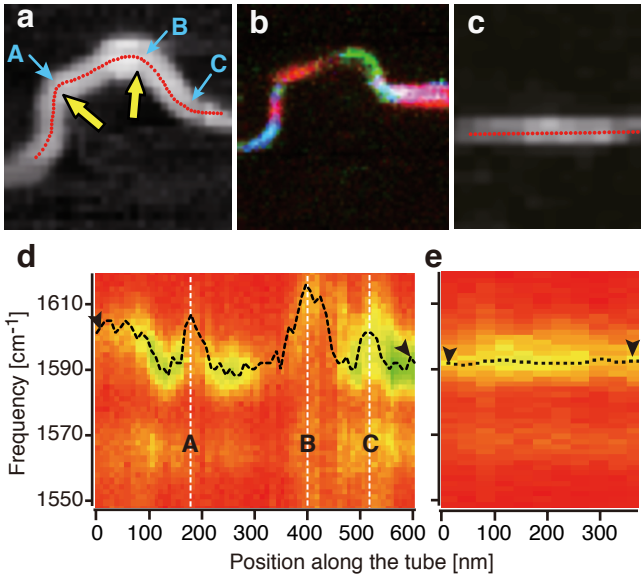

Fig. 10 | Strain induced in CNTs having higher frictional forces. (a) An AFM image of a nanotube, which was dragged along the yellow arrows from two distinct points marked by A and B. (b) A composite TERS image constructed from Raman intensities at three frequencies of 1590 cm^{-1} (red), 1600 cm^{-1} (blue) and 1610 cm^{-1} (green). Frequency-shifted intensity components (blue and green) are dominantly seen at the bent corners. (c) An AFM image of a neighbouring non-manipulated straight part of the sample. (d) The frequency positions of G+ -mode in TERS spectra obtained along the length of the manipulated part of the CNT (corresponding to the red dotted path shown in a) and (e) along the non-manipulated neighbouring area (corresponding to the red dotted path shown in c). Raman frequency variation can be seen only in the manipulated part. The vertical dashed lines correspond to the bent points A, B and C in a where large frequency shifts in the G+ -mode are observed.

It can be understood that a SWCNT would not be much elongated when dragged from its end, and hence the torsional strain should dominate in this case. However, when the nanotube is dragged from an inner location, it could be elongated if this dragging is slight and it could be torsion if the dragging is excessive. The amount of rolling would depend on the frictional forces between the substrate and the SWCNTs, which actually depends on the kind of nanotubes

utilized in the experiment. In the cases where frictional force is large, the effect of rolling would surpass the effect of elongation so that G+-mode may show a higher shift by the manipulation from an inner position. In order to explain this, I demonstrate a simple sample where a nanotube was dragged from just two inner locations, marked by points A and B in Fig. 10a, where the yellow arrows indicate the directions of dragging. AFM image in Fig. 10a shows the area where the CNT was dragged and Fig. 10b shows TERS image constructed with peak-shift of 1591 cm^{-1}, while the AFM image in Fig. 10c shows a neighboring area of the same CNT where it was not dragged. Figures 10d and 10e show shifts in Raman frequency of the G+-mode along the length of the CNT corresponding to Figs. 10a and 10c, respectively. Raman frequency of G+-mode in Fig. 10e remains constant at about 1591 cm^{-1} for the straight part of the CNT, while it varies from 1590 to 1618 cm^{-1} along the length of the CNT in the dragged area in Fig. 10d. This confirms that the strain was developed only in the manipulated part of the nanotube. In contrast to the previous sample, sharp up-shifts that correspond to torsional strain can be seen near those points where the tip apex dragged the SWCNT, even though the dragging points lie at inner locations of the nanotube. In addition, up-shifts can also be seen at the other corner points, such as at point C in the figure, where the SWCNT locally rolled even without a push at that location. This result leads us to the conclusion that the nanotube used in this particular experiment had stronger frictional force on the substrate that provided rotational torque to the SWCNT during manipulation, thus the resultant strain was a combination of tensile and torsional strains, with torsional strain being stronger in magnitude.

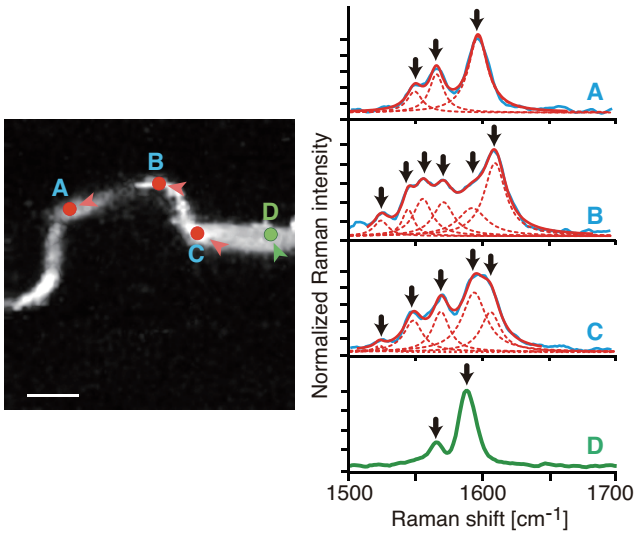

Fig. 11 | Symmetry breakdown induced at the bent corners of the CNT. (a) A TERS intensity image, which is a black-and-white version of Fig. 10b. Three bent corners are marked by the points A, B and C, and the bending curvatures are shown by dotted circles. Point D is marked on the non- manipulated straight part of the CNT. Scale bar, 100 nm (a). (b–e) TERS spectra measured at the points A, B, C and D, indicated in a. The observation of several new modes in the G-band spectral range only at the corners is attributed to the local breakdown in the circumferential symmetry.

Here, let me mention about an interesting fact I found through the experiment shown on Figure. 10. Localized strain in CNT modifies the arrangement of carbon atoms in the nanotube. Particularly, if the CNT is locally bent, the inner and the outer curvatures around the bend are different, causing a modified atomic arrangement. This results in the local breakdown of symmetry around the bend, leading to a relaxation in the selection rules of Raman scattering. A previous study has predicted that the relaxation of selection rules by symmetry breakdown in CNT can lead to the observation of as many as six Raman modes in the G-band spectral rage, which are not observed in a relaxed CNT [29]. Thus, besides the shift in the G^+-mode shown before, I also expect to observe several new modes in the G-band spectral range around the bent area of the nanotube.

I expected to have these change in G-band and tried to investigate the curvature effect. For this purpose, I explored the same TERS image shown in Fig. 10, and investigated the spectral variation along the length of the CNT. The TERS image is reproduced in black-and-white again

in Fig. 11a. The radius of curvature at the corner points A, B and C are approximately estimated to be smaller than 100nm, where we could recognize slight variation in the radii, as shown by the dotted circles around the corners. The spectra obtained from these three points are displayed in Fig. 11b–d, respectively. In addition, a spectrum measured from a point on the non-manipulated straight part of the CNT, marked by D, is shown in Fig. 11e. As expected from the un-manipulated part of the sample, the spectrum in Fig. 11e shows only two peaks corresponding to the usual G− - and G+ -modes. However, because of the breakdown in symmetry near the bent corners, the G-band splits into several peaks at all the three points A, B and C. To understand this splitting numerically, we tried to fit the three spectra A, B and C with six Lorentzian peaks, keeping in mind that not all peaks would have non-zero intensity. The best-fitted Lorentzian components are shown by the red dashed curves and the total intensities are shown by the red solid curves in Fig. 11b–d. As expected, smaller radius of curvature causes greater breakdown in symmetry leading to the appearance of larger number of peaks. Six peaks are observed at point B where the radius of curvature is the smallest, whereas only three peaks are observed at point A where the radius of curvature is the largest amongst the three bent corners. The number of peaks, their relative intensities and their frequency positions significantly change when measured at the intervals of 10nm, confirming that the effect of symmetry breakdown is localized within the vicinity of about 10 nm from the bent corners. Such a highly localized appearance of the symmetry breakdown can only be revealed by my TERS techniques, which cannot be observed in usual far-field Raman measurements.

The TERS image in Fig. 9 show the variation of strain along the CNT with high spatial resolution. I showed the amount of strain developed as well as the frictional force responsible for providing the rolling of the CNTs which is in usual observed by excessive manipulation. And I confirmed small curvature gives symmetry breaking. I thus confirm an important aspect that the strain developed along the manipulated CNT significantly depends on the intrinsic properties of the nanotubes, such as the chirality and the diameter, which could affect the frictional coefficient.

Apart from the results shown here with the manipulation of single nanotubes, I have also successfully performed the movement of an entire nanotube from one location to another and have written various two-dimensional patterns by manipulating more than one nanotubes (a example can be seen in Fig. 9). This manipulation technique is extremely precise and it gives us

freedom to utilize a pre-grown nanotube of our choice, and to manipulate them to a shape and a location of our requirement. I have confirmed that these manipulated nanotubes are mechanically stable after the manipulation. The combination of my manipulation and high-resolution characterization techniques opens paths for the development of well-controlled CNT-based devices with proper characterization of their performances. The methods are well suited for a variety of applications in optical, electronic, mechanical or bio-related usage of SWCNTs.

Summary

I have explained AFM based manipulation technique and how the manipulation affects on the strains and defects generation through this chapter. I described that Raman investigation is a great tool for visualizing the strains and defects induced by the manipulation system. In particular, I affirmed that a shift of G+ mode is sensitive for identifying types of strains applied to SWCNTs, which was caused by tangential or circumferential displacement of carbon atoms on a wall of SWCNTs. Then, experimentally I proved powerfulness of the Raman analytical method for strains and defects distribution by analyzing G+ mode and D-band intensity increment. And also I showed that my AFM-based manipulation works properly for precisely making deformation on SWCNTs. Through the experiment, I claimed that a torsional strain produces defects. However, the diffraction limit of light in visible region prevents us from visualizing the localized strains and localized defects with nano-meter spatial resolutions, which make property identification on SWCNTs intricate. I applied tip-enhanced technique for improving the resolution as well as efficiency of signal enhancement. Through the study, I confirmed nano-meter strains distribution appeared up on SWCNT by TERS. However, I couldn't utilize the RBM and D-band for nano-imaging of SWCNTs but the insufficiency of this technique will evoke more researches about optical methods for nano-material imaging.

References:

[1] Natnael Behabtu *et al.,* Science **339,** 182 (2013).

[2] Ji Wu et al., Nature Nanotechnology **7**, 133–139 (2012).

[3] Marc Ganzhorn et al., Nature Nanotechnology **8**, 165–169 (2013).

[4] Céline Merlet et al., Nature Materials **11**, 3063–310 (2012).

[5] Márcio D. Lima *et al.,* Science **338,** 928 (2012).

[6] Dong-ming Sun et al., Nature Nanotechnology **6**, 156–161 (2011).

[7] Sami Malola, Hannu Häkkinen, Pekka Koskinen, Phys. Rev. B, **78,** 153409 (2008).

[8] Xiaowei Li et.al., Phys. Rev. B, **81,** 195439 (2001).

[9] Xiaojie Duan et.al., Nano Lett, **7,** No. 7, pp2116-2121 (2007).

[10] Bei Wang et.al., Phys. Rev. B, **81,** 115422 (2010).

[11] Xiaowei Li et.al., Phys. Rev. B, **81,** 195439 (2001).

[12] S. B. Cronin et al., Phys. Rev. Lett, **93,** NUMBER 16 (2004).

[13] X. Guoet al., *Sciencedirect Composites: Part B,* **39,** 202–208 (2008).

[14] Amitesh Maiti et al., Chemical Physics Letters, **331,** 21±25 (2000).

[15] H. Kataura, et al., Synth. Met. **103**, 2555 (1999).

[16] N. Hayazawa, Y. Inouye, Z. Sekkat, & S. Kawata, Opt. Commun., **183**, 333–336 (2000).

[17] R. M. Stöckle, Y. D. Suh, V. Deckert,& R. Zenobi, Chem. Phys. Lett., **318**, 131–136 (2000).

[18] A. Hartschuh, E. J. Sánchez, X. S. Xie, & L. Novotny, Phys. Rev. Lett., **90**, 095503–095506 (2003).

[19] P. Verma et. al., Phys. Rev. B., **73**, 045416 (2006).

[20] T. Yano, P. Verma, S. Kawata, & Y. Inouye, Appl. Phys. Lett., **88**, 093125 (2006).

[21] Bailo, E. and Deckert, V. Tip-Enhanced Raman Spectroscopy of Single RNA Strands: Towards a Novel Direct-Sequencing Method. Angew. Chem. Int. Ed., **47**, 1658–1661 (2008).

[22] T. Ichimura, et al., Phys. Rev. Lett., **102**, 186101 (2009).

[23] T. Ichimura et. al., Phys. Rev. Lett., **92**, 220801 (2004).

[24] Duan, X. et al., Nano Lett., **7**, 2116–2121 (2007).

[25] Gao, B. et al.,J. Phys. Chem. C., **112**, 10789–10793 (2008).

[26] X. Li, Y. Jia, J. Dong, & Y. Kawazoe, Phys. Rev. B., **81**, 195439 (2010).

[27] P. Hohenberg and W. Kohn, Phys. Rev., **136**, B864 (1964).

[28] W. Kohn and L. J. Sham, Phys. Rev., **140**, A1133 (1965).

[29] Ren, Y. et al., Phys. Rev. B., **80**, 113412 (2009).

Chapter 4. Localized S-to-M transition in “X”-shaped semiconducting SWCNTs

Theoretical studies have predicted a modulation of electronic bands in SWCNTs due to deformation caused by bridging SWCNTs over electrodes or by crossing one SWCNT over another, which makes “X” shape (from now on, I will refer to it as X-CNTs) [1, 2]. In particular, the electronic transport properties measured at the junctions of X-CNTs showed interesting changes in the conductance of the junctions [2, 3]. X-CNTs can be fabricated intentionally or may happen accidentally, then both SWCNTs can be locally deformed near the junction due to their mechanical interactions via the van der Waals binding of the upper nanotube to the substrate away from the junction. It has been said that such deformation near junction cause metallization on semiconducting SWCNTs. Again Raman spectroscopic and microscopic technique prove usefulness for disclosing what is happening on this junction because of its ability of sensing metallic features in materials by analyzing Fano-shape of G− mode. In this chapter, I demonstrate the semiconductor to metal transition of SWCNTs induced at the junction with nano-meter spatial resolution by tip-enhanced Raman investigation. Before moving forward to experimental section, I explain about the history of researches on X-CNTs and what is Fano-shape of G− mode in section 1 and in section 2 respectively.

4-1. Existing researches on SWCNTs crossing each other in “X”-shape

A study of X-CNT via scanning tunneling microscopy (STM) has predicted that a radial compressional force of about 1 nN can modify their electronic band structure at the junction point [4]. Interestingly, the compression of a semiconducting SWNT was predicted to be the reason of its metallization, which was attributable to the $\pi* - \sigma*$ hybridization effect occurring near the compression point revealed by band gap closing at near K-point calculated with quantum chemical calculation as shown on Fig.1 [5].

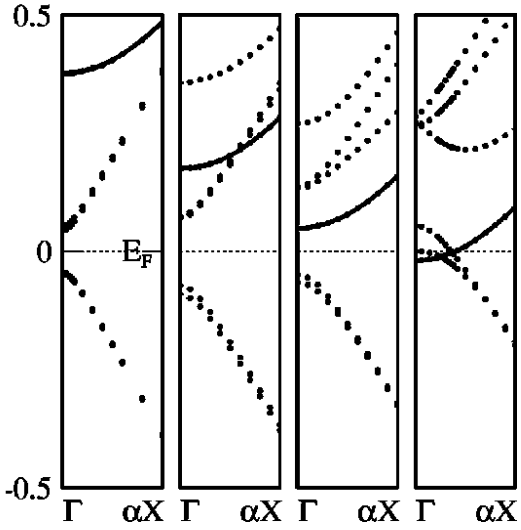

Fig. 1 | Theoretical calculation results of band gap closure at Fermi energy of carbon nanotube under a radial compression [5]. Γ is zero wavenumber in cutting line ($k = 0$) made by zone folding. αX is an edge of wavenumber in cutting line ($k = \frac{\pi}{T}$). Wavenumber for the cutting line is derived by the equation equals to $\mathrm{K} = \mu K_1 + kK_2/|K_2|$, where K_1 and K_2 are reciprocal vector and k ranges from $-\frac{\pi}{T}$ to $\frac{\pi}{T}$.

This phenomenon can also be expected for the X-CNTs because the X-CNTs goes under a slight compression at the crossing point. A dramatic transformation of SWCNTs from semiconductor to metal, invoked by localized pressure, was observed using scanning tunneling spectroscopy (STS) [6]. However, the modification of electronic properties has not been observed at high spatial resolution so far, and hence an ambiguity about the extent of such localized metallization still exists, which keeps this topic a subject of discussion, and there remains considerable debate to stimulate extensive research enthusiasm on this subject.

4-2. Fano effect on metallic SWCNTs

One of the prominent first-order vibrational mode in a typical Raman spectrum of SWNT is the so called G-band, which comprises two distinct Raman modes, G− mode and G+ mode, arising from the tangential vibrations of carbon atoms along the periphery and along the length, respectively. In metallic nanotubes, it is believed that the G− and G+ modes represent the LO and TO phonons, respectively [7, 8]. In general, it is common that the conduction electrons in SWCNT couple strongly to the Γ-point LO phonon because each produces a longitudinal field that interacts with the charge density of the other. Since the conduction electrons represent a

continuum plasmon and the LO phonons are bound, the interaction is of Fano-type, which incorporates an asymmetric broadening accompanied with a line-shift [9–11]. For understanding this asymmetric broadening, I derive mathematically the equation of intensity of G− mode in the case that there are free electrons in the system. The coupling represented as Breit-Wigner-*Fano* (BWF) line in G− mode is the phenomenon of an interaction of discrete excited phonon state which is denoted as |p) with continuum state of excited electron which is denoted as |e) in according to quantum theory. The electron-phonon coupling is assumed to be present in the form of a matrix element V between |e) and |p). Then a mutual repulsion of the levels E_e against E_p produce positions of $E_{\pm}$ due to V elements. If a Raman-active transition is allowed to both a discrete level of energy and a continuum with a density of levels ρ(ω) which is coupled with an interaction of strength V, the resulting interference gives rise to a Raman scattering intensity proportional to

$$I_{BW} = \frac{\pi\rho(\omega)[T_c(\omega-\omega_0)-VT_d]^2}{[\omega-\omega_0-V^2R(\omega)]^2+[\pi V^2\rho(\omega)]^2} \tag{4.1}$$

Here T_c and T_d are, respectively, Raman transition amplitude for the continuum and discrete transitions, and

$$R(\omega) = P\int d\omega' \frac{\rho(\omega')}{\omega-\omega'} \tag{4.2}$$

where P denotes the principal part of the integral. We can recast Eq. (4.1) into the form more commonly found in the literature, namely,

$$I(\omega) = \frac{T_c{}^2\pi\rho(\omega)(q+e)^2}{(1+\epsilon^2)} \tag{4.3}$$

by setting

$$\Omega = \omega_0 + V^2R \qquad \Gamma = \pi V^2\rho \qquad \varepsilon = (\omega-\Omega)/\Gamma \quad q = (V^2R + VT_d/T_c)$$

Then BWF function used in this study can be simply described as [10]

$$I(\omega) = I_0\frac{[1+(\omega-\omega_{BWF})/q\Gamma]^2}{1+[(\omega-\omega_{BWF})/\Gamma]^2} \tag{4.4}$$

where I_0, ω_{BWF}, Γ, and 1/q are intensity, renormalized frequency, broadening parameter and the asymmetric parameter, respectively. 1/q reveals the strength of electron-phonon coupling [6] because 1/q includes the ratio of interaction of continuum state with discrete states equals to VT_d/T_c. So if you assumed that free electrons filled in electronic band of materials, a shape of spectra becomes asymmetric shape, which is came from particular discreet phonon states interacting with continuum electrons state. Therefore, the G− mode contains information related to the electronic properties of the nanotube in the form of asymmetry of the mode.

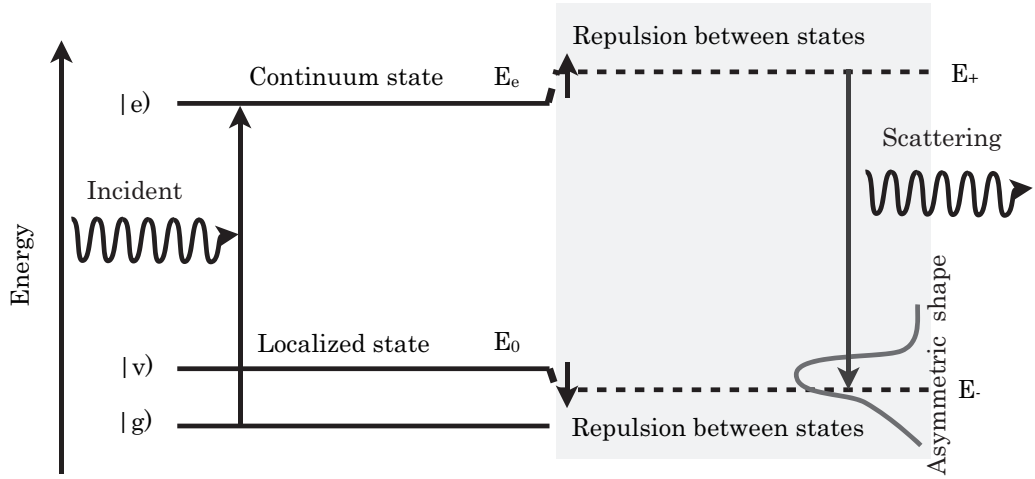

Fig. 2 | Scheme of asymmetric Raman shape induced by a repulsion between states with the state with free electrons. Incident light comes into a certain system filled with free electrons denoted as a grey square. Coupling of electrons with LO phonon of SWCNTs provide an asymmetric shape on a shape of G− mode.

However, as for the origin of Fano lineshape and the broadening, there have been unsound arguments. LO mode has been expected to have a bearing on electronic damping on phonons, which cause a frequency softening, which is derived from the coupling of single-particle electron-hole pair with phonon via Kohn anomaly (KA) [22-25] or the coupling of collective excitation of electron (plasmon) with a phonon [26]. KA is one of strong candidates as the relevant phenomena to the BWF lineshape of G− mode. LO phonon distorts reciprocal lattice space in such a way that a dynamic bandgap is induced in the electronic band structure, which is called KA [27]. The dynamic bandgap lowers the energy of the valence electrons near the Fermi point, and thus it lowers the electronic energy required to keep the lattice constant or binding, leading to phonon softening, which recursively lower the frequency of LO phonon.

Note that the detailed mechanism of the Fano line shapes in LO mode has remained a long-standing debatable topic, so let me spare the detailed discussions on it now.

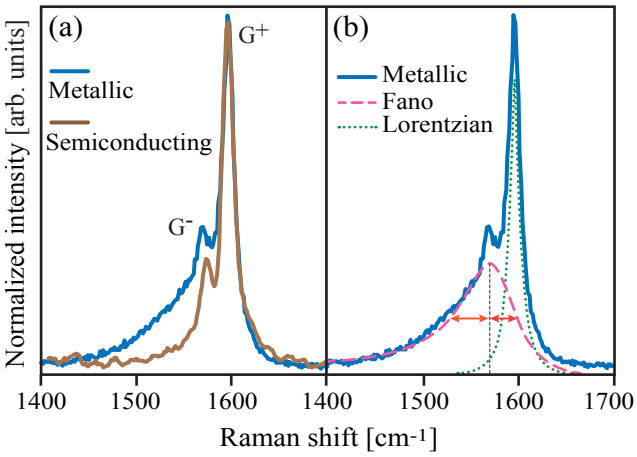

Fig. 3 | (a) Example of typical Raman spectra of metallic and semiconducting SWNTs presented in blue and brown colors, respectively, in the G-band spectral range showing both G− and G+ modes. (b) Raman spectrum of metallic SWNTs could be best fitted with an asymmetric Fano peak and a symmetric Lorentzian peak, shown by pink dashed line and green dotted line, respectively. As one can notice in Fano peak, an asymmetry around the peak position can be clearly observed.

The spectra are normalized at the intensity of the G+ mode. As one can notice here, the G− mode at about 1560 cm^{-1} is significantly asymmetric for metallic SWCNT in comparison to that for the semiconducting SWNT, whereas the G+ mode remains the same for the two kinds of nanotubes [see Fig. 3(a)]. The Raman spectrum of the metallic nanotubes in the G band spectral region can be best fitted with an asymmetric Fano peak and a symmetric Lorentzian peak, as shown in Fig. 3(b). The red dashed curve in Fig. 3(b) shows the Fano component, where a clear asymmetry around the peak position can be observed. The Raman spectrum from semiconducting nanotubes, however, can be best fitted with two symmetric Lorentzian peaks (not show here). Thus, by observing the asymmetry in the line shape of the G− mode in Raman spectrum, one can understand the electronic nature of the nanotube.

In general, BWF mode has a frequency dependence, 1/q dependence and Γ dependence on the diameter of nanotube and an intensity dependence on the degree of bundle [16, 20-21]. Note

that, for fitting BWF mode near 1550 cm^{-1} and decomposing the mode from other modes in G-band, Fano function described in (4. 4) is often used, which is useful for following discussion in next section.

4-3. TERS investigation of extremely localized semiconductor-to-metal transition in SWCNTs

Here, I show the investigation of the vibrational features of semiconducting X-CNTs utilizing TERS spectroscopy and microscopy across the junction at a high spatial resolution. The well-known G− mode Raman vibration of SWCNTs contains a signature of the electronic property of the nanotubes in the form of the line-shape of the vibrational mode as I mentioned at previous section, which is denoted as G− mode. By investigating whether G− mode has the symmetry shape or not at a spatial resolution far beyond the diffraction limit, I have observed the phenomenon of metallization of semiconducting SWCNTs as well as its extreme localization near the junction point in a X-CNT sample.

Sample preparation for this study was as follow: The semiconducting SWCNTs used in present study were procured from Meijo carbon Inc. These nanotubes with the diameter of 1.4 nm and a purity of > 99% were first ultrasonically dispersed with 1-2 dichrolethane, and then a droplet of this solution was spin-casted onto the glass coverslip. The chirality of these nanotubes were estimated from the radial breathing modes in Raman measurements using the Kataura plot [12] and were found to be (12, 11), (15, 7) and (16, 5). I then searched for nanotubes laying on each other in the shape of the letter “X” using atomic force microscopy (AFM) imaging. As estimated from the height in the line profile of AFM images, I could find such X-CNTs in bundles with approximately 1 to more than 3 nanotubes.

The frequency dependence of Raman intensity in a Fano-type interaction is usually given as again from Eq. (4.4) [11]

$$I(\omega) = I_0 \frac{[1+(\omega-\omega_{BWF})/q\Gamma]^2}{1+[(\omega-\omega_{BWF})/\Gamma]^2} \tag{4.4}$$

where I_0, ω_{BWF} and Γ represent the intensity, renormalized frequency and broadening parameter, respectively. The parameter q represents coupling between the phonon and the plasmons, and provides asymmetry to the line-shape of the G− mode in Raman spectrum of

metallic SWNTs. For large value of q, Eq. (4.4) takes the form of Lorentzian equation, and $q = \infty$ or $1/q = 0$ refers to a purely symmetric phonon shape corresponding to the G− mode of semiconducting SWNTs. Therefore, absolute value the term $1/q$, *i.e.,* $|1/q|$, obtained from Fano curve fitting of the G− mode in a SWNT can be used as a measure of the degree of metallization of the nanotube.

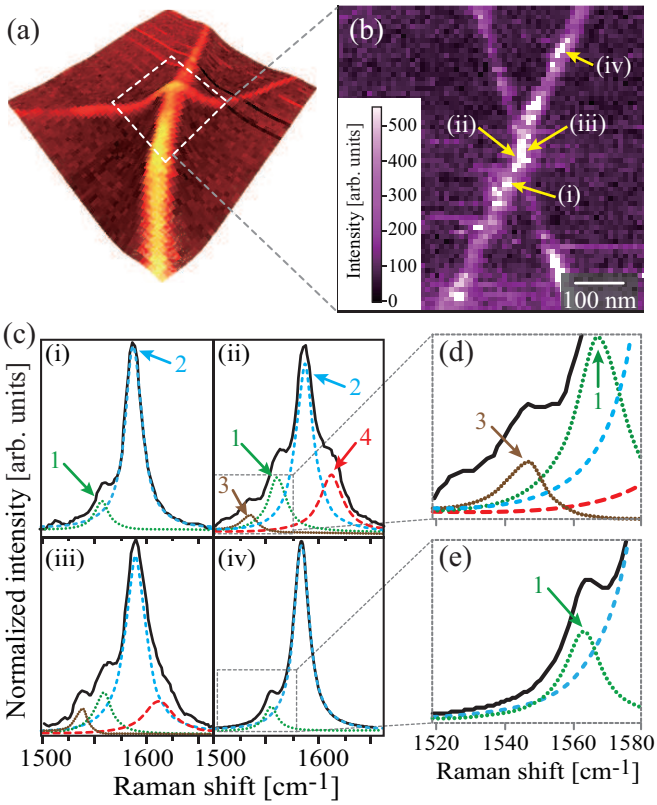

Fig. 4 | (a) A 3D AFM image of our X-CNT sample. TERS spectra were measured from the area enclosed by the white dashed lines. (b) TERS image of the enclosed area of the sample, constructed from the peak intensity of the G+ mode. (c) TERS spectra obtained from points (i) through (iv) indicated in (b). The spectra obtained far from the junction could be decomposed into two symmetric Lorentzian peaks (peak 1 and peak 2), while the spectra obtained near the junction required two additional peaks, one asymmetric Fano peak (peak3) and one symmetric Lorentzian peak (peak 4) for the best fitting. (d) and (e) show magnified Raman spectra obtained near the junction and far from the junction, respectively, in the spectral range of 1520 to 1580 cm^{-1}.

Fig. 4(a) shows a 3D AFM image of our X-CNT sample consisting 1-3 SWNTs (height within 1 nm - 2.8 nm), as estimated from the height in the image. A TERS image of the same sample but from a smaller area enclosed in the white rectangle, constructed from the peak intensity of the G+ mode, is shown in Fig. 4(b). TERS spectra obtained from 4 different points along one branch of X-CNT, as indicated by the points (i) through (iv), are shown in Fig. 4(c). A careful observation of these spectra reveals that the spectra obtained far from the junction, at points (i) and (iv), could be best fitted with two Lorentzian curves centered at 1565 and 1588 cm^{-1}, representing the G− and G+ modes of SWCNTs, respectively. I will call these peaks as peak 1 and peak 2, as also indicated in the figure. On the other hand, the spectra obtained around the junction at points (ii) and (iii), required two extra curves for best fitting, one Fano curve centered at 1548 cm^{-1} and one Lorentzian curve centered at 1607 cm^{-1}, which I will call as peak 3 and peak 4, respectively. Thus, around the junction, I needed four curves to best fit the raw data. For clarity, Figs. 4(d) and 4(e) show the presence and absence of the Fano curve (peak 3) for the spectra obtained at points (ii) and (iv), respectively, in zoomed illustration.

It is clear from Fig. 4(c) that the G-band spectral shape is significantly changed around the junction of the nanotubes in X-CNT sample. Noticeably, there are two interesting differences in the spectra obtained near the junction as compared to those obtained far from the junction. The first difference is the presence of two extra modes, and the second is the appearance of the asymmetric Fano curve. Indeed, both these differences arise from the fact that two branches of the X-CNT sample are locally deformed at the junction point. Provided that the reports by T. Hertel is true [1], this extremely localized deformation results from their interactions via the van der Waals binding of the upper nanotube to the substrate away from the junction. Then the nanotubes lose their radial symmetry locally at the junction point due to the deformation, and thus the selection rules are relaxed and Raman scattering is degenerated with additional phonons becoming observable. In addition to the reduction of symmetry, the deformation also causes the electronic bands to modify locally, resulting in a modification in the electronic properties of the SWCNT near the junction point, where it turns metallic from semiconducting. This local semiconductor-to-metal transition gives rise to the Fano-type broadening in the G− mode arising right from the junction point. It can also be concluded by examining the spectral shape that the extent of deformation is much smaller than the size of the confined light at the tip apex, and hence when a TERS spectrum is measured right at the junction point, it always contains contributions from both deformed and non-deformed areas of the nanotube.

To wrap up the point of the above discussion, the appearance of four peaks at the junction can be explained as follows – First, peak 1 and peak 2 originate from the unperturbed part of the nanotube immersed within the confined light. Then, peak 3 originates from the Fano interaction arising from the local deformation of nanotubes at the junction. The Fano interaction, as defined in Eq. (4.4), causes an asymmetrical broadening as well as a shift towards lower frequency to the G− mode, which causes peak 3 to show up distinctly at a shifted frequency compared to peak 1. Finally, peak 4 arises from the degeneration of Raman modes caused by the reduction in radial symmetry at the junction point, which is not observed in the total radial symmetry. The existence and the location of this peak is in good agreement with a previous report, where the authors concluded that as many as six Raman modes can be observed in G-band spectral range due to symmetry breaking [14]. In the present case, the nanotubes are only slightly distorted, and hence I observe only one additional peak. I also expect, but could not confirm, that peak 2 might have some contribution from the deformed area of the nanotube as well. In this way, I can observe one Fano and three Lorentzian peaks at the junction point.

In order to understand the localization of this modified electronic property of the nanotubes near the junction point, TERS spectra obtained from the entire X-CNT are decomposed sample into Fano and Lorentzian curves for their best fittings. As expected, at all points far from the junction, the Fano parameter, $1/q$, in the fitting was zero, which means the Fano curves were essentially nothing but symmetric Lorentzian curves. On the other hand, the value of $1/q$ varied from -0.2 to -0.4 for spectra obtained from points near the junction, indicating that nanotubes had significant amount of phonon-plasmon coupling around the junction [15-16].

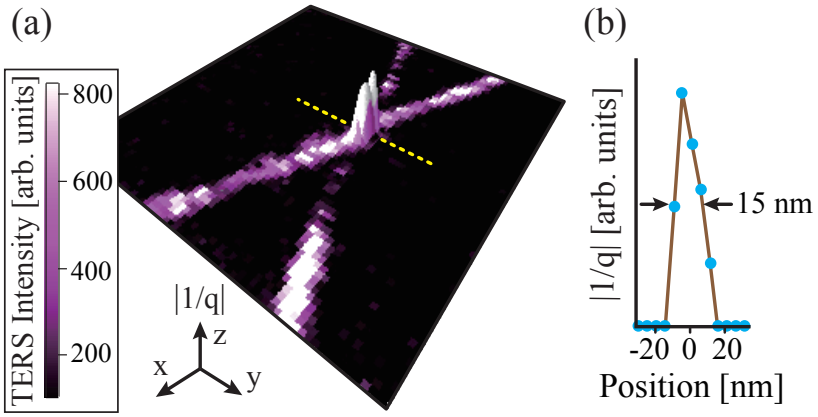

Fig. 5 | (a) A 4D TERS image of our X-CNT sample, where x- and y-axes show the sample plane, the color represents TERS intensity of the G+ mode in accordance with the color bar shown on left, and the z-axis shows the value of $|1/q|$, which provides a measure for the metallization of the nanotubes. Clear increase of $|1/q|$ and its localization near the junction confirms that the semiconductor-to-metal transition is strongly confined to the junction point. (b) A line profile of $|1/q|$ along the yellow arrow in (a) is shown.

Fig. 5(a) shows a 4D TERS image of the X-CNT sample (with 3 dimensions in space and one in color), where the x-y plane shows the sample plane, the color indicates the TERS intensity of G+ mode and the z-axis in the vertical direction shows the absolute value of the Fano parameter, $|1/q|$. As it can be clearly seen, a sharp peak in z-direction can be seen around the junction point, indicating strong localization of $|1/q|$ in the x-y plane. I measured a line profile along the yellow dashed line in Fig. 5(a), which is shown in Fig. 5(b). The full width of half maxima for the line profile of $|1/q|$ was estimated to be 15 nm. I expect the local deformation is confined to even smaller length than 15 nm, which is also evident from the observation of Raman signals from both metallic and semiconducting nanotubes in Fig. 4(c) near the junction point. It has also been theoretically predicted for flattened SWNTs that such metallization could be localized to a much smaller length [17, 18].

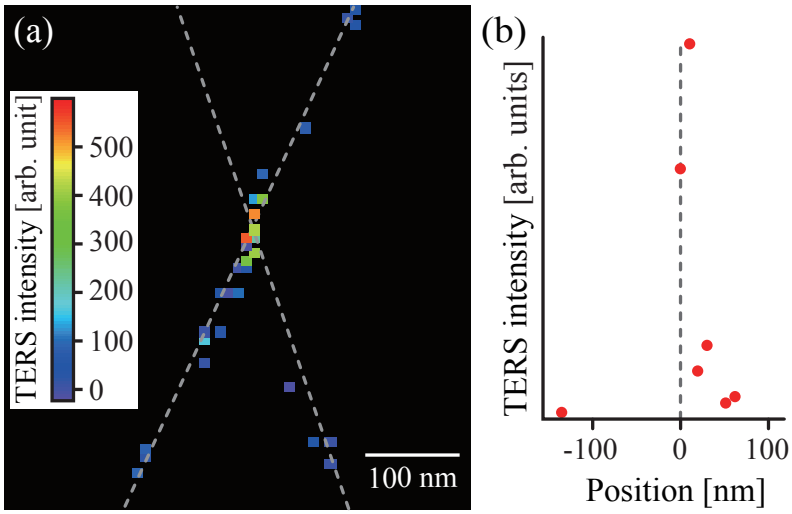

Fig. 6 | (a) White dashed lines are drawn from Fig. 4 and they depict the location of nanotubes in X-CNT sample, whereas the colored spots indicate TERS intensity of peak 4, in accordance with the color bar on the left. The intensity of peak 4 is strong only in the close vicinity of the junction. (b) TERS intensity plotted along one branch of the nanotube across the junction showing sudden increase in intensity at the junction.

In order to find the origin of the semiconductor-metal transition, I further investigated the other new mode, peak 4 shown in Fig. 4(c) (ii), which was also observed only in the close vicinity of the junction point. As explained before, this mode becomes observable in Raman scattering due to the reduction of symmetry, and thus expected to be found only around the junction point. Figure. 6 shows the spatial confinement of this mode. The white dashed lines in Fig. 6(a) are drawn from the TERS image in Fig. 4(a) and they depict the location of the X-CNT sample. The dots with different colors represent the observation of peak 4, where the color is a measure of the peak intensity, in accordance with the color bar on the left. As one can see here, the intensity of peak 4 is strong only in the very close vicinity of the junction point. This is also displayed in Fig. 6(b), where the peak intensity is plotted with respect to distance measured from the junction point. The dashed line in Fig. 6(b) refers to the junction point. Some existence of peak 4 can be still seen at locations far from the junction point, albeit with very low intensity. I do not expect peak 4 to appear far from the junction, however the peak fitting process brings them with some non-zero intensity. Nevertheless, they can be ignored as their intensities are

close to the background intensity. Fig. 6 clearly shows strong localization of the distortion and the relaxation of symmetry near the junction point.

From the results obtained in Figs. 5 and 6, I can conclude that the pressure applied by the nanotubes on each other at the junction point in X-CNT sample deforms the nanotubes in extremely localized area near the junction, which results in local semiconductor-to-metal transition and also in symmetry breaking. However, I want to press points that the localized pressure couldn't make a deformation on SWCNTs much, which was concluded by the RBM signal. A shift of RBM was not much enough to indicate radial deformation of SWCNTs by the comparison of RBM in crossed point and edge point of crossed SWCNTs as shown on Fig.7.

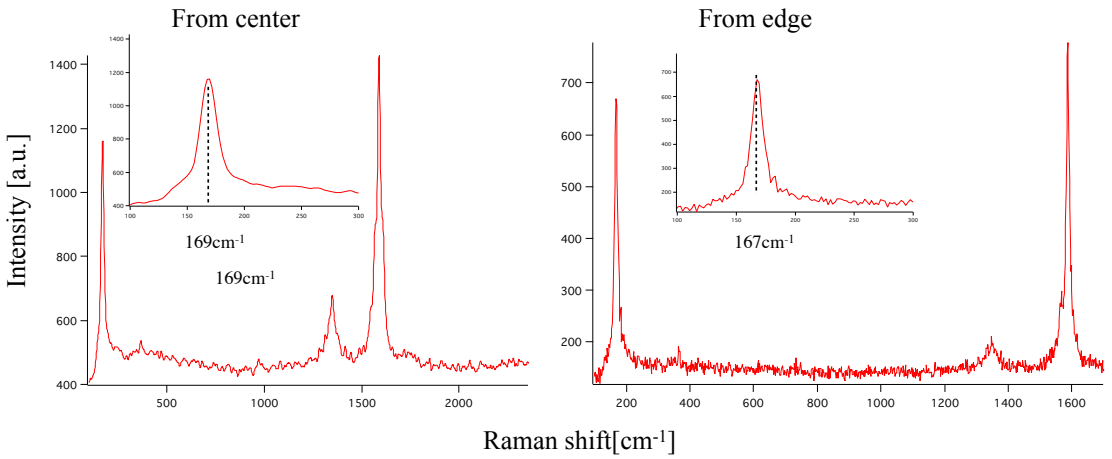

Fig. 7 | Raman spectra of X-CNTs used in this study. The difference of Raman shift of RBM between junction part and other part is just 2 cm^{-1} which is not enough to indicate strong deform on SWCNTs at crossed part.

By using the equation of $\omega_{RBM} = A/d_t$, where $A = 248cm^{-1} \cdot nm$, I found that the diameter of each nanotube included in the bundle changed from 1.485 nm to 1.460 nm at junction point. This difference means 1.5% distortion, which is estimated from Fig. 7, implies that the band gap closure reported by Bin Shan *et. al.* is completely overestimated [18]. My results revealed slight radial compression cause metallization experimentally.

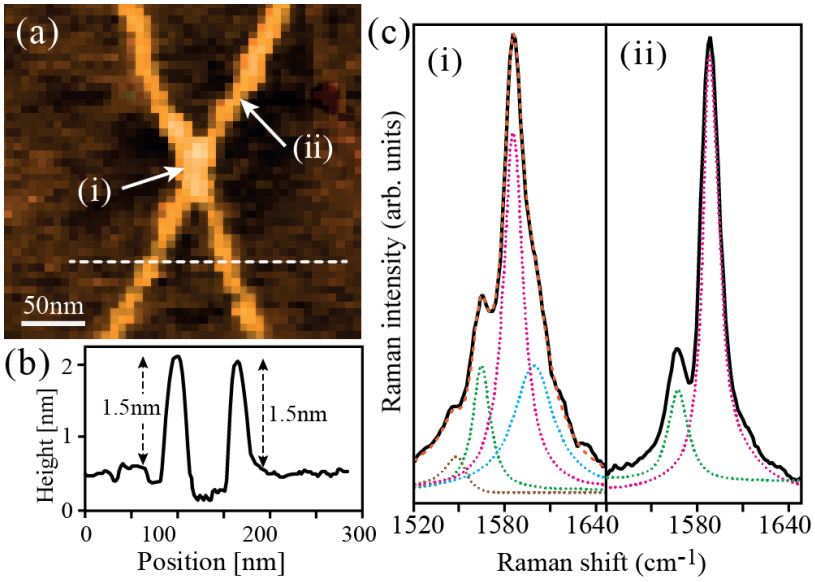

Fig. 8 | (a) AFM image of an X-CNT sample consisting single nanotubes in each branch. (b) A line profile along the white dashed line confirming the diameter of the nanotubes is about 1.5 nm. (c) TERS spectrum in the G-band region measured from point (i) at the junction and point (ii) far from the junction. Similar to Fig. 4, the spectrum far from the junction can be fitted with two Lorentzian curves, while the spectrum at the junction requires one additional Lorentzian and one Fano curves for the best fitting.

I would like to mention again that even though our X-CNT sample in Fig. 4 consisted 1-3 aggregated nanotubes in each branch, the phenomenon of localized semiconductor-to-metal transition at the junction point was identical as expected for a sample with single nanotubes in each branch. In order to establish our point, I demonstrate similar measurements in Fig. 8, which were performed on an X-CNT sample consisting single nanotubes. Fig. 8(a) shows an AFM image of the sample, and Fig. 8(b) shows a line profile along the white dashed line in Fig. 8(a). The line profile confirms that both branches in this sample contain single nanotubes with diameter of 1.5 nm, which is a similar value that we estimated from the RBM, 1.4 nm. TERS spectra measured in the G-band spectral region are shown in Fig. 8(c), where spectra measured at the junction point and far from the junction point are shown by (i) and (ii), respectively. The curve fitting shows that the spectrum measured near the junction at point (i) can be best fitted (orange dashed line) to the measured spectrum (black solid line) with one Fano-curve (brown dotted line) and three Lorentzian curves. At the same time, the spectrum measured far from the

junction at poimt (ii) can be best fitted with two Lorentzian curves. This result confirms that even though the sample in Fig. 4 contained 1-3 nanotubes in each branch, this small aggregation did not affect our analysis about localization of deformation and electronic properties of the SWCNTs.

I was also interested in understanding as to what would be the situation of local deformation and semiconductor- to-metal transition of the bundle consisting of large numbers of nanotubes. In order to investigate that, I studied another sample with similar shape, but with more than 10 nanotubes in each branch. I would call this sample as X-CNT2, on which I performed same investigations as on the previous sample. TERS spectra in the G-band spectral range from the X-CNT2 sample, obtained at a point far from the junction and at a point on the junction is shown in Figs. 9(a) and 9(b), respectively. Very similar to the case of previous sample in Fig. 9(c), we could best fit the TERS spectrum with two Lorentzian curves at a point far from the junction (peak 1 and peak2), while we needed four curves to obtain a best fit to the TERS spectrum obtained at the junction point. I call the two additional peaks observed at junction point as peak 3 and peak 4, similar to the previous case. However, the interesting difference in X-CNT2 compared to the previous X-CNT is that peak 3, which was expected to have Fano shape, was always found symmetric with $|1/q| = 0$. This essentially means that I have revealed the phenomenon of semiconductor-to-metal transition that occurs at extremely localized area of the sample near the junction point of the X-CNT sample made of few semiconducting SWCNTs through the appearance of Fano-interaction between plasmon and phonon in Raman scattering but in the X-CNT2 case I couldn't. I listed detailed line-shape analysis of TERS spectra of crossed nanotube taken at junction part and at far from junction part, which is referred as straight point, each in Table. 1. All parameters including $|1/q|$ value and FWHM of vibrational modes and the frequency for X-CNT (Sample I) and for X-CNT2 (Sample II) are listed in Table. 1.

Table. 1 show that FWHM of the G− mode observed in this experiment was narrower than that of general BWF modes (40-60 cm^{-1}). However, the broadening is a sufficient, but not necessary signature of a metallic feature of SWCNTs [22, 28]. Therefore, one-to-one correspondence between line broadening (2Γ ranges from 10 cm^{-1} to 100 cm^{-1}) and $|1/q|$ factor is invalid.

	Fitting curve (component)	In junction part			In straight part	
		ω(cm^{-1})	FWHM (cm^{-1})	1/*q*	FWHM (cm^{-1})	1/*q*
Sample I	BWF (G_{BWF}^{-})	1548	10-24	-0.1 -0.4	10-15	0
	Lorentzian (G_{E1}^{-})	1565	14		14	
	Lorentzian (G_{E1}^{+})	1589	16		16	
	Lorentzian (G_{E2}^{+})	1607	30		30	
Sample II	BWF (G_{BWF}^{-})	1548	30	0	10-17	0
	Lorentzian (G_{E1}^{-})	1565	14		14	
	Lorentzian (G_{E1}^{+})	1588	16		16	
	Lorentzian (G_{E2}^{+})	1603	30		30	

TABLE. 1 | Detailed line-shape analysis of TERS spectra of X-CNT (Sample I) and X-CNT2 (Sample II) taken at junction part and straight part each. The frequency (ω) and FWHM (2Γ) are listed for Lorentzian and BWF features. 1/q value shows asymmetric feature for BWF line. The fitting parameters were obtained by the means of smallest root square error of fitting procedure.

At the same time, I have also discovered that Raman spectrum are degenerated in the same area near the junction, confirming extremely localized physical distortion of the nanotubes due to the pressure applied on one nanotube by the other. The modification of electronic properties as well as the physical distortion takes place within a length smaller than 15 nm, however, I could not distinctly confirm the exact size beyond the spatial resolution of our TERS system, which was 15 nm.

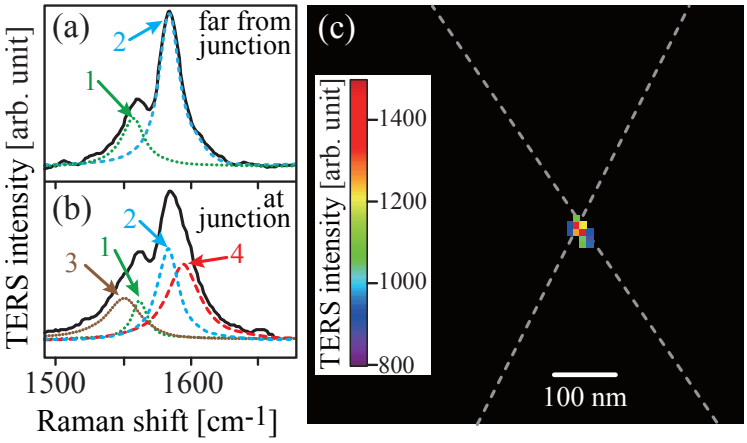

Fig. 9 | TERS spectra obtained from a point (a) far from the junction, and (b) at the junction, of the sample X-CNT2 containing more than 10 SWNTs in each branch. The spectrum in (a) could be best fitted with two Lorentzian peaks (peak 1 and peak 2), while the spectrum in (b) could be best fitted with four Lorentzian peaks. In contrast to Fig. 4, peak 3 was found to be a symmetric Lorentzian peak, rather than an asymmetric Fano peak. (c) White dashed lines depict the location of nanotubes in X-CNT2 sample, and the colored spots indicate TERS intensity of peak 4, in accordance with the color bar on the left. The intensity of peak 4 is strong only in the close vicinity of the junction, depicting strong confinement of this peak around the junction.

Fig. 9(c) shows an image obtained from the intensity of peak 4 in TERS spectra from X-CNT2 sample. As can be seen from the color, the peak intensity was found to drastically increase near the junction. The spatial resolution in this case was again the same as the size of the tip apex, confirming a strong localization of distortion-induced effects. The results confirm that for sample containing bundles of many nanotubes, the physical distortion leading to a reduction of symmetry still exists at the junction point, however, there are negligible interactions between the phonon and the electron via KA. The absence of Fano interaction indicates that either there are no free electrons in bundled nanotubes even after compression, or the LO phonons are no more bound due to the bundled effect, which make a strong plasmon enhancing [19]. The actual reason is not clear, but my results show that there are no Fano interactions in bundled SWNTs, even though physical deformation, as seen via degenerated phonon modes, is present. However, I must say that this is very interesting, because no other technique can reveal this information simultaneously at such a high spatial resolution.

The present results could be very interesting for CNT-based device fabrication where the local modification of electronic properties could play a very important role I believe.

Summary

In summary, I briefly introduced the trends in researches on X-CNTs for pointing out the significance on an investigation of X-CNTs. Through the introduction of existing researches, I emphasize that the metallization of semiconducting SWCNTs has attracted many researchers because of its leading to exploiting new application using SWCNTs. I explained that BWF mode in G− mode help us to see the metallization. And the Fano feature derived from electron–phonon interaction appearing on SWCNTs. By utilizing our state-of-the-art TERS spectroscopy, localized S to M transition was visualized at the junction of X-CNTs and I found that strains applied to SWCNTs were main inducers for this transition. The transition was a localized phenomenon on SWCNTs, which implies the capability of its nano-switching features from semiconductor to metal nature. This research provided noticeable facts that SWCNT's electronic features have no limitation with just strains. However I couldn't disclose the types of strains affecting on the metallization, which needs more spatial resolution and enhancement mechanism for improving analytical precision of this technique.

References:

[1] T. Hertel *et al.*, Phys. Rev. B., **58**, 13870 (1998).

[2] Henk W. Ch. Postma *et al.*, Phys. Rev. B., **62**, 653 (2000).

[3] M. S. Fuhrer *et al.,* Science **288**, 494 (2000).

[4] J. W. Janssen *et al.,* Phys. Rev. B., **65**, 115423 (2002).

[5] Chan-Jeong Park *et al.*, Phys. Rev. B., **60**, 10656(1999)

[6] L. Vitali *et al.,* Phys. Rev. Lett., **96**, 086804 (2006).

[7] M. Lazzeri *et al.,* Phys. Rev. B., **73**, 155426 (2006).

[8] S. Piscanec *et al.,* Phys. Rev. B., **75**, 035427 (2007).

[9] U. Fano, Phys. Rev., **124**, 1866 (1961).

[10] V. Klein *et al.,* in Light Scattering in Solids I, edited by M. Car-dona (Springer-Verlag, Berlin, 1983), pp. 169-172.

[11] A. M. Rao *et al.,* Nature **388**, 257 (1997).

[12] H. Kataura, *et al.,* Synth. Met., **103**, 2555 (1999).

[13] A. Jorio *et al.,* New Journal of Physics **5**, 139.1 (2003).

[14] Y. Ren *et al.,* Phys. Rev. B., **80**, 113412 (2009).

[15] K. T. Nguyen, A. Gaur, and M. Shim, Phys. Rev. Lett., **98**, 145504 (2007).

[16] S. D. M. Brown, A. Jorio, P. Corio, M. Dresselhaus, G. Dresselhaus, R. Saito, and K. Kneipp, Phys. Rev. B., **63**, 155414 (2001).

[17] M. S. C. Mazzoni *et al.,* Appl. Phys. Lett., **76**, 1561 (2000).

[18] Bin Shan et. al., Appl. Phys. Lett., **87,** 173109 (2005)

[19] Chaoyang Jiang, Phys. Rev. B., **66**, 161404 (2002)

[20] C. Jiang, K. Kempa, J. Zhao, U. Schlecht, T. Basche, M. Burghard, A. Mews, Phys. Rev. B., vol. **66**, no. 16, pp.161404-161407, 2002.

[21] N. Bendiab, R. Almairac, M. Paillet, J. L. Sauvajol, Chemical Physics Letters, vol. **372**, pp. 210-215, 2003.

[22] Y. Wu et al., Phys. Rev. Lett. **99,** 027402 (2007).

[23] M. Lazzeri, S. Piscanec, Francesco Mauri, A. C. Ferrari, and J. Robertson, Phys. Rev. B., **73,** 155426 (2006).

[24] H. Farhat et al., Phys. Rev. Lett., **99**, 145506, (2007)

[25] O. Dubay, G. Kresse, and H. Kuzmany, Phys. Rev. Lett., **88**, 235506, (2002)

[26] S. M. Bose, S. Gayen, and S. N. Behera, Phys. Rev. B., **72,** 153402 (2005).

[27] G. G. Samsonidze, Phys. Rev. B., **75,** 155420 (2007).

[28] A. Jorio *et al.,* Phys. Rev. B., **66,** 115411 (2002).

Conclusion

In this dissertation, the response of SWCNTs on deformations has been discussed on the basis of tip-enhanced Raman spectroscopic and microscopic investigations. The capability of TERS microscopy as a nano-imaging method was experimentally verified.

In first chapter, the principle of Raman scattering in SWCNTs was introduced on the basis of group theory and quantum theory of Raman scattering process. I made a point that understanding of group theory and symmetry property of materials is needed for comprehension of the selection rules. And a basic physics on the property of SWCNTs was mentioned.

In second chapter, the principle of tip-enhanced techniques for improving spatial resolution and efficiency of signal generation was explained. For improving a TERS performance, I explained precise tip positioning, z-polarized excitation and optimum geometry of tip apex.

In third chapter, Raman scattering investigations on deformed SWCNTs was conducted with far field and with near field Raman microscopy. I visualized the strains and defects induced by the home-made manipulation system with the use of conventional confocal Raman microscopy and TERS. Through this chapter, I explained about relationship between types of strains and defects by analyzing G+ mode and D-band intensity increment. “CNT” character of bundle SWCNTs was imaged as 2D-color imaging with TERS. This study proved that this manipulation technique was extremely precise and it gave us freedom to utilize a pre-grown nanotube of our choice, and to manipulate them to a shape and a location of our requirement. I claimed that the combination of my manipulation and high-resolution characterization techniques opens paths for the development of well-controlled CNT-based devices with proper characterization of their performances.

In forth chapter, the fact that local pressure was a main cause of metal transition from semiconducting feature of SWCNTs was verified through tip-enhanced Raman investigations on crossed SWCNTs. For the experiment, I have utilized TERS to measure X-CNT sample with a spatial resolution of 15 nm. I found that the modification of electronic properties as well as the physical distortion took place within a length even smaller than 15 nm by analyzing LO mode of carbon nanotube and the shape of LO mode had asymmetric shape. The results are very interesting, because no other technique can reveal this information simultaneously at such a high spatial resolution. The present results could be very attractive for CNT-based device

fabrication where the local modification of electronic properties could play a very important role. This work would be interesting not only for those who are working in the fields related to CNT-based devices, where the local modification of electronic properties could play an important role, but also for those who are interested in electron-phonon interaction at extremely high resolution, and even those who are simply interested in mapping some physical, electronic or chemical properties of a sample at nano-scale.

The whole experimental results imply that TERS technique proved their excellent capability of enabling us to explore nano-world.

List of publications

Original papers

[1] Yoshito Okuno, Yuika Saito, Satoshi Kawata, and Prabhat Verma "Tip-enhanced Raman investigation of extremely localized semiconductor-to-metal transition of carbon nanotube" Physical Review Letters, Vol. 111, p. 216101 (2013)

[2] Yoshito Okuno, Yuika Saito, Shota Kuwahara, Taka-aki Yano, Satoshi Kawata, and Prabhat Verma "Raman microscopic investigation of the strains effect to defects of dragged SWCNTs" Applied Physics Letters (in preparation)

[3] Taka-aki Yano, Taro Ichimura, Shota Kuwahara, Fekhra H'Dhili, Kazumasa Uetsuki, Yoshito Okuno, Prabhat Verma, and Satoshi Kawata, "Tip-enhanced nano-Raman analytical imaging of locally-induced strain distribution in carbon nanotubes" Nature Communications, Vol. 4, 2592 (2013)

International conferences

[1] Yoshito Okuno, Yuika Saito, Satoshi Kawata and Prabhat Verma "Evaluation of localized semiconductor to metal transition of semiconducting carbon nanotube by Tip-enhanced Raman investigation", JSAP-OSA Joint Symposia 2013, 16p−D5−7, (Doshisha University, Kyoto, Japan, September 16 th - 20th, 2013)

[2] Yoshito Okuno, Yuika Saito, Satoshi Kawata, and Prabhat Verma "Tip-enhanced Raman investigation of extremely localized metallization phenomenon in semiconducting carbon nanotube", 7th International Conference on Advanced Vibrational Spectroscopy (ICAVS7), P-266, (Kobe Convention Center, Hyogo, Japan, August 25th- 30th, 2013)

[3] Yoshito Okuno, Yuika Saito, Satoshi Kawata, and Prabhat Verma "Tip-enhanced Raman Scattering Study of Metalized-Semiconducting Carbon Nanotube", The 10th Pacific Conference on Lasers and Electro-Optics Rim (CLEO) , ThI2-3, (国立京都国際会館, Kyoto, Japan, June 30th - July 4th, 2013)

[4] Yoshito Okuno, Prabhat Verma, and Satoshi Kawata "Raman scattering study of the crossed carbon nanotubes using tip enhanced Raman scattering (TERS) microscopy", Fifth International Symposium on Atomically Controlled Fabrication Technology, P-77, (Osaka

University Nakanoshima Center, Osaka, Japan, October 23th, 2012)

[5] Yoshito Okuno, Shota Kuwahara, Kazumasa Uetsuki, Takaaki Yano, Prabhat Verma, and Satoshi Kawata "Tip enhanced Raman imaging and analysis of crossed nanotube junction", Taiwan-Japan Nanophotonics and Plasmonic Metamaterials Workshop (National Taiwan University, Taiwan, January 11th- 13th, 2012)

[6] Yoshito Okuno, Shota Kuwahara, Kazumasa Uetsuki, Takaaki Yano, Prabhat Verma, and Satoshi Kawata "Tip enhanced Raman imaging and analysis of crossed nanotube junction", Sixth photonics center symposium_Nanophoto Asia (Shima, Japan, September 20th-21th, 2011)

[7] Yoshito Okuno, Shota Kuwahara, Kazumasa Uetsuki, Takaaki Yano, Prabhat Verma, and Satoshi Kawata "Tip enhanced Raman imaging and analysis of crossed nanotube junction", The 8th Asia-Pacific Workshop on Nanophotonics and Near-Field Optics (Adelaide, Australia, August 25th- 26th, 2011)

Domestic conferences

[1] 奥野義人 、桑原彰太、矢野隆章、プラブハット・バルマ、河田聡 「Raman Scattering Study of Deformed Single-Walled Carbon Nanotubes」『第 39 回フラーレン･ナノチューブ総合シンポジウム』、2P-44、（京都大学、京都、2010 年 9 月）

[2] 奥野義人 、桑原彰太、矢野隆章、プラブハット・バルマ、河田聡 「単層カーボンナノチューブの構造変化時における分光特性変化の観察」『2010 年秋季第回応用物理学会学術講演会』、14p-NK-10、（長崎大学、長崎、2010 年 9 月）

Award

[1] The Best Poster Presentation Award**,** Yoshito Okuno, Shota Kuwahara, Kazumasa Uetsuki, Takaaki Yano, Prabhat Verma, Satoshi Kawata "Tip enhanced Raman imaging and analysis of crossed nanotube junction", Taiwan-Japan Nanophotonics and Plasmonic Metamaterials Workshop, (January, 2012)

Acknowledgement

I would like to express my gratitude to Prof. Satoshi Kawata, who has been my adviser at the Laboratory of Scientific Instrumentation Engineering (LaSIE). Talks with you gave me an opportunity to face myself.

In preparing this thesis, I have been helped by questions, suggestions, criticisms, and advices from Prof. Prabhat Verma, Associated Prof. Yuika Saito.

In terms of managing the LaSIE from a big-picture perspective, I've learned a lot from Associated Prof. Katsumasa Fujita. His capability of managing everything about LaSIE had a beneficial impact for my way of accomplishing business tasks.

In terms of managing and keeping the environment in LaSIE from field site, attitudes of Associated Prof. Satoru Shoji. provided me good influence.

In terms of understanding what is significant for an evaluation of carbon nanotubes, I got clear knowledge from Prof. Yoshihiro Kobayashi. I thank you for your courtesy extended to me.

In terms of concentrating on what physical phenomena occurred through my experiment, I've learned a lot from Prof. Yasuhiro Sugawara. With your suggestion, I could have the sincere attitude to face on physical phenomena.

In terms of understanding what is Fano mode and what is caused by reciprocal space changes, I've leaned a lot from Prof. Hiroshi Harima. With your advices, I could brush up the contents of my thesis.

I would like to thank Dr. Yasuaki Kumamoto, Dr. Kyoko Masui, Dr. Masahito Yamanaka, Dr. Almar F. Palonpon, Dr. Liang-da Chiu, Dr Susan E. Skelton and Dr. Jun Ando for giving advice with respect to experiment and researches.

For my research life and private life, Mitsuhiro Honda, Dr. Masaya Okada always gave me strong vitality to carry on everything. I will not forget everything I had with you such as overnight work and sleeping on chairs like as you used to do and hanging out with you for playing outside. I bet I couldn't make my research through without your help, discussion and nice chatting.

I would like to thank Dr.Yu Jun, Zhao Yan, Toshihiro Mino, Maouli Imad, Yoshihiro Ohashi and Takayuki Umakoshi, and other NSOM group members for exchanging knowledge in Nano-Photonics.

I would like to express thankful to Yasuo Yonemaru, Shota Ushiba, Kentaro Mochiduki, Kozue Watanabe and Kazuki Bando for discussion about fundamental physics and optics. This helped me to consider all events happening in the world more deeply, which navigate me to proceed my research forward.

I appreciate other members in LaSIE and my friends all over the world. I could lead the effective research life thanks to my amazing memory with you.

I finally show my deep gratitude to my mother and my brother for giving an emotional support throughout my life. Without it, I couldn't have done anything to make my life worth living.

Appendix

Probability amplitude described by the momentum operator of electron in molecule

Here, I will translate the probability amplitude of Eq. (1.5) in chapter 1 to the one with the use of the momentum of electron in molecule denoted as P by considering state changes with one-photon generation and annihilation.

Let's think about the Raman scattering process that a molecular state of $|m\rangle$ transit to the one of $|n\rangle$, while one photon annihilates in $k'l'$mode and one photon generates in $k''l''$. Initial state of $|q\rangle$ and final state $|s\rangle$ is described as a product of a ket vector of molecular state by a ket vector of radiant field, which is described as like $|m\rangle|\nu\rangle$. Because two-photon-process only affect on two-modes in vibrational states, eigenstate of radiant field can be describe only by the number of photons in two-modes expressed like as $|\nu_{k'l'}, |\nu_{k''l''}\rangle$.

On the condition that the number of photons in $k''l''$ mode and in $k'l'$ mode at initial state changes from 0 to 1 and from $\nu_{k'l'}$ to $\nu_{k'l'} - 1$ respectively,

$$|q\rangle = |m\rangle|\nu_{k'l'}, 0\rangle \tag{1.6}$$

$$|s\rangle = |n\rangle|\nu_{k'l'} - 1, 1\rangle \tag{1.7}$$

are derived, then which has relation with

$$h\nu_q = h\nu_m + \nu_{k'l'}h\nu_{k'} \tag{1.8}$$

$$h\nu_s = h\nu_n + (\nu_{k'l'} - 1)h\nu_{k'} + h\nu_{k''} \tag{1.9}$$

Given that an intermediate state $|r\rangle$ can connect initial state $|q\rangle$ to final state $|s\rangle$ by energy perturbation H_Q, a radiant field of an intermediate state should be equivalent to one-photon annihilation or one-photon generation, which is expressed respectively as following equations,

$$|r_1\rangle = |e\rangle|\nu_{k'l'} - 1, 0\rangle \tag{1.10}$$

$$|r_2\rangle = |e\rangle|\nu_{k'l'}, 1\rangle \tag{1.11}$$

where $|e\rangle$ is a molecular part of an intermediate state. As you can see from Eq. (1.10) and Eq. (1.11), there are two types of intermediate states. Then these energy states becomes like following,

$$h\nu_{r_1} = h\nu_e + (\nu_{k'l'} - 1)h\nu_{k'} \tag{1.12}$$

$$h\nu_{r_2} = h\nu_e + \nu_{k'l'}h\nu_{k'} + h\nu_{k''} \tag{1.13}$$

By using Eq. (1.6-13) and Eq. (1.4) shown in chapter 1, which is the Hamiltonian of quantized interaction between electrons and radiant field, and performing partial integration to radiant field, one can have following equation.

$$b_s^{(2)}(t, r_1) = \frac{\langle s|H_Q|r_1\rangle\langle r_1|H_Q|q\rangle}{h(\nu_{r_1} - \nu_q)} = \frac{e^2h}{16\pi^4m^2}\frac{\langle n|P_{l''}|e\rangle\langle e|P_{l'}|m\rangle}{h(\nu_e - \nu_m - \nu_{l'})} \times (\nu_{k'l'})^{\frac{1}{2}}(\nu_{k'}\nu_{k''}\sigma_{k'}\sigma_{k''})^{\frac{-1}{2}} \tag{1.14}$$

This equation indicates the process that one-photon in the mode $k'l'$ is absorbed and the one in the mode $k''l''$ is emitted by the Hamiltonian of quantized interaction denoted as H_Q. And,

$$b_s^{(2)}(t, r_2) = \frac{\langle s|H_Q|r_2\rangle\langle r_2|H_Q|q\rangle}{h(\nu_{r_2} - \nu_q)} = \frac{e^2h}{16\pi^4m^2}\frac{\langle n|P_{l'}|e\rangle\langle e|P_{l''}|m\rangle}{h(\nu_e - \nu_m + \nu_{l''})} \times (\nu_{k'l'})^{\frac{1}{2}}(\nu_{k'}\nu_{k''}\sigma_{k'}\sigma_{k''})^{\frac{-1}{2}} \tag{1.15}$$

This equation indicates the process that one-photon in the mode $k''l''$ is absorbed and the one in the mode $k'l'$ is emitted by the Hamiltonian of quantized interaction denoted as H_Q.

Through an above sequence of equations, translating the probability amplitude of Eq. (1.5) in chapter 1 to the one with the use of the momentum of electron in molecule denoted as P is performed.